

Functional Analysis of MTSS1 Regulation of Purkinje Cell Dendritic Development and Actin Dynamics

Kelly Kawabata

ABSTRACT

Dendrite patterning is a critical determinant of neuronal function and connectivity, yet shows high diversity among neuronal types. Thus, the question of how neurons acquire their appropriate morphology is a major interest in the study of neuronal development. Purkinje cells develop large, space-filling dendrites in a single plane with little overlap among the individual dendrites. To achieve this, Purkinje cell dendrites show a characteristic developmental pattern in which contact between dendrites, mediated by numerous small protrusions, signals one or both dendrites to retract. The actin-rich protrusions found on these dendrites function as environmental sensors, and while their dynamic changes in morphology have often been studied in the context of spinogenesis and synaptic plasticity, little work has been done on the contribution of these protrusions to the final morphology of dendritic arbors.

Metastasis-suppressor 1 (MTSS1) is a membrane and actin-scaffolding protein that shows notably high, developmentally-regulated expression in Purkinje cells. Using MTSS1 conditional knockout (cKO) mice, stereotypical reduction in dendritic arbor size and shape was observed, concomitant with significant increase in dendritic protrusion length. These morphological phenotypes were similarly observed in Purkinje cells cultured *in vitro*. Live imaging demonstrated that cKO Purkinje cells underwent frequent branch retraction at the earlier stages of their development, with no reduction in ability to form dendrites, suggesting that the over retraction of dendrites was the main contributor to the MTSS1 knockout dendritic phenotype. This increase in retraction was facilitated by increased contact between the longer dendritic protrusions. To understand what changes in the actin cytoskeleton led to this increase in dendritic protrusion length, several pharmacological inhibitors were added to Purkinje cells with either loss or overexpression of MTSS1. While MTSS1 overexpression upregulated the activity of the branched-actin nucleator ARP2/3, loss of MTSS1 resulted in

increased formin-dependent actin regulation. Thus, this loss of negative formin regulation in cKO Purkinje cells led to the increased length of dendritic protrusions.

The formin DAAM1 was observed to be highly localized to dendritic protrusions, and could transiently induce longer filopodia in Purkinje cells with induced expression of a constitutively active DAAM1 construct. Through biochemical experiments, the central region of MTSS1 was observed to bind to DAAM1, and expression of this portion was sufficient to rescue the MTSS1 knockout morphological phenotypes observed in Purkinje cells. These results suggested that neither the well-characterized I-BAR nor WH2 domain was necessary for MTSS1 function in Purkinje cells. Using Single-Molecule Speckle Imaging (SiMS), visualization of individual constitutively active DAAM1 dimers demonstrated that in the presence of MTSS1, the DAAM1-dependent elongation of actin was inhibited in two modes. The first was due to a non-specific inhibition of actin elongation due to WH2-dependent sequestration of monomeric actin. The second was a specific induction of DAAM1 pausing during actin elongation, likely due to the specific binding between the central region of MTSS1 and DAAM1. Together, these results suggest that MTSS1 may function as a regulator of DAAM1 that had already been activated, modulating its actin polymerization activity at the tips of dendritic protrusions. This regulation further links between biological events in distinct hierarchies and spatiotemporal scales; actin dynamics occurring at the molecular, submicron and second scale, and neuronal morphogenesis occurring at the scale of hundreds of microns and several days.

1 CONTENTS

Abstract.....	2
List of Abbreviations.....	6
Chapter 1. Introduction.....	7
1.1 Purkinje Cell Dendrites and Their Development.....	8
1.1.1 Dendrite form and function.....	8
1.1.2 Dendrite development.....	14
1.1.3 Dendritic protrusions (spines, filopodia).....	19
1.2 MTSS1	22
1.2.1 MTSS1 structure and domains.....	22
1.2.2 MTSS1 Molecular function.....	25
1.2.3 MTSS1 in neurons	30
1.3 Neuronal Actin.....	33
1.3.1 Introduction to actin.....	33
1.3.2 Actin in dendritic protrusions	38
Chapter 2. Results	42
2.1 Characterization of MTSS1 loss in Purkinje Cells.....	43
1.1.1 In vivo loss.....	43
1.1.2 In vitro loss and live imaging	50
1.1.3 MTSS1 truncate rescue experiments.....	55
1.2 Identification of MTSS1 downstream pathways.....	59
1.2.1 Upregulation of ARP2/3.....	59
1.2.2 Downregulation of formin	62
1.2.3 Characterization of DAAM1 in Purkinje cells	64
1.3 Regulation of DAAM1 by MTSS1	68
1.3.1 MTSS1 DAAM1 interaction.....	68
1.3.2 Negative regulation of DAAM1 by MTSS1 in mammalian NIH3T3 cells	70
1.3.3 Negative regulation of DAAM1 using SiMS imaging.....	72
1.3.4 Biochemical analysis of MTSS1 inhibition of DAAM1.	77
Chapter 3. Discussion	80
3.1 Discussion.....	81
3.2 Limitations of this study	89
Chapter 4. Materials and Methods	90
4.1 Animals.....	91
4.2 Primary Cell Culture	91

4.3 Cell Line Cultures	92
4.4 Plasmids and Construction	92
4.5 AAV production	94
4.6 AAV intracerebellar injection.....	94
4.7 Genotyping	94
4.8 Purkinje cell electroporation.....	95
4.9 Pharmacological Experiments	95
4.10 Immunocytochemistry/ Immunohistochemistry.....	95
4.11 Induced expression of constitutively active C-DAAM1	96
4.12 Immunoprecipitation and Western Blot Analysis	96
4.13 Protein Purification	97
4.14 GST Pull-down.....	98
4.15 Image Acquisition	98
4.16 XTC cell electroporation and preparation for SiMS imaging.....	99
4.17 TIRF imaging of C-DAAM1-dependent elongation of F-actin.....	100
4.18 Image Analysis.....	101
Acknowledgements	103
References	104
Image Licensing Information	114

LIST OF ABBREVIATIONS

Abbreviation	Definition
AAV	Adeno-Associated Virus
ABP	Actin-Binding Protein
ARP2/3	Actin-Related Proteins 2/3
cKO	conditional Knockout
DAAM1	Dishevelled Associated Activator of Morphogenesis 1
DAD	Diaphanous Autoregulatory Domain
DID	Diaphanous Inhibitory Domain
DIV	Days In Vitro
I-BAR	Inverse Bin/Amphiphysin/Rvs
ICR	Institute of Cancer Research –mouse strain
G-actin	Globular-actin
GFP	Green Fluorescent Protein
GST	Glutathione S-Transferase
GluR δ 2	Glutamate-Receptor-like molecule δ 2
F-actin	Filamentous-actin
FH1	Formin Homology domain 1
FH2	Formin Homology domain 2
Flox	Flanked by LoxP
MIM	Missing-in-Metastasis
MTSS1	Metastasis Suppressor protein1
PXX	Postnatal day XX
PI(4,5)P ₂	Phosphatidylinositol 4,5-bisphosphate
PRD	Proline-Rich Domain
SD	Standard Deviation
SEM	Standard Error of Mean
SMI-FH2	Small Molecule Inhibitor of Formin Homology Domain 2
SRD	Serine-Rich Domain
WH2	Wiskott-Aldrich homology 2
WT	Wildtype

CHAPTER 1. INTRODUCTION

1.1 PURKINJE CELL DENDRITES AND THEIR DEVELOPMENT

1.1.1 Dendrite form and function

Neurons are post-mitotic, electrically excitable cells that vary widely in their size, localization, type of input received, mode of information integration, and manner of signal output. The neuronal network requires precise connections to form circuits that are able to correctly transmit and process information, and it has been well-established that improper neuronal connectivity during development leads to neurological diseases and disorders (Kaufmann and Moser, 2000). To achieve proper connectivity, neurons must extend unique processes to both receive (dendrites) and send (axons) information through crowded and oftentimes very distant target neurons (**Figure 1A**). However, while much has been focused on axonal growth and guidance for establishment of proper synaptic connectivity, there have been relatively fewer studies regarding the rules governing dendrite growth and population of their receptive fields.

Dendrites function as the site of postsynaptic input, and while the number of possible morphologies a neuron can possess is impressively high, neurons must minimize their branching to reduce resource cost and achieve the most efficient wiring (Cherniak, 1994). Thus, dendrites develop to reflect the neuron's function, resulting in a huge variety in shape, density, localization relative to the soma, and extent of reach, (**Figure 1B**). These parameters impact the placement and number of synapses a neuron can make, as well as modify the electrical characteristics of the dendritic compartment (Häusser et al., 2000; London and Häusser, 2005; Mel et al., 2017).

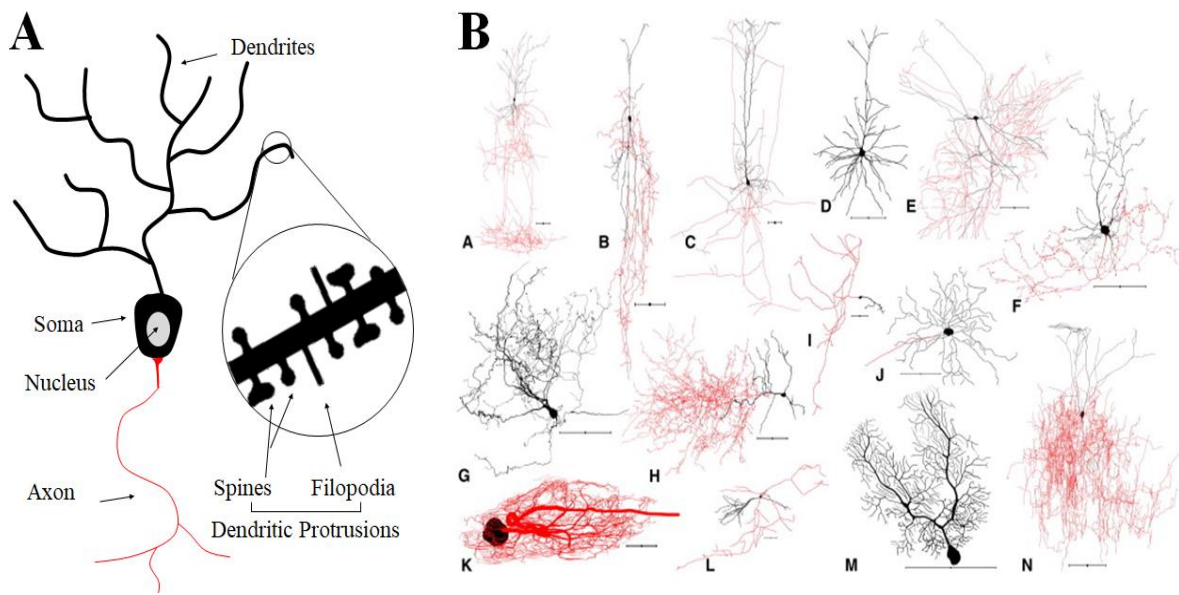


Figure 1. Neuronal structure and their diversity.

(A) Neurons are cells with typical organelles, in addition to unique processes. In general, dendrites are formed closer to the soma, and are the receivers of information. Some neurons have dendrites covered with dendritic protrusions, which include filopodia-like structures and spines. Oftentimes, synapses may be found on these protrusions. The axon conveys information away from the soma to other neurons or target tissues that can be some distance away. **(B)** An example of the variety of morphologies dendritic (black) and axonal (red) arbors can make. Image reproduced from Parekh and Ascoli (2013) with permission.

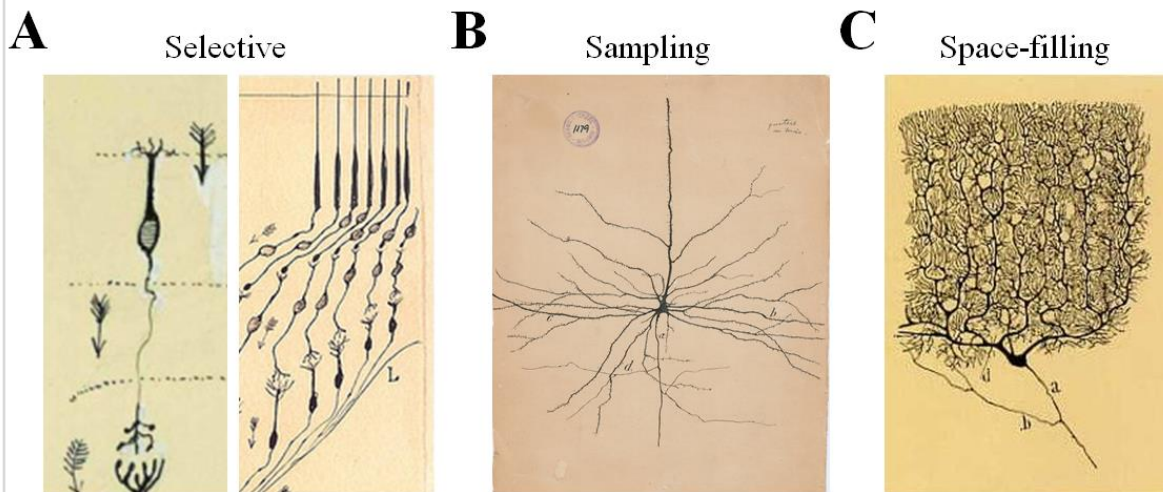


Figure 2. Dendrite arbor morphology reflects specific neuronal subtype function.

(A) Olfactory sensory neuron (left) and bipolar neurons of the retina (right). Selective dendrites connect to a single target, and are often found in sensory systems. **(B)** Pyramidal neuron of the cortex shows sampling dendrite morphology. **(C)** Purkinje cell of the cerebellum fills its receptive field with non-overlapping dendrites. All drawings from Santiago Ramón y Cajal (1852-1934); Public domain – Creative Commons.

An approximate classification based on type of information processing divides dendrites into selective, sampling, and space-filling patterns (Fiala and Harris, 2007) (**Figure 2**). Selective dendritic arbors connect a single input to the neuron, effectively functioning as a band pass filter of incoming signal (**Figure 2A**). Space-filling dendrites function as their name suggests and extend a dense dendritic arbor intended to maximize coverage of an input field and integrate information into a single output (Snider et al., 2010) (**Figure 2C**). Sampling dendritic arbors fall between these two extremes and will take a representative sample of input from their receptive field, for more nuanced calculations (**Figure 2B**). Thus, it is of high interest to clarify the molecular mechanisms underlying how different neuronal subtypes can form such a variety of dendritic arbors.

Neurons with space-filling dendrites are widely used as a model to clarify molecular mechanisms underlying dendrite formation, due to the ease of observation and detection of defects in dendritic morphology. Neurons with space-filling dendrites show conservation of many of its characteristics throughout several neuronal subtypes; these include neurons with two-dimensional dendritic arbors consisting of a single plane (Purkinje, drosophila da neurons) or a few, stratified planes (retinal ganglion cell, amacrine).

In my work, I utilized mouse cerebellar Purkinje cells (**Figures 3A-B**) for modeling and studying dendritic development. The cerebellum plays an important role in motor control and learning (Ito, 1989) and is a popular model to use due to its orderly and well-characterized circuit organization. Purkinje cells form a single parasagittal plane of dense, non-overlapping dendrites (Ramon y Cajal, 1911) that densely covers its receptive field. The flat morphology allows innervation from thousands of afferent

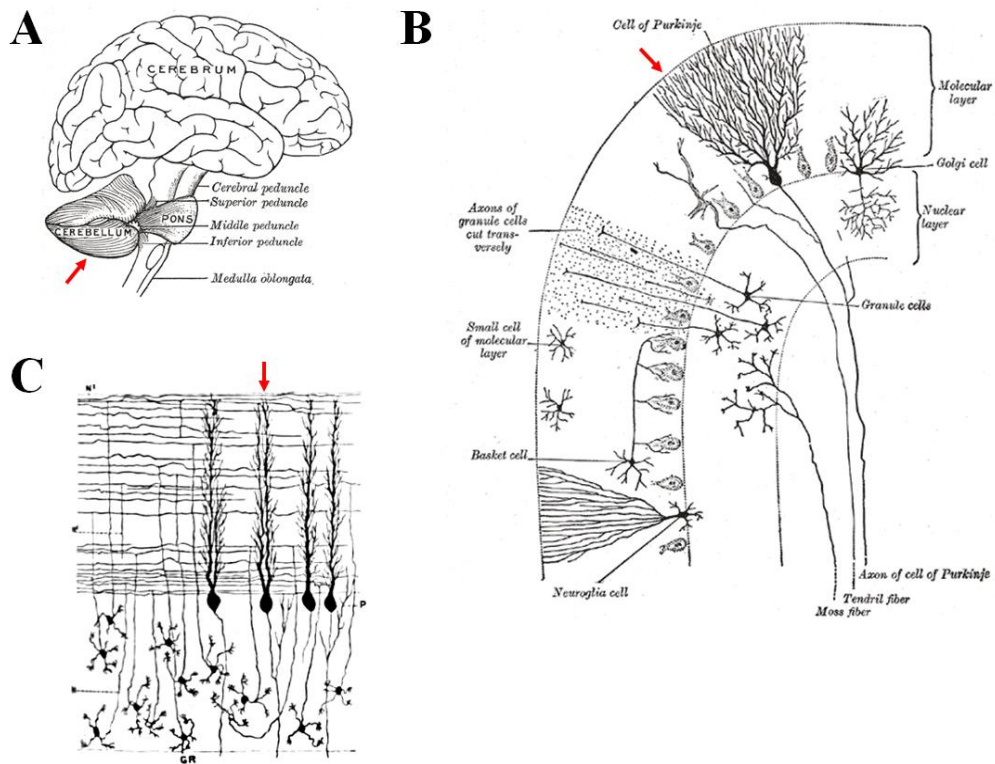


Figure 3. Cerebellar layout and Purkinje cells.

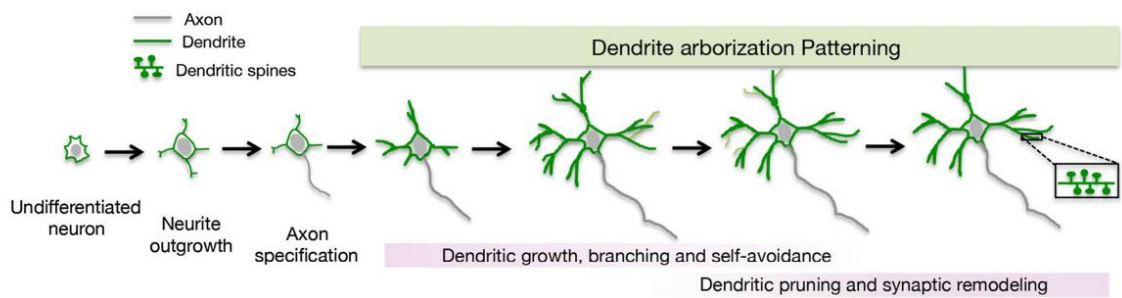
(A) The cerebellum (red arrow) is located at the rear of the brain and is involved in motor learning and coordination. Henry Gray (1918). **(B)** Cerebellar cortical layer organization from a sagittal slice view shows Purkinje cells (red arrow) aligned in a single layer with dendrites extending toward the meninges. Henry Gray (1918). **(C)** A coronal slice view shows Purkinje cells (red arrow) forming a flat shape, allowing innervation from multiple granule cell axons and minimization of multiple synapse per afferent connection. Daniel John Cunningham (1913). All images: Public domain – Creative Commons.

parallel fibers, which are the axons of the cerebellar granule cells. These connections occur at a perpendicular angle, minimizing multiple innervations from the same axon (Napper and Harvey, 1988)(**Figure 3C**). Thus, the particular circuit requirements between the granule cells and Purkinje cell are elegantly reflected by the morphology of the two neurons.

1.1.2 Dendrite development

Dendritic arbor development occurs on the scale of days to weeks; however, growth of individual dendrites can occur much faster, with some cell types showing dendrites undergoing multiple rounds of extensions and retraction prior to stabilization. The formation of a dendrite encompasses several steps (**Figure 4A**), including initiation, elongation, and stabilization/retraction, all of which impact the shape, size, localization, and integration of the arbor into the neural circuit (Lefebvre et al., 2015). Many factors have been shown to contribute to one or more of these steps, including energy and material reserves (Fukumitsu et al., 2015), sensitivity to growth factor gradients (Smith et al., 2012), response to contact with permissive/prohibitive surfaces, and neuronal activity (Miller and Kaplan, 2003)(**Figure 4B**).

While it is not surprising that the difference between simple, sampling, and space-filling dendritic arbors is largely impacted by intrinsic programming, live imaging studies have highlighted the importance of intrinsic programming in generating morphological dendritic diversity by demonstrating differences in dendrite initiation, elongation, and stabilization/retraction among neuronal subtypes. Intrinsic differences in dendrite initiation are well represented by the difference between pyramidal neurons, which sprout new branches from the side of preexisting dendrites (Dailey and Smith, 1996), and Purkinje cells that grow new branches by bifurcation of dendrite tips (Fujishima et al., 2012)(**Figure 5**). What determines whether dendrite formation is to occur by bifurcation or collateral sprouting is still unknown. Differences in intrinsic programming can also be observed within arbor types that display similar features. For example, dendritic growth of cortical neurons in layers 4 and 6 show opposite

A**B**

		Dendritic growth and Branching	Dendritic self-avoidance and pruning	Postsynaptic differentiation and spine development
Extrinsic Factors	Secreted cues	BDNF, NT3, NT4/ Trks GDNF/GFR α 1/NCAM HGF/Met BMPs NRG1/ErbB2-4 Wnts Sema3A (directional growth) Slit/Robo Reelin	Slit2/Robo2*	BDNF/TrkB GDNF/GFR α 1/NCAM HGF/Met NRG1/ErbB2/4
	Contact-mediated cues	Celsr2/3 Protocadherins Integrin α 3 DSCAM L1CAM	EphrinA5/EphA7 EphB/EphrinB3 Cadherin Fat3 γ Protocacherin* DSCAM* Integrins	Integrin β 1 Integrin α 3/ α 5 DSCAM Sidekick EphB/EphrinB3
	Neuronal activity and calcium signaling	NMDARs VSCC CamKI/CamKII α /CamKIV MAPK	NMDAR2B CamKII β VSCCs	NMDAR VSCC CamKK/CamKI CAMKv

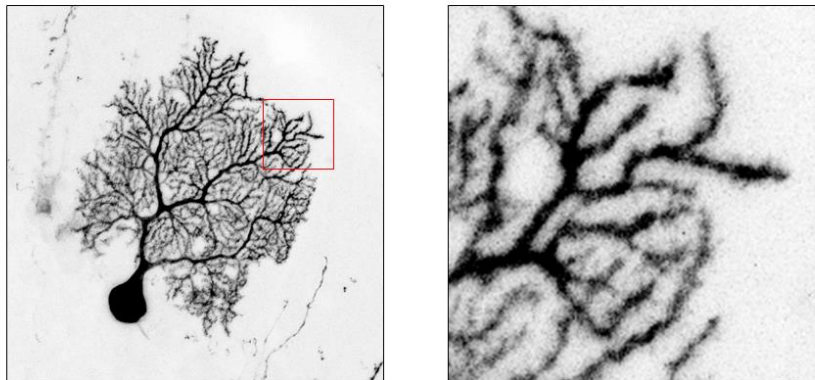
C

Figure 4. Regulators of dendritic arborization.

(A) Important processes for establishment of dendritic arbors. **(B)** Summary of extracellular factors regulating dendrite development. Asterisk indicates molecules that mediate dendritic self-avoidance. **(C)** Example of Purkinje cell showing dendrite self-avoidance. (A and B) modified from Ledda and Paratcha (2017), with permission.

responses to BDNF and NT-3 (McAllister et al., 1997). Further specification within general intrinsic programming is the stabilization/retraction responses in cells showing dendritic self-avoidance. In order to prevent intra-dendrite crossing, Purkinje cells switch self-avoidance behaviors during dendritic arbor development (Fujishima et al., 2012). At earlier stages, in which the more proximal dendrites are being formed, contact with a neighboring dendrite results in retraction. At later stages, when the more distal dendrites are being formed, contact results in a stalling of growth and dendrite stabilization.

In neurons showing space-filling, self-avoiding dendritic patterning, environmental sensing is very important to prevent dendritic crossing either with dendrites from the same neuron or from other neighboring neurons. Contact-dependent stalling of growth has been shown to be a conserved mechanism in many types of neurons (Emoto et al., 2006; Fujishima et al., 2012; Grueber et al., 2003; Han et al., 2012; Smith et al., 2012). At present, only a few mammalian molecules have been identified to be involved in dendritic self-avoidance, and all have been demonstrated to convey their self-avoidance effects via restriction to the membrane. Protocadherins (Ing-Esteves et al., 2018; Lefebvre et al., 2012) appear to confer single cell identity by extensive alternative splicing. DSCAM was suggested to inhibit self-adhesive signals among cells of the same type (Fuerst et al., 2009), and both the Plexin A4/Semaphorin 6A and Robo2/Slit2 signaling cascades may function as cell autonomous repulsion factors (Gibson et al., 2014; Matsuoka et al., 2012). Of surprise was the report that unlike conventional secreted Slit signaling, signaling between a membrane-anchored Slit2 and its receptor Robo2 was shown to be involved in this self-avoidance behavior.

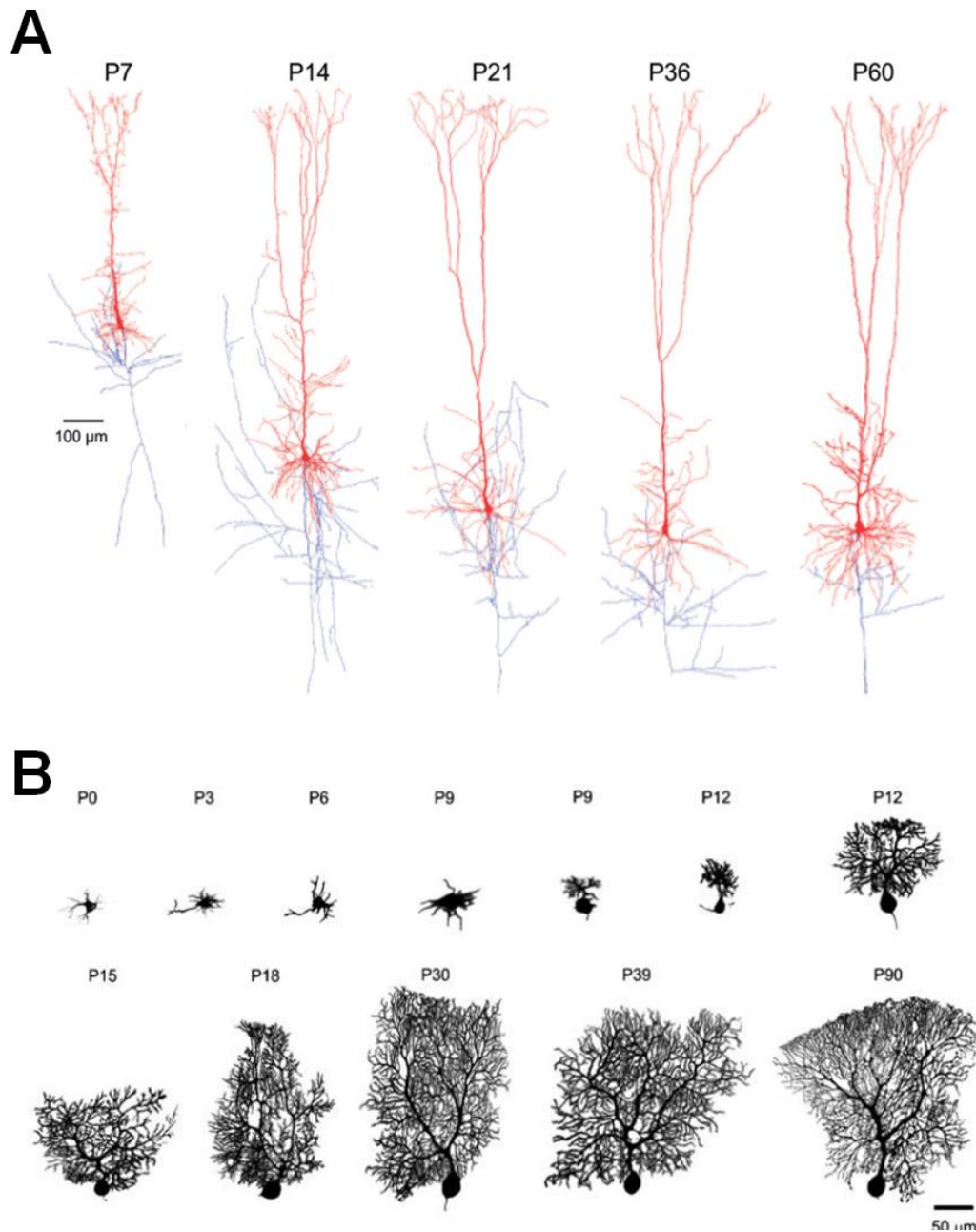


Figure 5. Neurons show different strategies of dendrite development.

(A) Illustration of cortical pyramidal neuron development characterized by rapid dendritic (red) growth and lengthening followed by addition of collateral dendrites proximal to the soma. Axons are shown in blue. Modified from Ramaswamy and Markram (2015), with permission. **(B)** Rat Purkinje cells display transient stellate dendrites before becoming polarized at P9, followed by progressive dendrite extension at the distal tips. Axons not shown. Modified from McKay and Turner (2005), with permission.

In addition to the identification of molecules required for recognition of contact, more detailed aspects of how space filling neurons regulate dendritic growth remain to be clarified. This includes how neurons regulate the dynamics of local environmental exploration, the threshold for both sensing contact and triggering a response, as well how these signals are converted into different outcomes and the signaling cascades involved.

1.1.3 Dendritic protrusions (spines, filopodia)

During dendrite formation, some neuronal types will simultaneously begin to form numerous small, actin-filled protrusions on the dendritic shafts that persist throughout adulthood. Dendritic protrusions during early development have been attributed to a variety of roles, such as functioning as environmental sensors, spine precursors, and dendrite precursors, depending on the neuron type and location on the dendrite (Dent et al., 2007; Fujishima et al., 2012; Heiman and Shaham, 2010; Lohmann and Bonhoeffer, 2008; Niell et al., 2004; Ziv and Smith, 1996)(**Figure 6A-C**). These functions have been shown to be dependent on the environmental-sensing capability of the protrusion, similar to canonical filopodia, to find either presynaptic partners or sense a permissive environment for dendrite formation. Likely to facilitate this environment exploration, protrusions are extremely dynamic structures, showing a high rate of morphological change, motility, and turnover that slows down with maturation.

In mature neurons, dendritic protrusions largely consist of spines: constricted compartments that house the postsynaptic machinery required for converting an extracellular chemical signal into an electrical signal. Spines are also highly dynamic structures, and their turnover and change in size are known to reflect synaptic strength (Alvarez and Sabatini, 2007). Consistently, numerous studies have established that dendritic protrusion morphological changes depend on developmental stage, neurological activity, and disease state (Hotulainen and Hoogenraad, 2010; Yuste and Bonhoeffer, 2004).

Dendritic protrusions are often classified into four groups according to morphological criteria in an attempt to distinguish immature and mature protrusions:

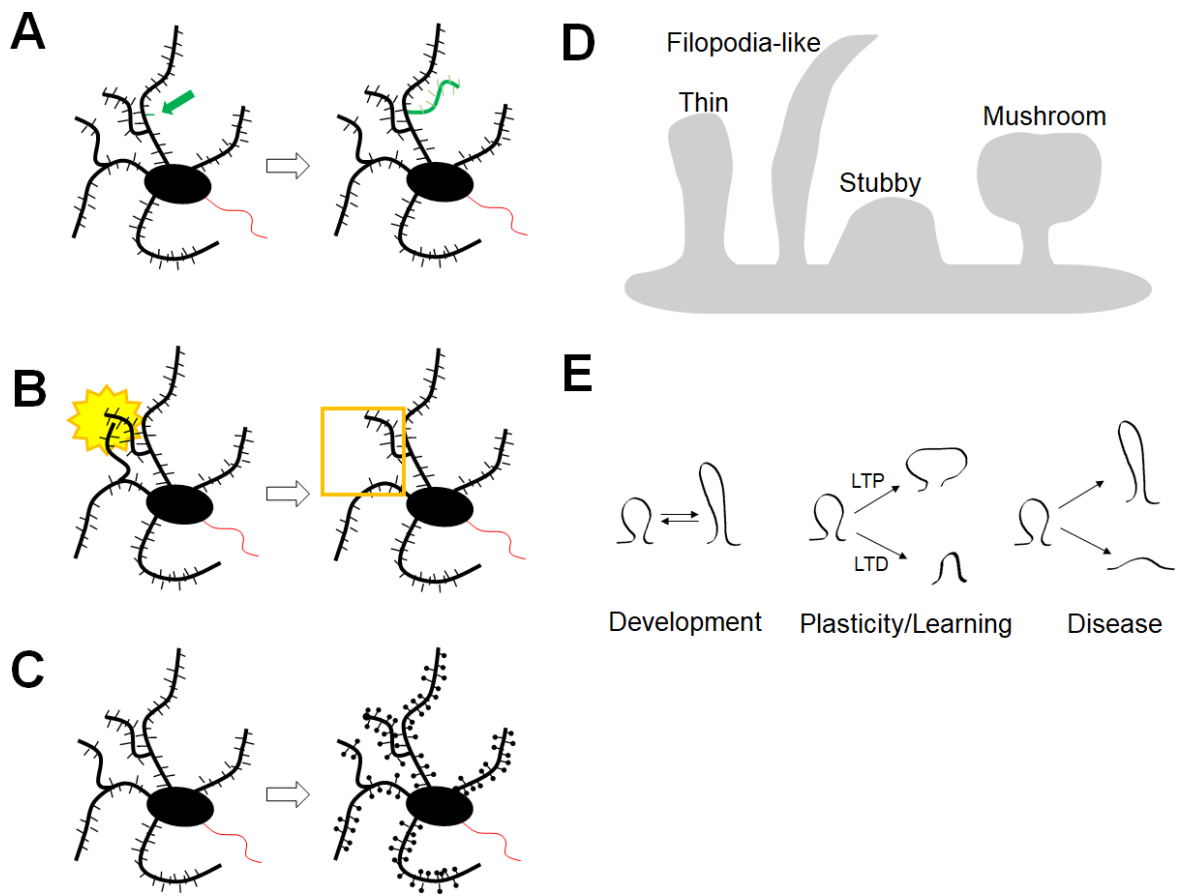


Figure 6. Dendritic protrusions show diverse functionality and morphology.

Dendritic protrusions in developing neurons have been observed to **(A)** function as dendrite precursors, **(B)** function as environmental sensors, and **(C)** function as spine precursors. **(D)** Dendritic protrusions are commonly classified into four shapes. **(E)** Dendritic protrusions undergo morphological change in response to development, synaptic strength, and disease.

filopodia-like, thin, stubby, and mushroom-like (**Figure 6D**). Together these protrusions range in length from 0.5-4 μm with widths of as little as 100 nm in the case of filopodia and mushroom-like spine necks. Unfortunately, there have been no markers reported able to distinguish among these commonly used categories. Due to their frequent change in morphology, dendritic protrusions may be better viewed as existing on a spectrum, and able to fluidly change from one category to another (Nägerl et al., 2004; Parnass et al., 2000) (**Figure 6E**).

Purkinje cell dendritic protrusion classification has been reported in several studies, and differ significantly from the more commonly studied hippocampal or cortical spines (González-Burgos et al., 2011; Lee et al., 2004). The proportion of spines with “thin” or filopodia-like morphology, which are generally described as less-mature spines in pyramidal cells, is much higher in mature Purkinje cells, and “mushroom”-shaped spines are less distinct. Therefore, in this study I do not distinguish among the categories in an attempt to count protrusion density in an unbiased manner.

1.2 MTSS1

1.2.1 MTSS1 structure and domains

Metastasis Suppressor 1 (MTSS1), also known as Missing-in-Metastasis (MIM), is a 745-residue multi-domain protein first named due to its downregulation in several cancers (**Figure 7A**). It is a member of the Bin -Amphiphysin- Rvs (BAR) superfamily, comprising proteins that contain a relatively conserved domain able to dimerize and induce membrane curvature, both in vitro and in vivo (Zhao et al., 2011). The inverse-BAR domain (I-BAR), so named due to its ability to bend membranes in the direction opposite of other BAR proteins, was first characterized in MTSS1 and IRSp53 (Yamagishi et al., 2004). The I-BAR domain dimerizes and binds to the plasma membrane's inner leaflet, inducing convex ("negative") membrane curvature, or outward protrusions in cells (Mattila et al., 2007) (**Figure 7B**). The I-BAR domain was shown to bind to phosphoinositide-rich regions of membrane (Mattila et al., 2007), as well as to be able to accumulate PI(4,5)P₂ clusters (Saarikangas et al., 2009). This ability to accumulate PI(4,5)P₂ was shown to be important for assembly of actin-regulating machinery, demonstrating an indirect regulation of actin via the I-BAR domain (Saarikangas et al., 2015). Furthermore, this I-BAR domain was shown to have a splicing isoform-dependent ability to upregulate Rac1 activity and localize it to the membrane (Dawson et al., 2012a). Interestingly, in HeLa cells stimulated with stromal cell-derived factor 1 (SDF-1), both MTSS1 and its I-BAR truncate could associate with Rab7, presumably via complex formation on endo-lysosomal vesicles (Li et al., 2017). This demonstrated that the I-BAR domain could be "activated" to associate with certain membranes, or if viewed in the opposite direction, suggests that despite containing the I-BAR domain, MTSS1 does not necessarily always associate with membrane.

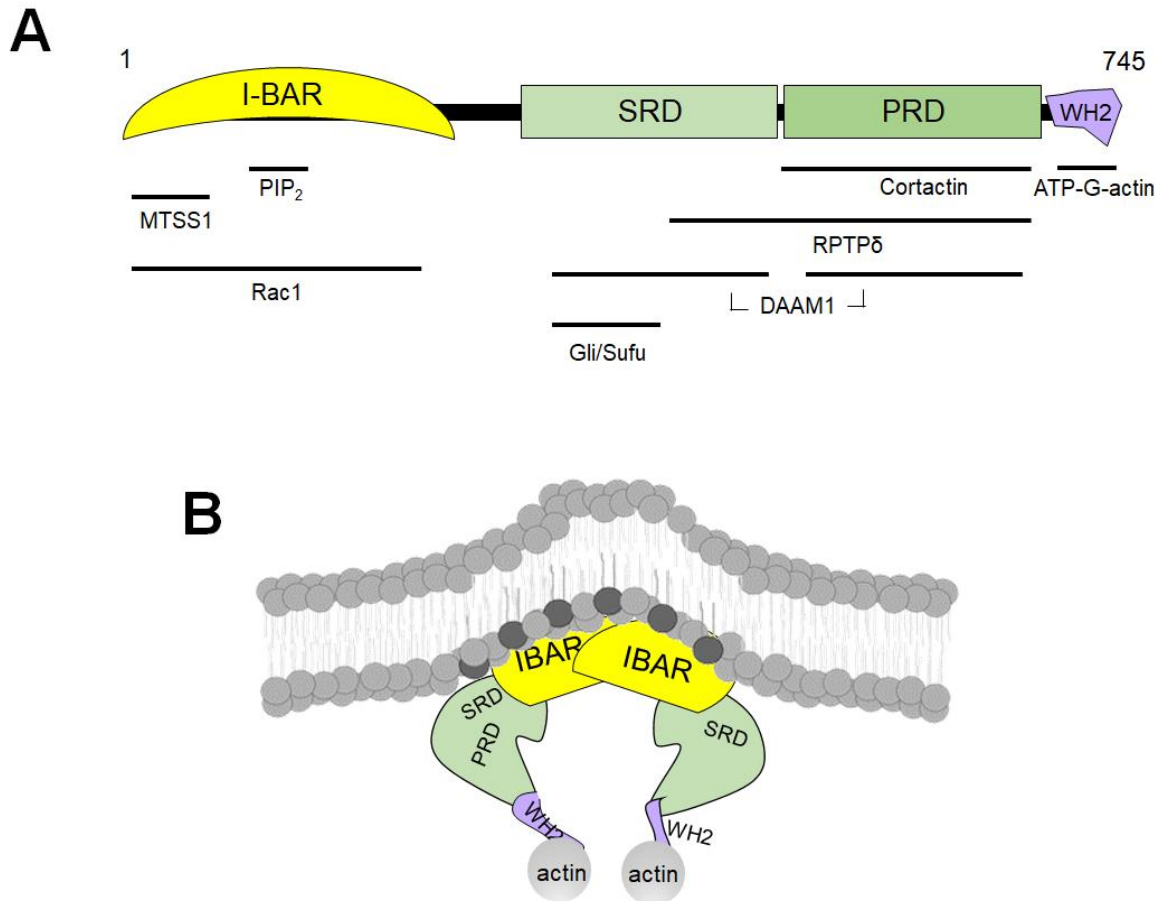


Figure 7. MTSS1 structure and function.

(A) Domain structure of MTSS1 and binding partners identified to date. **(B)** Hypothetical schematic of MTSS1 function in cells. MTSS1 can dimerize and bind to the plasma membrane, accumulating PI(4,5)P₂ (darker lipids) and forming an outward protrusion.

The C terminus of MTSS1 contains the highly conserved Wiskott-Aldrich homology 2 (WH2) domain, an approximately 30-amino acid sequence known to bind to ATP-bound actin monomers with high affinity (Mattila, 2003; Woodings et al., 2003). The WH2 domain is an intrinsically disordered short sequence that folds once bound to actin (Carlier et al., 2013). Because it is often found in proteins that include several actin-regulating motifs, the WH2 domain is associated with a variety of actin-regulating activities; furthermore, it was shown that the sequence N-terminal to the WH2 domain determines whether it facilitates or inhibits F-actin polymerization by its strength of G-actin binding (Chereau et al., 2005; Didry et al., 2012). The WH2 domain in MTSS1 is most similar to the WH2 domains found in verprolin, WIP and actobindin, and its high affinity to ATP-G-actin suggests that while it may participate in barbed-end elongation in in vitro experiments, MTSS1 may sequester G-actin away from other actin-binding proteins in cells (Lin et al., 2005; Mattila, 2003; Woodings et al., 2003).

In addition to the well-characterized I-BAR and WH2 domains, MTSS1 includes domains of high serine (SRD) and proline (PRD) density, which are subject to regulation via multiple kinases and phosphatases (Wang et al., 2007; Zeleniak et al., 2018). Although the structure of this region has not been reported, it has been demonstrated to bind to the ARP2/3 regulator cortactin (Lin et al., 2005), the transcription factor Gli and its regulator Sufu of the Sonic Hedgehog pathway (Callahan, 2004), the formin DAAM1 (Liu et al., 2011), and the phosphatase RPTP δ (Gonzalez-Quevedo, 2005).

1.2.2 MTSS1 Molecular function

MTSS1 is expressed in several organ systems during embryogenesis and maintains strong expression in the adult kidney, liver, leukocytes, and Purkinje cells (Glassmann et al., 2007; Mattila, 2003; Yu et al., 2012), with lower expression in a number of other tissues. MTSS1 was first observed to be down regulated in bladder carcinoma (Lee et al., 2002), and was later categorized as a metastasis suppressor after decreased expression was observed in metastatic breast (Parr and Jiang, 2009), esophageal (Xie et al., 2011), kidney (Du et al., 2012), pancreatic (Zhou et al., 2016), and ovarian (Isaksson et al., 2014) cancers. This was initially largely attributed to the increased cell motility and invasiveness observed when MTSS1 expression was knocked down in cell lines, due to rearrangement of the actin cytoskeleton as well as changes in surface expression levels of various receptors (Li et al., 2017; Lin et al., 2005; Parr and Jiang, 2009; Quinones, 2010; Xie et al., 2011; Yu et al., 2011; Zhan et al., 2016). Furthermore, while increases in proliferation after MTSS1 loss have been reported in breast and esophageal squamous cell carcinoma lines (Parr and Jiang, 2009; Xie et al., 2011), changes in proliferation in response to loss of MTSS1 was shown to be cell type-dependent and even having opposite effects in different non-small cell lung carcinoma cell lines (Ling et al., 2016), making it unclear how MTSS1 may suppress proliferation.

Other studies have shown significant overexpression of MTSS1 compared to normal tissues in primary or early-stage cancers, such as in lung (Kayser et al., 2015), head and neck small cell (Dawson et al., 2012b), and hepatocellular (Ma et al., 2007) cancers, which was then lost with increasing metastatic potential. Although it remains unclear what is regulating this pattern of expression, one study attempting to clarify the role of MTSS1 in these cancers hypothesized that in a cell density-dependent

manner, MTSS1 may regulate the membrane localization of the EGF receptor, which is implicated in several signal transduction cascades that modulate migration, cell adhesion and proliferation (Dawson et al., 2012b). However, several other studies have reported that the upregulation of MTSS1 was correlated with increased metastatic potential in colorectal (Wang et al., 2011) and melanoma (Mertz et al., 2014) cancers. Thus it is clear that the biological role of MTSS1 may be tissue specific and extrapolation of MTSS1 function across multiple cancers should be performed with caution.

Further studies on the biological function of MTSS1 have been explored by generation of four distinct MTSS1 knockout animals (including the one described in this text)(Table 1). Despite the widespread expression of MTSS1 throughout the embryo, homozygous loss of MTSS1 does not result in embryonic lethality, demonstrating that MTSS1 is dispensable for embryonic development. The Finnish and Kansas City models showed consistent findings of kidney function disruption and histological abnormalities, although their molecule mechanisms differed; the former was attributed to disruption in cell junction maintenance, and the latter to increased cell proliferation, although no further exploration was performed (Saarikangas et al., 2011; Xia et al., 2010). On the other hand, there has been no report of kidney dysfunction in the Baltimore model, and instead it was shown to accumulate significant B cell malignancies due to impaired chemokine receptor internalization and motility(Yu et al., 2011, 2012). Despite being the most published, results from the Baltimore model may be difficult to interpret due to the recent report that MTSS1 expression is not fully knocked out in a variety of tissues (Fahrenkamp et al., 2017).

Neural phenotypes have been reported in the Finnish model, which showed widespread behavioral defects that increased with age and spinogenesis disruption

Table 1. Summary of MTSS1 knockout mouse models.

Model	Genotype	Strategy	Decreased lifespan ?	Phenotypes	Neural Phenotypes	Limitations	References
Finnish	Mtss1 ^{-/-}	Gene targeting: stop codon in exon 1	MTSS1 ^{-/-} mice became sick and died at around 8–18 months due to renal failure.	Defects in kidney epithelia intercellular junctions, altered bone metabolism (secondary effect).	Complex but fairly mild behavioral defects. Attenuated excitatory synaptic transmission to Purkinje cells. Morphological defect in spinogenesis.	Expresses truncated form that lacks first 81 amino acids (part of the I-BAR domain) due to use of alternative promoter in intron 3. Does not appear to be expressed in cerebellum, but unknown if expressed in brain.	Saarikangas (2011) Saarikangas (2015)
Kansas City	Mtss1 ^{-/-}	Gene trap: intron 1	no	Extensive renal tubule dilation and cysts.	12 month KO mice rotarod deficiency, death of Purkinje cells around 12 months, granule cell migration defect	Not reported, but may suffer from same limitations as the Finnish model.	Xia (2010) Sistig (2017)
Baltimore	Mtss1 ^{-/-}	Gene trap: intron 3	MTSS1 ^{-/-} died between 14 to 24 mo, presumably related to B-cell malignancies.	Increased propensity to develop aggressive B cell lymphomas (2012) increased hematopoietic stem cell homing (2016).	None reported	Was reported to only decrease MTSS1 levels by 50% due to use of host splice acceptor sequence instead of the delivered sequence.	Yu (2011) Yu (2012) Zhan (2016) Li (2017) Fahrenkamp (2017)
Japan	Mtss1 flox/flox; GluRD2-Cre	Gene targeting: floxed exon 4	no		Morphological defects in Purkinje cell dendrites	Not assessed, but possible expression of exons 1-3 (first 69 amino acids of I-BAR)	Kawabata Galbraith (2018)

(Saarikangas et al., 2015). The Kansas City model also showed an age-dependent decrease in cerebellar-related functions and Purkinje cell death (Sistig et al., 2017). However, it is unclear whether the decreasing kidney function and increasing inability to regulate electrolyte homeostasis may have contributed to these age-dependent changes in behavior.

Other MTSS1 functional studies at the cellular level have shown that although it is implicated in several diverse signaling pathways, its major activity is associated with regulation of actin dynamics as a scaffolding protein. Multiple studies have demonstrated that changes in MTSS1 level consistently lead to actin-based morphological restructuring, such as induction of lamellipodia, membrane ruffles, and filopodia (Bompard, 2005; Gonzalez-Quevedo, 2005; Woodings et al., 2003). Other phenotypes included disassembly of stress fibers (Mattila, 2003; Woodings et al., 2003), accumulation of actin at cell junctions, increase in cell adhesion, and regulation of receptor endocytosis. In addition to the direct effect MTSS1 may have on the cytoskeleton via its WH2 domain, these changes are largely attributed to the number of actin-binding or regulating proteins that interact with the SRD-PRD domains of MTSS1.

Cortactin, an activator of the actin nucleator ARP2/3, has been shown to bind to the PRD of MTSS1, and its activation of ARP2/3 is upregulated in the presence of MTSS1 in vitro (Lin et al., 2005). However, a following study reported MTSS1-dependent indirect downregulation of cortactin due to change in phosphorylation status, obscuring how the direct binding may function in vivo (Bershteyn et al., 2010). DAAM1, a member of the formin family of actin nucleators, was shown to be a binding partner of MTSS1, although the authors did not explore how this binding impacted DAAM1-specific actin dynamics (Liu et al., 2011).

MTSS1 involvement in the positive regulation of the Sonic Hedgehog (Shh) pathway was described in two studies; the first demonstrating MTSS1 binding to the Gli and Sufu transcription factors and mediation of signaling, and the second reporting MTSS1 knockdown-dependent defects in primary cilium formation, known to be the hub of Shh signaling (Bershteyn et al., 2010; Callahan, 2004). While aberrant upregulation of the Shh pathway has been reported in many cancers (Rimkus et al., 2016), it is unclear whether the MTSS1-dependent decrease in Shh signaling may contribute to the metastatic potential of the cancers described above.

1.2.3 MTSS1 in neurons

While the majority of MTSS1 molecular studies have focused on its function in epithelial or cancer cells, only a few studies have explored its function in the brain. In the central nervous system, MTSS1 expression was first noted in Purkinje cells (Mattila, 2003), with increasing expression during the period in which Purkinje cells elaborate their dendritic arbors, and high maintenance throughout adulthood (Glassmann et al., 2007; Hayn-Leichsenring et al., 2011). MTSS1 is also transiently expressed in cerebellar granule cells from the time they are born until they reach their final position in the internal granule layer, around P15-P21, suggesting that MTSS1 may be involved in neuronal migration (Glassmann et al., 2007; Holst et al., 2008). Interestingly, Glassmann and colleagues demonstrated that granule cells exhibited a developmental switch in MTSS1 splicing isoform expression, from using exon 12 to 12a, although it could not be determined whether Purkinje cells also underwent a similar switch.

Subcellular localization of MTSS1 in neurons was first described to be localized diffusely throughout the somatodendritic compartment with minimal axonal localization (Hayn-Leichsenring et al., 2011; Saarikangas et al., 2015). Hayn-Leichsenring and colleagues showed polarized MTSS1 accumulation on the axonal side of the soma; however, no functional assessment of this localization was performed, and since then there have been no reports of this distribution.

The first functional investigation of MTSS1 in neurons was reported in 2015, demonstrating that MTSS1 regulated cytoskeletal dynamics and dendritic spine initiation (Saarikangas et al., 2015). The authors first noted expression of MTSS1 in the pyramidal neurons of the adult hippocampus, and demonstrated that it

accumulated at future dendritic protrusion initiation sites. Using the Finnish MTSS1 knockout mouse, the authors hypothesized that MTSS1-dependent disruption in spinogenesis was an underlying cause of a variety of behavioral and electrophysiological defects observed in this mouse. They further showed that the I-BAR domain was important for binding to the membrane and accumulating PI(4,5)P₂, followed by ARP2/3-dependent actin polymerization and subsequent outward protrusion.

In cerebellar granule cells, overexpression of MTSS1 was shown to increase dendrite formation that could be abrogated either by mutation of the I-BAR domain or inhibition of PI(4,5)P₂ signaling, and reduce dendrite formation when knocked down (Yu et al., 2016). While the requirement of the I-BAR domain and PI(4,5)P₂ signaling was consistent between the two studies, Saarikangas et al. reported that the WH2 domain was dispensable for dendritic protrusion initiation, whereas Yu et al. demonstrated that truncation of the WH2 domain inhibited the MTSS1-dependent increase in dendrite formation. These conflicting results suggested that the importance of the MTSS1 WH2 domain may differ depending on use (dendrite vs dendritic protrusion initiation) and neuron type (hippocampal vs granule cell).

Knockout of MTSS1 in the Kansas City model demonstrated that MTSS1 was indeed required for granule cell migration (Sistig et al., 2017). Mispositioned granule cells could be observed throughout the cerebellar cortex, and cultured cells showed a decrease in migration. The authors reported that cultured MTSS1 knockout granule cells also showed reduced neurite formation, which could be rescued by expression of the exon 12a, but not exon 12, splicing isoform. Furthermore, the authors noted severe Purkinje cell degeneration and cell death at 12 months, which was ablated

when MTSS1 was specifically re-expressed in Purkinje cells. Although Purkinje cell death was not reported in the Finnish mouse, it remains to be clarified if reduced Purkinje cell viability contributes to the later-stage cerebellar-related behavior defects reported earlier.

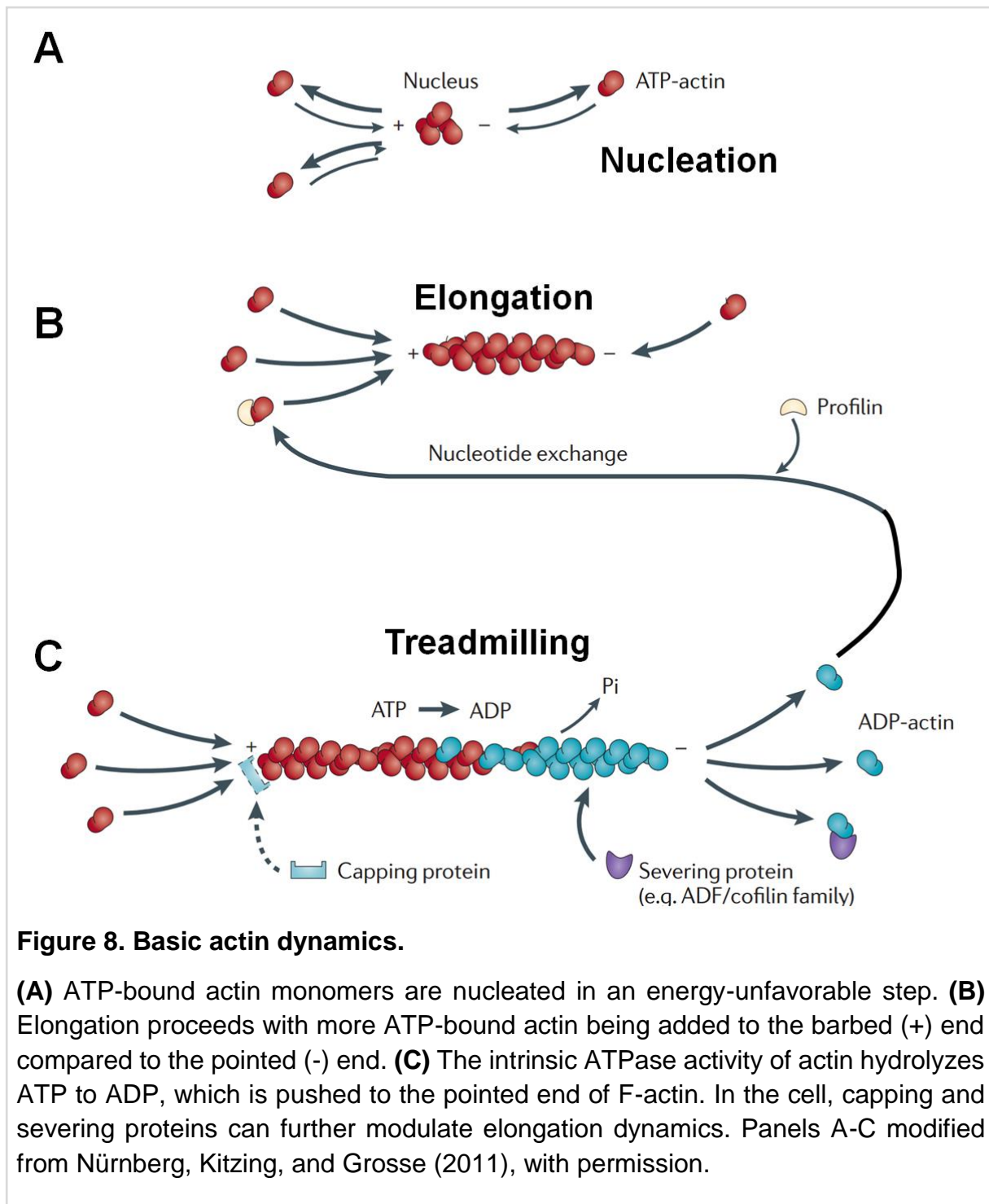
In summary, while neuronal MTSS1 has been shown to be involved in the morphological regulation of several neuronal subtypes, it remains unclear which, and to what extent, the wide range of reported MTSS1 functions is utilized in each of these cells.

1.3 NEURONAL ACTIN

1.3.1 Introduction to actin

Actin is a 43-kDa, ATP-binding protein that can be present either in a monomeric (G-actin) or polymerized (F-actin) state. Actin's highly dynamic turnover between these forms allows rapid F-actin assembly and disassembly that, when combined with further organization into a number of higher-order structures, makes it a highly-responsive and essential component of the cytoskeleton. Actin associates with a vast array of actin-binding proteins (ABPs) that can control F-actin dynamics, localization, and force generation in numerous cellular processes, including provision of physical support, facilitation of signal transduction, generation of mechanical force, and aiding of trafficking and translocation of intracellular components.

In vitro, G-actin can be polymerized from both ends of F-actin; however, due to the inherent polarity of G-actin and orientation of each monomer when polymerized, the two ends of F-actin have different physical properties and thus different critical concentrations (concentration at which G-actin and F-actin remain at equilibrium). F-actin consists of a "barbed" end (or "+" end), at which G-actin incorporation is preferentially incorporated, and a "pointed" end (or "-" end) that has a higher critical concentration leading to a lower rate of G-actin incorporation (**Figure 8A-B**). This difference in critical concentrations leads to polarized F-actin, in which polymerization occurs faster at the barbed end. Although these critical concentrations can be modulated by varying conditions such as divalent cation availability, ionic strength, and nucleotide state of the actin monomer (Carrier et al., 1987; Fujiwara et al., 2007; Gordon et al., 1977; Pollard, 1986), it has been shown that the barbed end always has a lower critical concentration than the pointed end. In physiological conditions, this



contributes to a phenomenon called “treadmilling” in which sections of an F-actin appear to move by preferential addition of G-actin on one end and depolymerization on the other (**Figure 8C**). This treadmilling can be further facilitated by preferential severing of F-actin near the pointed end by proteins such as cofilin and gelsolin.

Polymerization of F-actin can be divided into two steps: the initial nucleation of actin monomers into a short oligomer, followed by subsequent elongation. Nucleation of the first three actin monomers is the most energy-intensive and rate-limiting step due to dimer instability (Sept and McCammon, 2001), and does not occur spontaneously *in vivo* (Pollard, 2007). In physiological conditions, cells require nucleating factors to aid in overcoming this energy barrier. Nucleators include the Arp2/3-complex, which nucleate new F-actin on preexisting F-actin at fixed angles (**Figure 9A**), the formin family that share the conserved FH1-FH2 domains and nucleate linear, unbranched F-actin de novo (**Figure 9B**), and the newly identified WH2-containing nucleators such as Spire and Cordon-Bleu. Thus, nucleation of F-actin is a major strategy in which the cell can control the localization and timing of F-actin formation, as well as the local shape of the actin network (Sept and McCammon, 2001).

On the other hand, the elongation that occurs after nucleation is dependent on incorporation of G-actin at the barbed end and can occur spontaneously at a rate linearly proportional to the concentration of available actin monomers (Pollard, 1986). Although the intracellular concentration of actin has been estimated to be in the order of tens to hundreds of micromolar (Wu and Pollard, 2005), which is many times higher than the barbed end critical concentration, elongation is tightly controlled in cells by

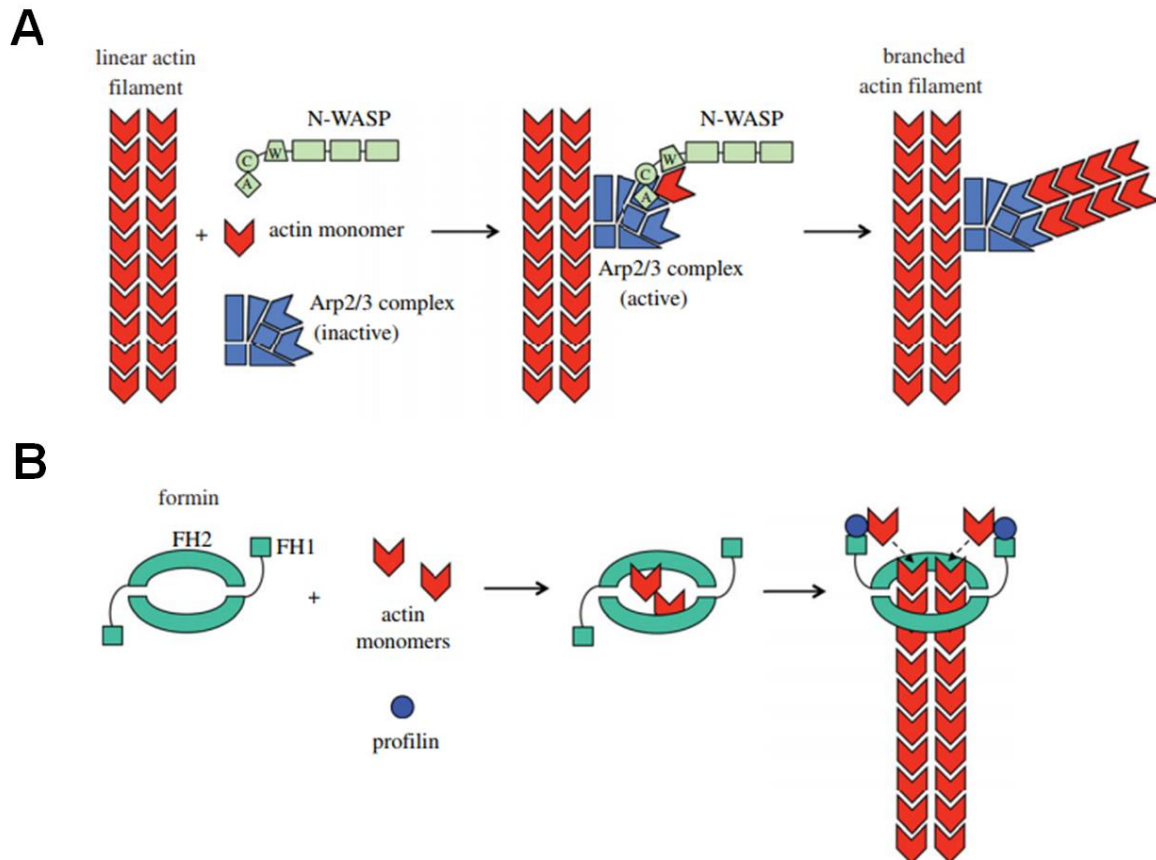


Figure 9. Nucleation of actin.

(A) The ARP2/3 complex nucleates new F-actin on the side of preexisting filaments at a fixed, 70° angle. ARP2/3 requires activation by nucleation promoting factors, such as the pictured N-WASP, as well as WAVE, WASH, and cortactin. **(B)** Formins share conserved FH1 and FH2 domains. When dimerized, the FH2 domain can nucleate F-actin *de novo*, and the FH1 domain binds to profilin-actin complexes and processively elongates F-actin. Modified from Ireton (2013), with permission.

sequestration of the majority of G-actin by monomer-binding proteins such as profilin and thymosin b4, and capping of barbed ends by CapZ or adducin.

Control of the F-actin network in the cell is tightly regulated via coordinated activation and deactivation of actin nucleators, elongators, cappers, and disassembly factors. Recent evidence has suggested a homeostatic interplay among these factors in which ABPs can compete for G-actin or in some cases compensate for one another (Burke et al., 2014; Chesarone and Goode, 2009; Gao and Bretscher, 2008; Rotty et al., 2015; Suarez et al., 2015). Thus, ample care is needed for interpretation of experiments that perturb actin assembly factors or actin levels.

1.3.2 Actin in dendritic protrusions

The actin organization within dendritic protrusions is a topic of intense study due to its important role in the formation and elimination, motility and stability, and morphology of dendritic protrusions in response to a multitude of stimuli (Chazeau et al., 2014; Hotulainen and Hoogenraad, 2010; Luo, 2002). Both linear and branched F-actin are found throughout the entire spectrum of dendritic protrusion morphologies (Korobova and Svitkina, 2010). Replica electron microscopy of dendritic filopodia have shown actin structure fairly dissimilar to that of canonical filopodia, containing unbundled, bidirectional arrangements of F-actin (Korobova and Svitkina, 2010)(**Figure 10A**). This suggested the presence of actin binding proteins in dendritic filopodia not normally ascribed to canonical filopodia, such as multiple nucleation factors and myosin contractibility (Hotulainen et al., 2009; Wegner et al., 2008). It is hypothesized that this arrangement facilitates the rapid morphological changes observed in dendritic protrusions, such as spine head formation and neck constriction (**Figure 10B**).

Consistently, a number of recent studies have demonstrated the importance of both branched and linear F-actin nucleation for achieving dendritic protrusion morphology (Glebov and Burrone, 2016; Hotulainen et al., 2009; Miermans et al., 2017; Spence et al., 2016). It is generally believed that the more filopodia-like dendritic protrusions rely on actin nucleated by linear actin nucleators such as formins, whereas change into a more bulbous spine shape depends on relatively higher activity of the branched-actin nucleator ARP2/3 (**Figure 11A**). Furthermore, recent observations have suggested that in the small volume of such dendritic protrusions, the presence of multiple actin nucleators may compete with one another for available monomeric actin, resulting in mutual inhibition

How these different nucleators function in the developing dendritic protrusion remains to be clarified, particularly in the early stages when most protrusions appear filopodia-like. The dynamic extensions and retraction of thin, filopodia-like dendritic protrusions suggests coupling with the concomitant necessity of membrane-bending. In this study, I explored the membrane-bending and actin-binding protein MTSS1 and its involvement in the regulation of two actin-nucleating pathways.

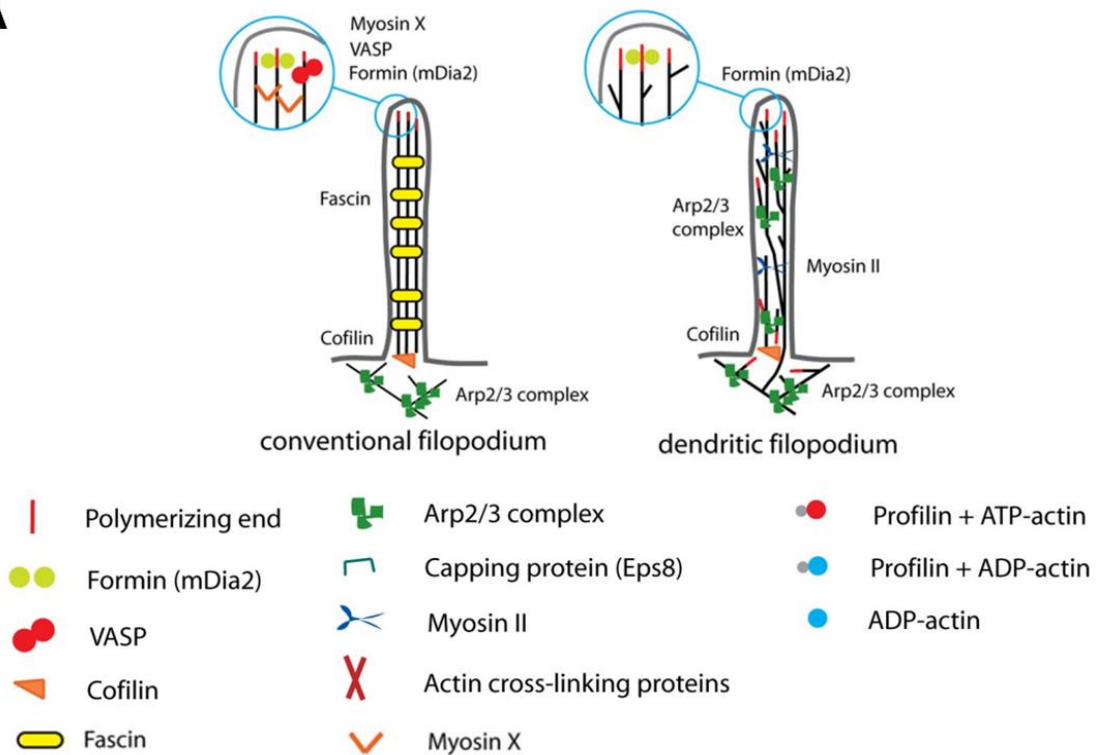
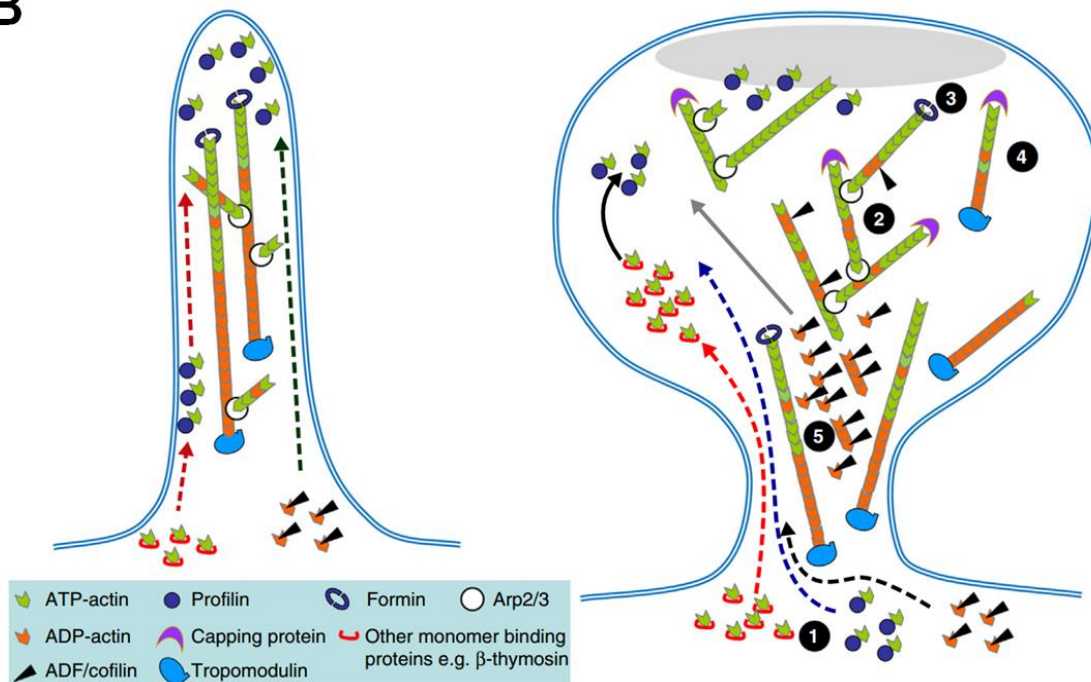
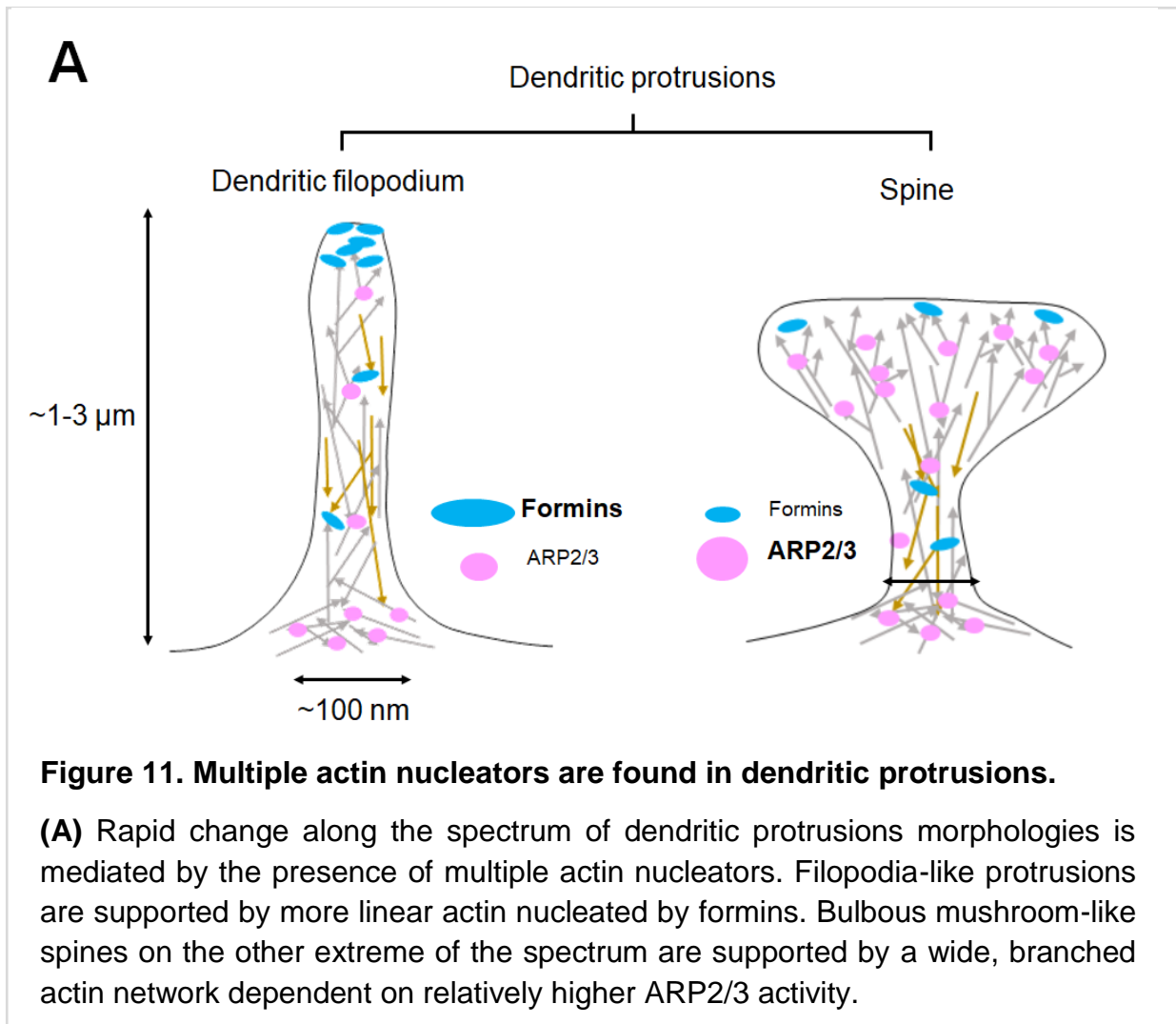
A**B**

Figure 10. Actin organization in neuronal dendritic protrusions.

(A) Although visually similar, the internal actin organization is significantly different between conventional and dendritic filopodia. F-actin in dendritic filopodia are oriented in both directions, unbundled, and nucleated by both ARP2/3 and formins. Modified from Hotulainen and Hoogenraad (2010), with permission. **(B)** In the small volume of dendritic protrusions, actin dynamics are regulated by a number of actin-binding proteins during development. Modified from Lei et al. (2016), with permission.



CHAPTER 2. RESULTS

2.1 CHARACTERIZATION OF MTSS1 LOSS IN PURKINJE CELLS

1.1.1 In vivo loss

To understand the cell-autonomous function of MTSS1 in Purkinje cells, I used MTSS1 conditional knockout (cKO) mice first developed by Masayoshi Mishina's lab (University of Tokyo) in 2011 that was given to the Kengaku lab in 2012. In brief, the fourth exon of *Mtss1* was flanked by two loxP sites, which ensured bypassing the alternative promoter in exon 3 that was reported to result in a truncated form of MTSS1 (Saarikangas et al., 2011). Homologous floxed mice were then crossed with a transgenic Cre line under the control of the *GluR δ 2* promoter. This promoter has been previously used as a Purkinje cell-specific promoter which begins expression around embryonic day 15 (Takayama et al., 1996).

I did not observe late-stage Purkinje cell death as reported in the Kansas City knockout model (Sistig et al., 2017) (**Figure 12A**). Furthermore, I observed no gross anomalies in cerebellar formation or layer formation (**Figure 12B**). While abnormalities in Purkinje cell function often manifests in defects in motor coordination and learning (Cendelin, 2014; Raymond et al., 1996), cKO mice showed no obvious behavioral anomalies associated with major Purkinje cell dysfunction; however, I did not perform any quantitative behavioral analysis. This is consistent with previous reports, in which global loss of MTSS1 did not result in mice showing major motor coordination difficulties, until tested at 1 year with more sensitive tests (Saarikangas et al., 2015; Sistig et al., 2017).

While MTSS1 loss was confirmed in the Mishina lab using antibodies generated in house, I also confirmed loss of MTSS1 expression in Purkinje cells by immuno-

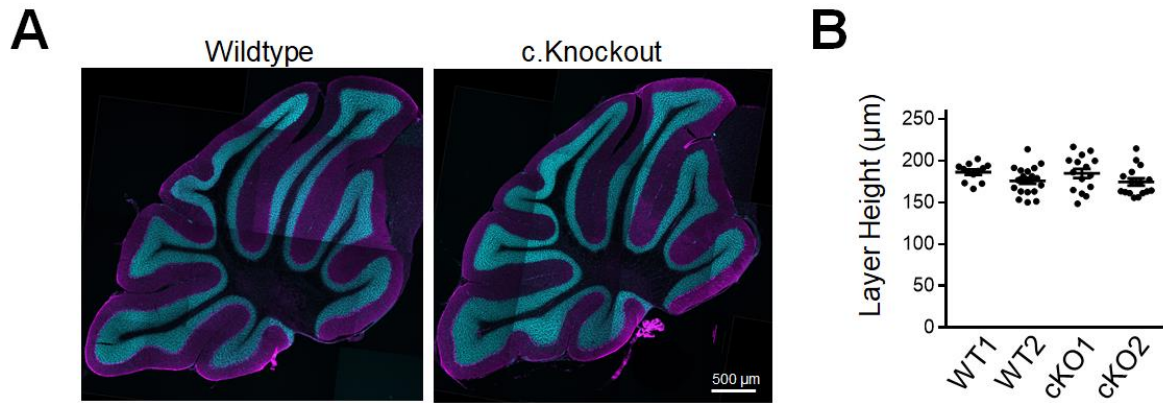


Figure 12. Gross histology of cKO mice is not changed.

(A) Sagittal sections of a 14-month-old WT mouse (left) and 16-month-old cKO mouse (right), stained with the PC-specific marker calbindin (magenta) and DAPI (cyan). No change in size or layer formation can be observed. Neither calbindin-free patches of degenerated PCs nor ectopias of granule cells are seen. **(B)** Quantification of molecular layer height from two WT and two cKO female P35 mice, measured from multiple points in lobes IV-V of mid-sagittal sections show no change. Mean \pm SEM.

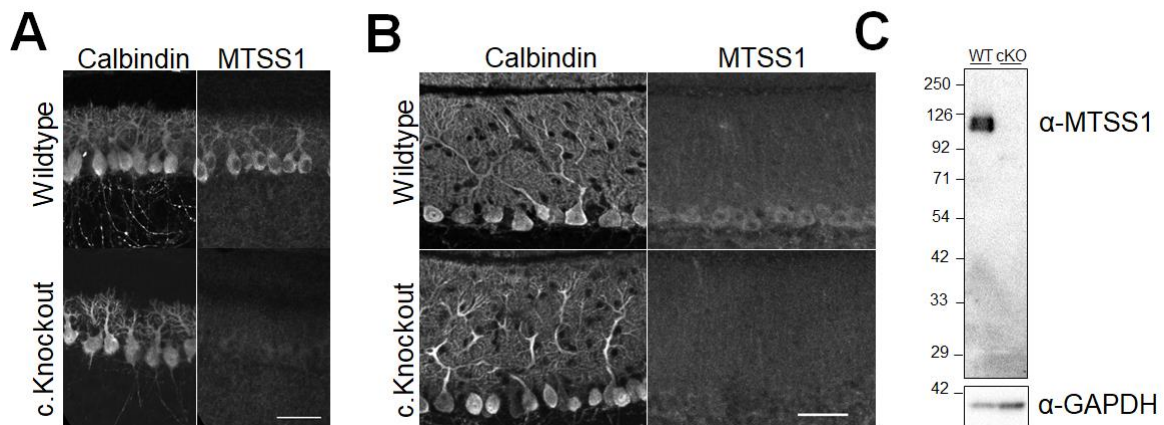


Figure 13. Confirmation of PC-specific MTSS1 knockout.

(A-B) Sagittal cerebellar sections showing endogenous staining of PC marker calbindin and MTSS1 from WT (top) and cKO (bottom) mice at (A) P7 and (B) P14. **(C)** Western blot of cerebellar lysate from 3-month-old WT and cKO mice demonstrating complete ablation of MTSS1 and specificity of anti-MTSS1 antibody. Scale bars 50 µm.

histostaining of cerebellar slices from postnatal days 7 (P7) and P35 mice (**Figure 13A-B**) using a commercial antibody that binds to the C-terminus of MTSS1. This confirmed that our knockout model did not express the truncated form of MTSS1 previously reported in the Finnish knockout model. I further confirmed complete knockout by western blot analysis of cerebellar lysates from 3-month-old mice (**Figure 13C**).

To analyze the in vivo morphology of individual Purkinje cells in cKO mice, I sparsely labeled cells with GFP by performing intracerebellar injection with adeno-associated virus (AAV) carrying a GFP expression construct. Mice were injected at P1 and sacrificed at P7,9,14, and 35 (**Figure 14A**). As early as P7, Purkinje cells clearly showed dendritic morphology defects. Dendritic arbors were smaller in cKO Purkinje cells and the density near the soma appeared lower. At the later stages P14 and P35, reduction in total arbor size was more evident, as was the narrowing of the arbor and loss of dendrites proximal to the soma. Quantification at these time points showed a 40% decrease in total dendritic length (WT, $3530 \pm 189 \mu\text{m}$; cKO, $1970 \pm 142 \mu\text{m}$; mean \pm SEM) and branch points (WT, 233 ± 11 ; cKO, 136 ± 9) at P14 and a 30% decrease in total dendritic length (WT, $6710 \pm 330 \mu\text{m}$; cKO, $4620 \pm 203 \mu\text{m}$) and branch points (WT, 377 ± 10 ; cKO, 254 ± 10) at P35 (**Figure 14B-C**).

Purkinje cells in vivo will generally have a single, easily identifiable, thick dendrite extending from the soma which bifurcates into two daughter branches of equal thickness (**Figure 14D**). I observed that cKO Purkinje cells had much thicker and longer primary dendrites. By P35, it could be observed that cKO Purkinje cells had primary dendrites that appeared much thicker and longer, with bifurcation far from the soma (WT, $36 \pm 4 \mu\text{m}$; cKO, $98 \pm 7 \mu\text{m}$) (**Figure 14E**).

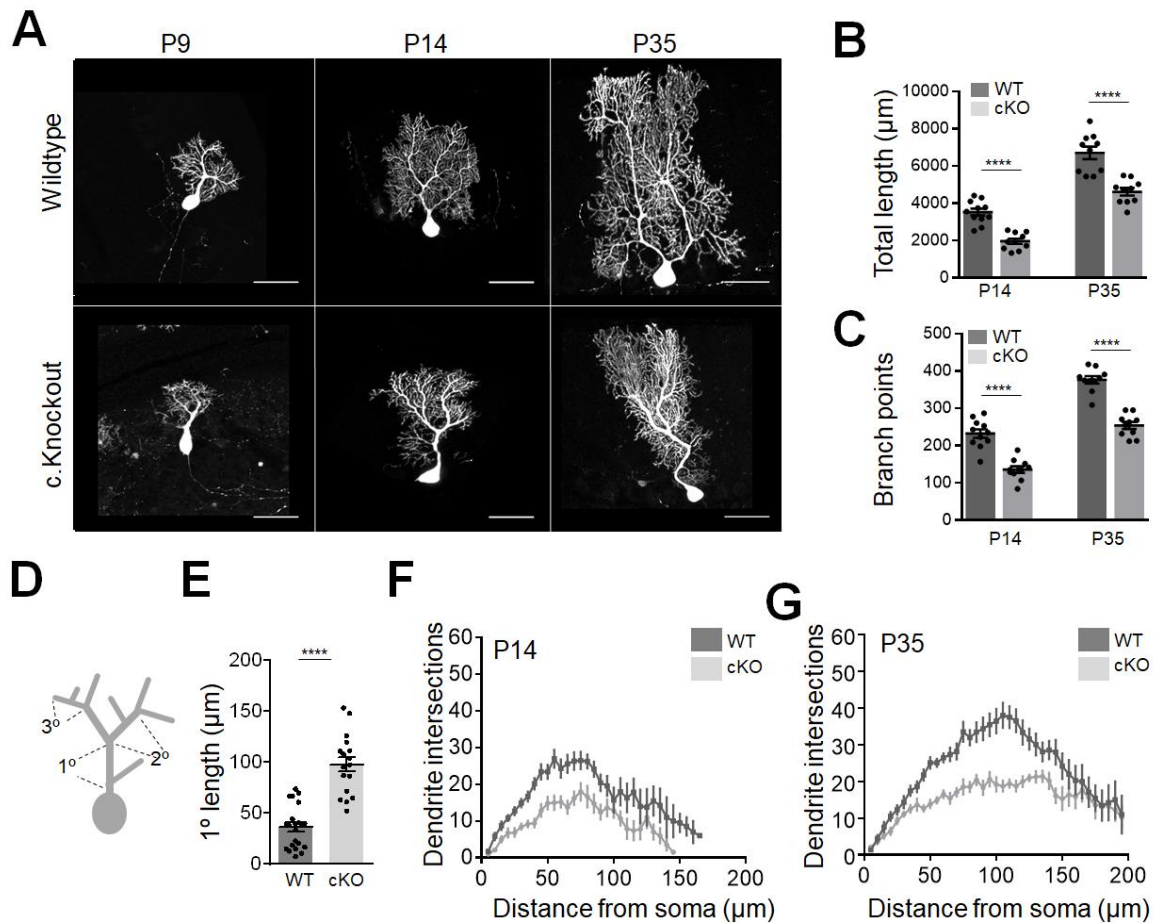


Figure 14. Loss of MTSS1 decreases dendrite complexity in PCs.

(A) Representative images of PCs labelled with AAV-GFP in sagittal cerebellar sections from WT (top) and cKO (bottom) mice at indicated ages. **(B)** Quantification of total dendritic length and **(C)** total number of branch points from AAV-GFP-labelled PCs at indicated ages reconstructed and traced using Imaris software. $n=10-11$ neurons per condition. **(D)** Diagram illustrating PC dendrite classification and **(E)** quantification of primary dendrite length in mature PCs (P35). $N \geq 17$ neurons per condition. **(F)** and **(G)** Sholl analyses of AAV-GFP-labelled PCs reconstructed in Imaris software at ages P14 (F) and P35 (G). $N=9-11$ neurons per condition. All data show mean \pm SEM. Scale bars $50 \mu\text{m}$. **** $p < 0.0001$.

Next, I performed a Sholl analysis, which measures the number of dendritic intersections across concentric circles sharing a common center at the soma. Loss of MTSS1 resulted in a decrease in proximal dendritic density at both P14 and P35 when compared with WT (**Figure 14F-G**). However, the density of dendrites returned to WT levels at distal regions of the arbor. Given that the width of the arbor at distal regions was also generally reduced, this suggested a denser packing of dendrites at the later stage of dendrite development; however, no dendrite crossings could be observed. Instead, I observed that intersegmental length seemed shorter in cKO cells, although this was not quantified.

Observation of Purkinje cells at higher magnification revealed that the dendritic protrusions were noticeably longer in cKO cells (**Figure 15A**). Due to differences in dendritic protrusion morphological classification among neuronal subtypes, I took unbiased measurements of all protrusions without selection of a particular class. Dendritic protrusion length was clearly increased at both P14 (WT, $0.63 \pm 0.01 \mu\text{m}$; cKO, $0.94 \pm 0.01 \mu\text{m}$), and P35 (WT, $0.70 \pm 0.01 \mu\text{m}$; cKO, $0.91 \pm 0.01 \mu\text{m}$) (**Figure 15B**). Most surprising was that loss of MTSS1 showed no significant decrease in dendritic protrusions, as previously reported (Saarikangas et al., 2015)(**Figure 15C**). Because it was reported that the I-BAR domain of MTSS1 was responsible for dendritic protrusion density, I stained cultured Purkinje cells for ABBA1 and IRSp53 (**Figure 16A-B**), both of which contain a highly conserved I-BAR domain (Yamagishi et al., 2004). Although their expression was not restricted only to Purkinje cells, clear localization at the tips of dendritic protrusions could be observed (**Figure 16C-D**). This suggests the possibility that the I-BAR-dependent dendritic protrusion initiation may be mediated by redundant proteins.

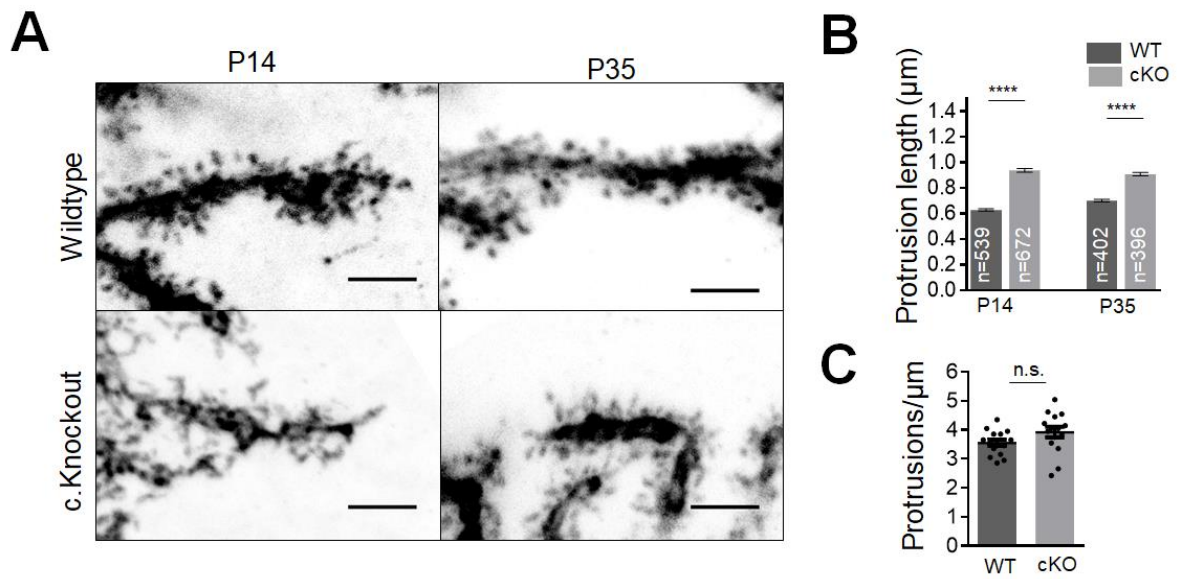


Figure 15. MTSS1 loss increases dendritic protrusion length, but does not affect density in PCs.

(A) Distal dendrites and their dendritic protrusions at indicated ages in WT and cKO PCs labelled with AAV-GFP. **(B)** Quantification of distal dendritic protrusion length in WT and cKO PCs. **(C)** Quantification of distal dendritic protrusion density in P14 mice. All data show mean \pm SEM. Scale bars 3 μ m. **** $p < 0.0001$.

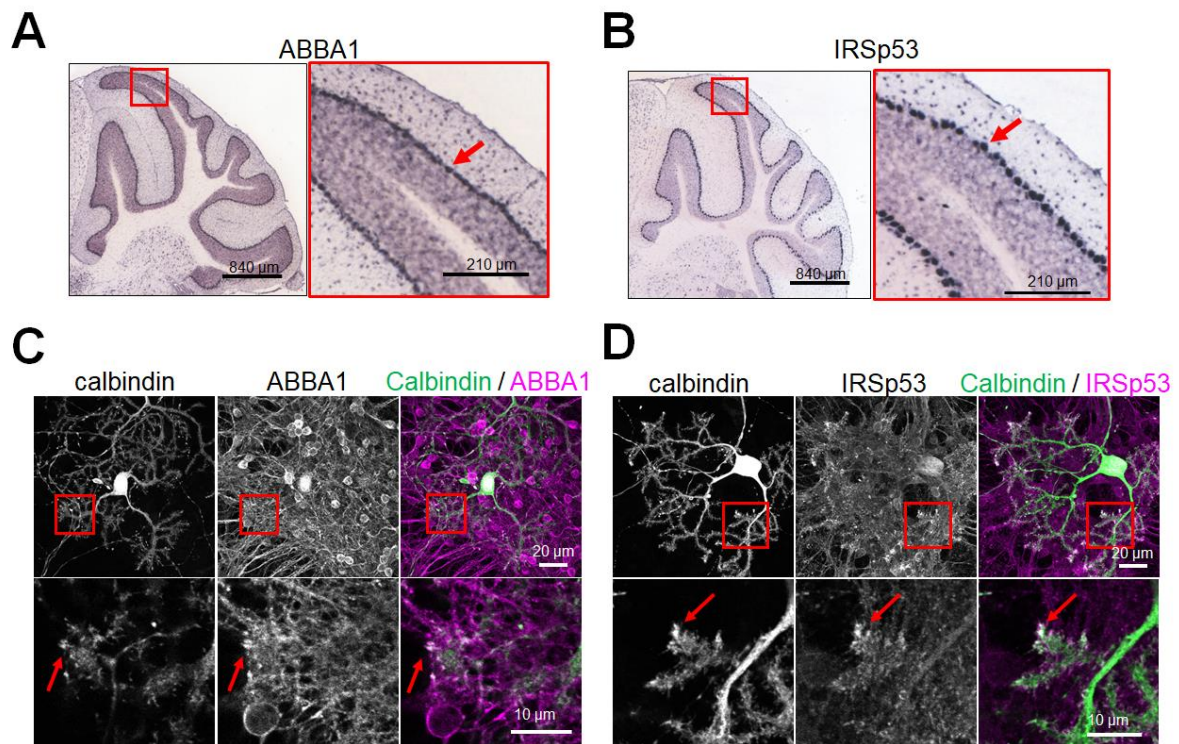


Figure 16. I-BAR proteins are expressed in PCs and show localization in dendritic protrusions.

(A-B) In situ hybridization of P56 mice shows (A) ABBA1, also known as MTSS1L, and (B) IRSp53, also known as BAIAP2, highly expressed in the PC layer (insets). Images from the Allen Brain Atlas. **(C-D)** Immunostaining of (C) ABBA1 and (D) IRSp53 in 15DIV culture confirms expression in PCs. Boxed region and arrow shows localization in dendritic protrusion. Upper images are z-projections to show expression in the soma, lower images are single slices to better visualize the dendritic protrusions.

1.1.2 In vitro loss and live imaging

I next confirmed whether mutant Purkinje cells cultured in vitro showed similar morphological defects as Purkinje cells in vivo. Mutant Purkinje cells expressing GFP in dissociated cerebellar tissue cultures from P0.5 mice showed similar loss of dendritic complexity (**Figure 17A**), with ~60% decrease in total dendritic length and ~55% decrease in branch points at 12 days in vitro (12DIV) (**Figures 17B-C**). While Purkinje cells cultured in vitro often lose polarity and form multiple primary dendrites, cKO Purkinje cells instead showed a decrease in primary dendrite number (-46%) (**Figure 17D**). Of note, cKO Purkinje cells looked morphologically similar to those in vivo, with more obvious loss of branches proximal to the soma.

I performed lower magnification long-term live imaging of growing Purkinje cells in culture to determine whether this MTSS1 loss-dependent decrease in dendrite complexity was due to problems in dendritic initiation and formation or increased retraction. WT neurons imaged from DIV 7-11 started growth with frequent, robust extension of dendrites on several primary dendrites, and showed occasional dendritic retraction. On the other hand, cKO Purkinje cells showed significantly more dendritic retraction despite showing a similar robust growth of dendritic branches (**Figure 18A**). Quantification of individual branch dynamics showed increased extension speed in cKO cells and no change in bifurcation until later in development, likely reflecting the increased branch density observed at distal regions (**Figure 18B-C**). These results suggested that the arbor phenotype observed was a result of increased retraction proximal to the soma and not a transient reduction in dendrite formation. Using Sholl analysis I observed the peak of dendrite intersection in WT cells gradually broaden, reflecting the addition of new dendritic segments by bifurcation of the dendritic tips.

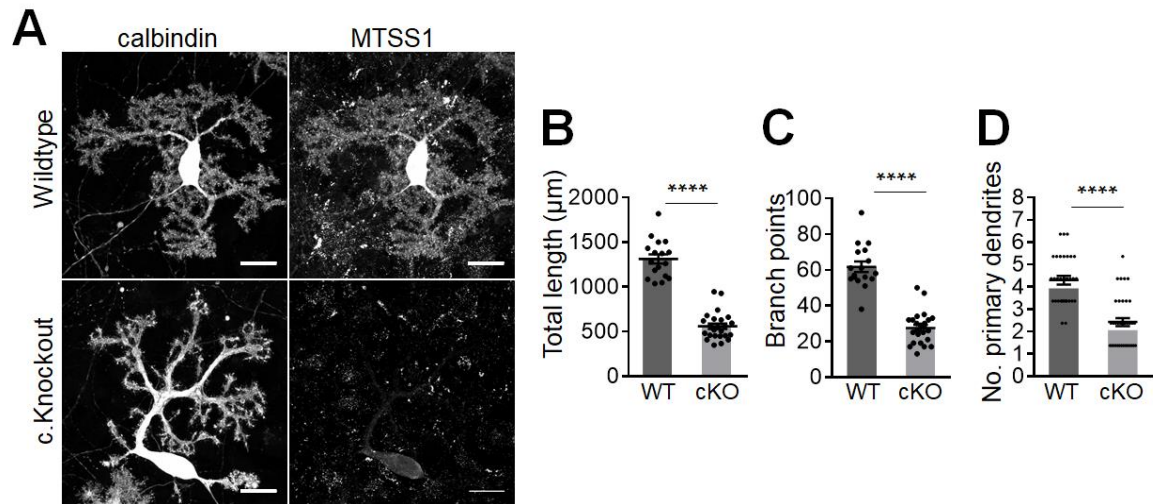


Figure 17. Cultured cKO PCs show similar decrease in dendritic complexity.

(A) Representative images of PCs transfected with GFP in dissociated cerebellar cultures of WT (left) and cKO (right) mice at 12DIV. **(B-D)** Quantification of total dendritic length (B), number of branch points (C) and primary dendrites (D). N=17-24 neurons per condition. All data show mean \pm SEM. Scale bars 20 μm . **** $p < 0.0001$.

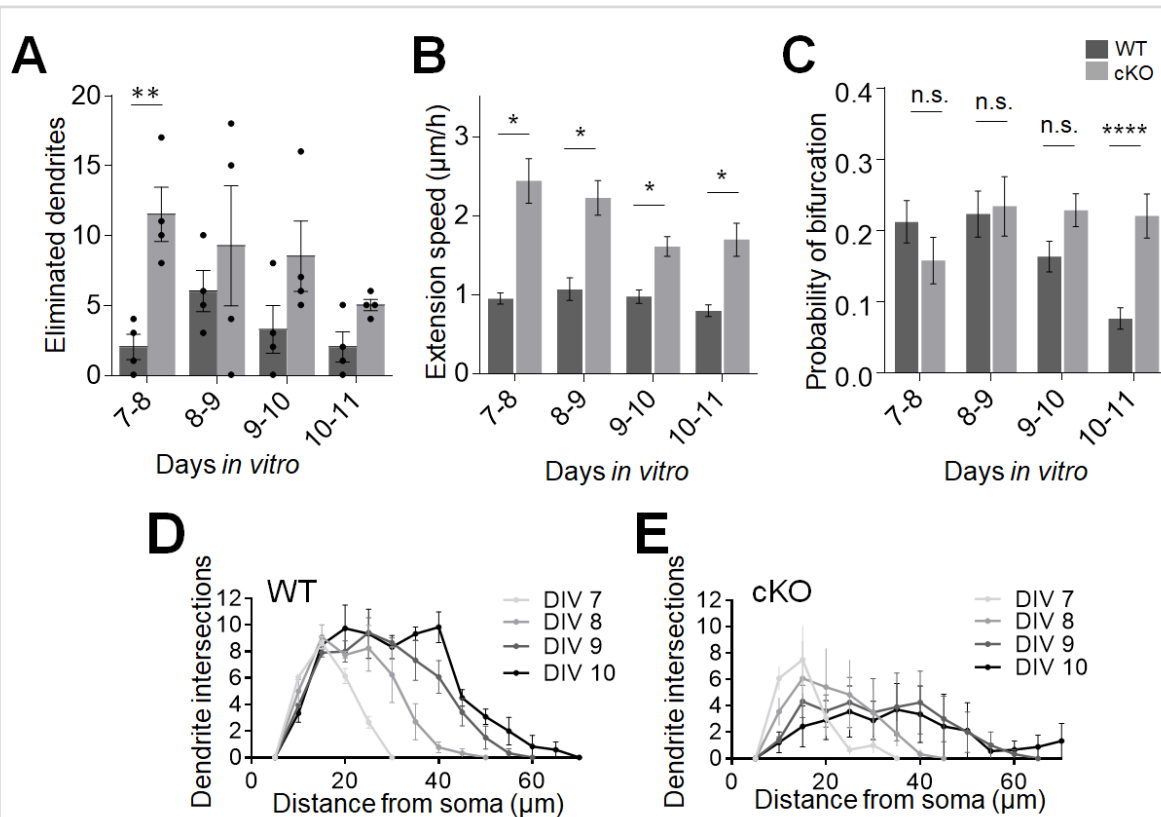


Figure 18. Live imaging showed increased dendrite retraction in cKO PCs.

(A) Quantification of eliminated dendrite events observed during time-lapse imaging of PCs. One event was counted on the last frame of retraction. 4 neurons per condition. (B) Quantification of rate of elongation for extending dendrites. $n=18-27$ branches for each DIV and phenotype. (C) Quantification of the probability a dendrite would bifurcate in a given day. The tip of a dendrite that showed growth from 7DIV to 11DIV was tracked, and probability was calculated as the fraction of frames a bifurcation event was observed in a given day. $n=23$ branches for both WT and cKO, mean \pm SEM. (D-E) Time-dependent Sholl analyses of developing PCs in WT (D) and cKO (E) cultures observed during time-lapse imaging. $n = 4$ per condition. All data mean \pm SEM. * $p < 0.05$, ** $p < 0.01$, **** $p < 0.0001$.

On the other hand, cKO cells showed a marked reduction of dendrite density proximal to the soma as the cell developed (**Figure 18D-E**).

Similar to Purkinje cells in vivo, cultured cells showed dendritic protrusions much longer than wildtype Purkinje cells (**Figure 19A**). Measurement showed cKO Purkinje cells were also significantly longer than WT cells (WT, $0.98 \pm 0.02 \mu\text{m}$; cKO, $1.60 \pm 0.03 \mu\text{m}$), and the range of lengths was significantly increased (**Figure 19B**). Live imaging showed that these dendritic protrusions were highly dynamic with frequent extension and retraction, suggesting that the observed range of dendritic protrusion lengths was more reflective of the spectrum an individual dendritic protrusion may take on.

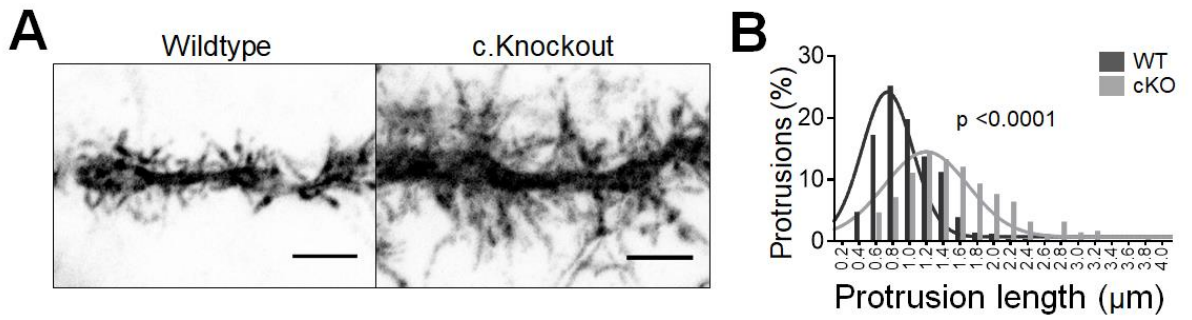


Figure 19. Dendritic protrusions in cKO PCs showed significant increase in length.

(A) Representative images of distal dendritic segments from PCs transfected with GFP in dissociated WT (left) and cKO (right) cerebellar cultures at 12DIV. **(B)** Distribution of WT ($n = 540$) and cKO ($n = 572$) dendritic protrusion lengths in 12DIV PCs. Scale bars 3 μm .

1.1.3 MTSS1 truncate rescue experiments

To better understand the role MTSS1 may be playing in Purkinje cells, I performed rescue experiments using full-length and truncated forms of MTSS1 transfected into cKO Purkinje cells at 0DIV (**Figure 20A-D**). By 12DIV, cKO cells transfected with full-length GFP-tagged MTSS1 showed dendritic complexity similar to that of WT cells transfected with GFP, and was significantly increased compared to cKO cells transfected with GFP only (WT + GFP, $1312 \pm 52 \mu\text{m}$; cKO + GFP, $560 \pm 32 \mu\text{m}$; cKO + MTSS1, $1396 \pm 51 \mu\text{m}$). Expression of the N-terminal I-BAR domain on the other hand did not rescue the cKO phenotype, and rather exasperated the polarized morphology (cKO + I-BAR, $611 \pm 63 \mu\text{m}$). Expression of the C-terminal portion of MTSS1, which includes the SRD, PRD, and WH2 domains, showed rescue of the dendritic phenotypes; however, the dendrites were still slightly reduced in complexity compared to WT cells (cKO + C-MTSS1, $1070 \pm 58 \mu\text{m}$). Further removal of the WH2 domain maintained the ability to rescue the dendritic phenotype (cKO + C-MTSS1 Δ WH2, $1376 \pm 97 \mu\text{m}$), demonstrating that loss of MTSS1's WH2 domain did not underlie the morphological phenotype observed in cKO Purkinje cells, and that the SRD-PRD portion of MTSS1 was important for dendritic development.

Further examination at higher magnification showed full-length GFP-MTSS1 localized throughout the dendritic arbor and accumulation in dendritic protrusions, although with no clear membrane localization (**Figure 21A-B**). cKO Purkinje cells expressing moderate levels of GFP-MTSS1 showed complete rescue in dendritic protrusion length (WT, $0.98 \pm 0.02 \mu\text{m}$; cKO + GFP, $1.60 \pm 0.03 \mu\text{m}$; cKO + MTSS1, $1.02 \pm 0.02 \mu\text{m}$). As expected, GFP-I-BAR was highly localized to the membrane and induced very thin, long dendritic protrusions in cKO Purkinje cells ($1.76 \pm 0.04 \mu\text{m}$),

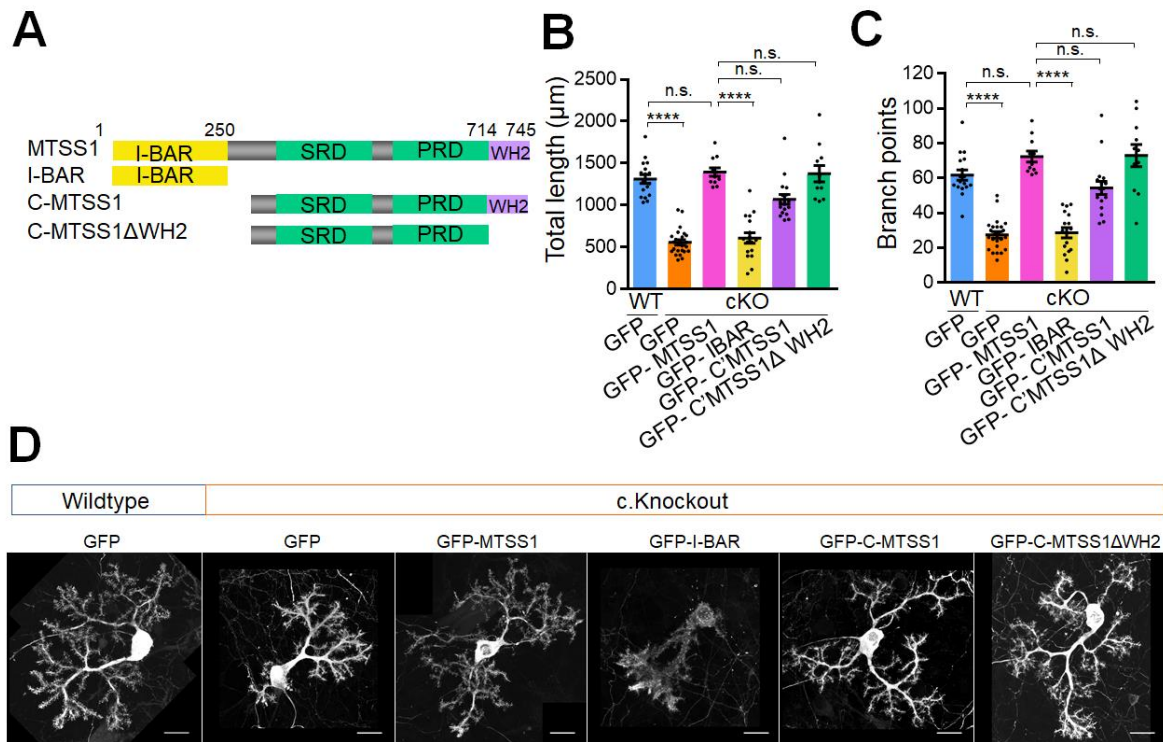


Figure 20. Expression of the SRD-PRD domains of MTSS1 rescues the cKO dendritic phenotype.

(A) Schematic of MTSS1 constructs. **(B-C)** Quantification of total dendritic length (B), and total number of branch points (C), N= 11-24 neurons per condition. **(D)** Representative images showing GFP signal of 12DIV WT and cKO PCs in dissociated cerebellar cultures, transfected at 0DIV with GFP or GFP-MTSS1 constructs. All data show mean \pm SEM. Scale bars 20 μ m. **** $p < 0.0001$.

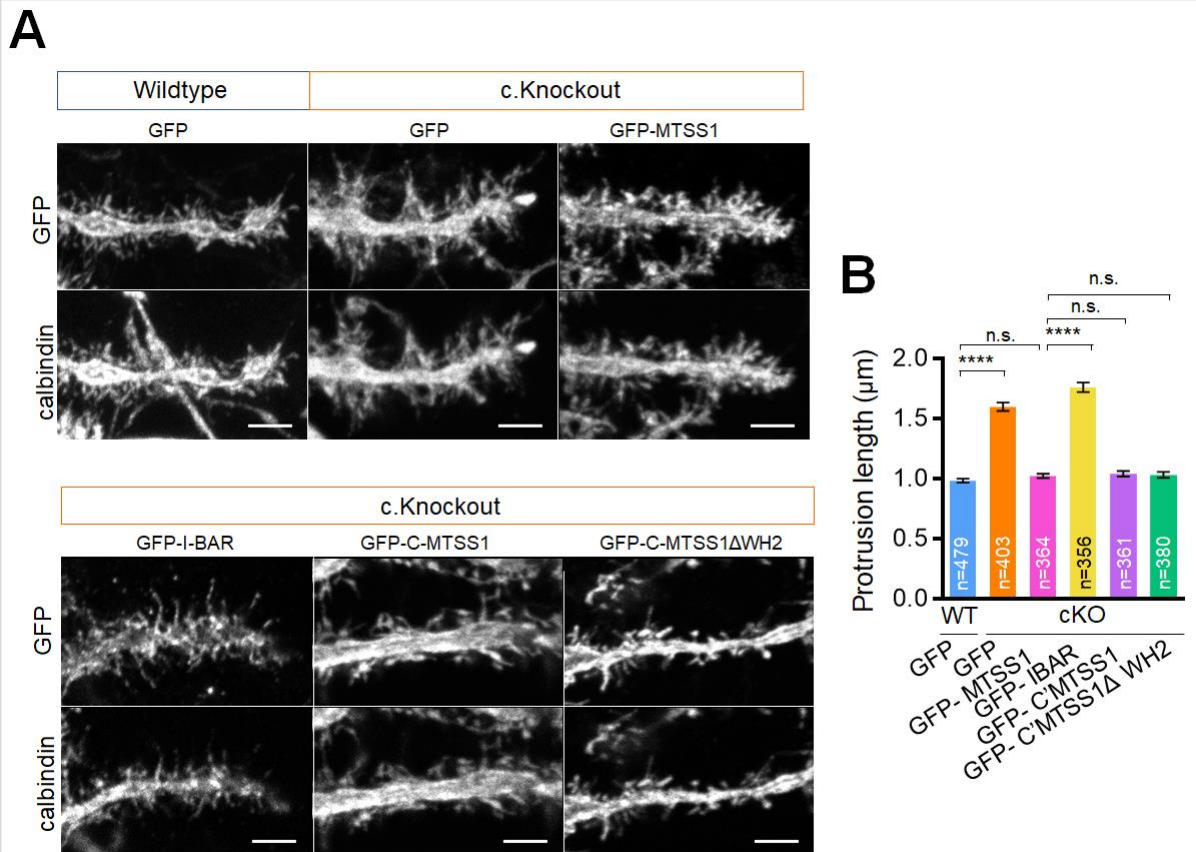


Figure 21. Expression of the SRD-PRD domains of MTSS1 rescues the cKO dendritic protrusion phenotype.

(A) Representative GFP and calbindin images of dendritic segments from 12DIV WT and cKO PCs in dissociated cerebellar cultures, transfected at 0DIV with GFP or GFP-MTSS1 constructs. **(B)** Quantification of dendritic protrusion lengths. Data show mean \pm SEM. Scale bars 3 μ m. **** $p < 0.0001$.

and accumulation at the tips of some protrusions could clearly be seen. Both GFP-C-MTSS1 and GFP-C-MTSS1 Δ WH2 showed diffuse localization throughout the dendritic shaft and protrusions and, consistent with their rescue of the dendritic arbor, resulted in a rescue of dendritic protrusion length (C-MTSS1, $1.04 \pm 0.02 \mu\text{m}$; C-MTSS1 Δ WH2, $1.03 \pm 0.02 \mu\text{m}$). These results indicate that the C-terminal SRD and PRD is critical for MTSS1 regulation of dendritic protrusion and arbor morphology.

1.2 IDENTIFICATION OF MTSS1 DOWNSTREAM PATHWAYS

1.2.1 Upregulation of ARP2/3

MTSS1 function in hippocampal neurons was first reported as a regulator of dendritic protrusion formation, via upregulation of ARP2/3 activation by the accumulation of the I-BAR domain at the membrane (Saarikangas et al., 2015). I first wanted to confirm that this upregulation of the ARP2/3 pathway was also present in Purkinje cells. I transfected wildtype dissociated cerebellar culture with GFP-MTSS1 at 0DIV and observed the morphological phenotype at DIV12. Overexpression of MTSS1 resulted in dendritic protrusions that appeared much more bulbous than dendritic protrusions transfected with only GFP (**Figure 22A**). I observed that overexpression of MTSS1 very slightly reduced the length of dendritic protrusions (WT, $1.02 \pm 0.02 \mu\text{m}$; WT+MTSS1, $0.89 \pm 0.02 \mu\text{m}$), consistent with previous data (Saarikangas et al., 2015). Next, I treated Purkinje cells with the ARP2/3 inhibitor CK-666 (20 μM), which binds at the interface of the Arp2 and Arp3 subunits and stabilizes the inactive state of the ARP2/3 complex (Baggett et al., 2012).

Wildtype cells overexpressing GFP-MTSS1 and treated with CK-666 lost their bulbous morphology and showed rescue back to a dendritic protrusion morphology reminiscent of wildtype cells. On the other hand, treatment of wildtype control cells showed inhibition of ARP2/3 resulted in 57% lengthening of dendritic protrusions (WT+CK-666, $1.61 \pm 0.03 \mu\text{m}$), which was not observed in the cells overexpressing MTSS1 (WT + MTSS1 + CK-666, $1.13 \pm 0.03 \mu\text{m}$) (**Figure 22B**). Lengthening of dendritic protrusions or filopodia after Arp2/3 inhibition has been previously reported (Hotulainen et al., 2009; Kim et al., 2013; Spence et al., 2016), and it has been suggested that when Arp2/3 is inhibited, the formin family of actin binding proteins may

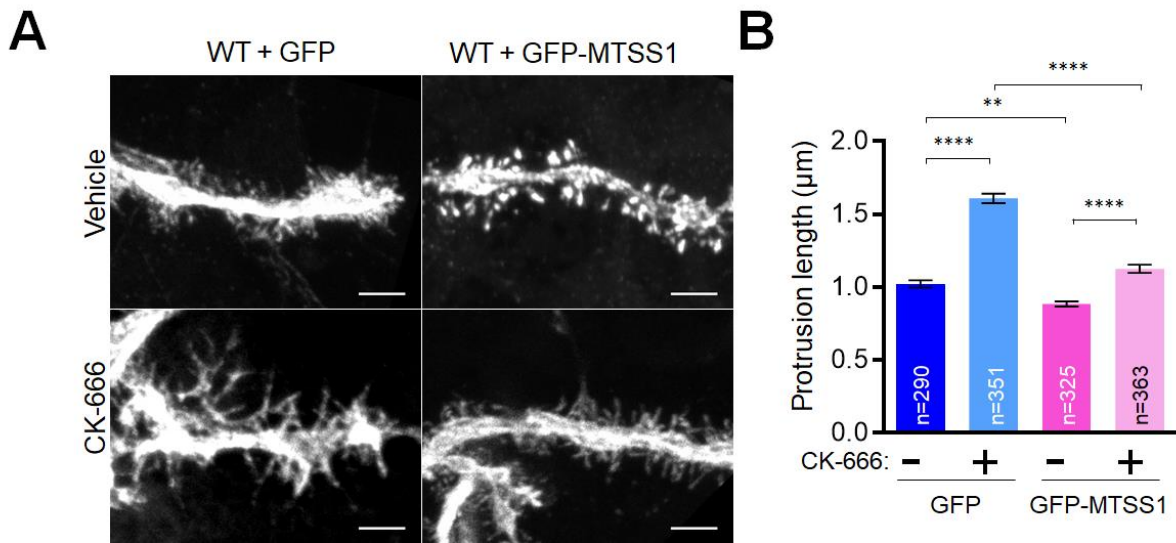


Figure 22. MTSS1 upregulates ARP2/3 activity in PC dendritic protrusions.

(A) Representative images of 12DIV WT PCs transfected at 0DIV with either GFP (left) or GFP-MTSS1 (right) and treated with either vehicle (top) or 20 μm of the ARP2/3 inhibitor CK-666 for 24 hr prior to fixation. **(B)** Quantification of dendritic protrusion lengths in PCs described in (A). Data show mean \pm SEM. Scale bars 3 μm . ** $p < 0.01$, **** $p < 0.0001$.

compensate (Burke et al., 2014; Rotty et al., 2015; Suarez et al., 2015). Thus, I hypothesized that overexpression of MTSS1 may somehow inhibit the compensatory morphological change in CK-666-treated Purkinje cells, possibly upregulating formin activity.

1.2.2 Downregulation of formin

In order to test whether MTSS1 was downregulating formin(s) activity, I acutely treated WT and cKO Purkinje cell cultures with the pan-formin inhibitor SMI-FH2 (10 μ M). I observed that treatment for longer periods of time resulted in poor culture health and retraction of dendrites. I performed live imaging of dendritic protrusions both before and after the addition of SMI-FH2, and observed that within 30 minutes of drug application, wildtype cells showed little change in dendritic protrusion length with formin inhibition. On the other hand, cKO cells treated with SMIFH2, which initially showed long dendritic protrusions prior to drug addition, shortened significantly. To better quantify this, I fixed cultures 10 minutes after drug application, took higher magnification images, and measured the dendritic protrusion lengths (**Figure 23A**). While WT dendritic protrusions only decreased by 19% in length after formin inhibition (WT control, $1.07 \pm 0.02 \mu\text{m}$; WT + SMIFH2, $0.86 \pm 0.02 \mu\text{m}$), cKO cells decreased 33% in length (cKO control, $1.44 \pm 0.02 \mu\text{m}$; cKO + SMI-FH2, $0.97 \pm 0.01 \mu\text{m}$) (**Figure 23B**) supporting the hypothesis that loss of MTSS1 upregulated formin activity.

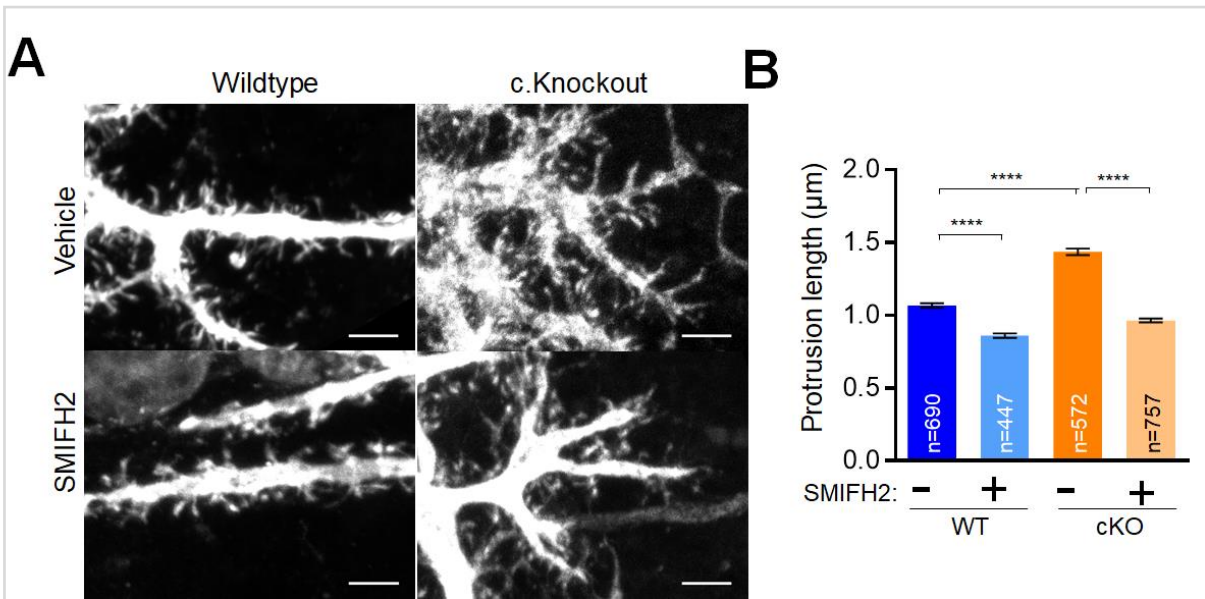


Figure 23. MTSS1 downregulates formin activity in PC dendritic protrusions.

(A) Images of 12DIV WT (left) and cKO (right) PCs transfected at 0DIV with GFP and treated with either vehicle (top) or 10 µm of the formin inhibitor SMI-FH2 for 10 minutes prior to fixation. **(B)** Quantification of dendritic protrusion lengths in PCs described in (A). Data show mean ± SEM. Scale bars 3 µm. **** $p < 0.0001$.

1.2.3 Characterization of DAAM1 in Purkinje cells

Next, I aimed to identify which formin MTSS1 may be negatively regulating in Purkinje cells. A previous study demonstrated that the *Xenopus* MTSS1 interacted directly with the catalytic domain of *Xenopus* DAAM1, a member of the diaphanous-related formin family (Liu et al., 2011). Furthermore, DAAM1 had been shown to be involved in protrusion formation activity (Hoffmann et al., 2014; Jaiswal et al., 2013; Saengsawang et al., 2013; Tsuji et al., 2010).

While a previous study reported that in the adult cerebellum, DAAM1 was most strongly expressed in Purkinje cells (Kida et al., 2004), I first confirmed by western blot that DAAM1 was strongly expressed in the cerebellum throughout development and into adulthood (**Figure 24A**). I followed up by immunofluorescent analysis of cultured Purkinje cells and observed that WT Purkinje cells at 12DIV showed DAAM1 localization throughout the length of the dendritic protrusion, with accumulation at the tip in a subset of more filopodia-like protrusions (**Figure 24B-E**). This localization was consistent with a previous report that DAAM1 was expressed in hippocampal neuronal dendrites (Salomon et al., 2008). Co-labeling MTSS1 showed that many, although not all, of the DAAM1 puncta overlapped with MTSS1 in the dendritic protrusions.

In an attempt to see if upregulation of DAAM1 activity resulted in the lengthening of dendritic protrusions, as seen in cKO Purkinje cells, I cotransfected various amounts of constitutive active DAAM1 into Purkinje cell cultures with a TdTomato transfection marker. Even at low plasmid concentrations, no TdTomato-expressing Purkinje cells could be observed past 3-4DIV, unlike control cultures cotransfected with GFP and TdTomato. This suggested that persistent DAAM1 activity was toxic to Purkinje cells. Because Purkinje cells can only be transfected at 0DIV, I generated an inducible,

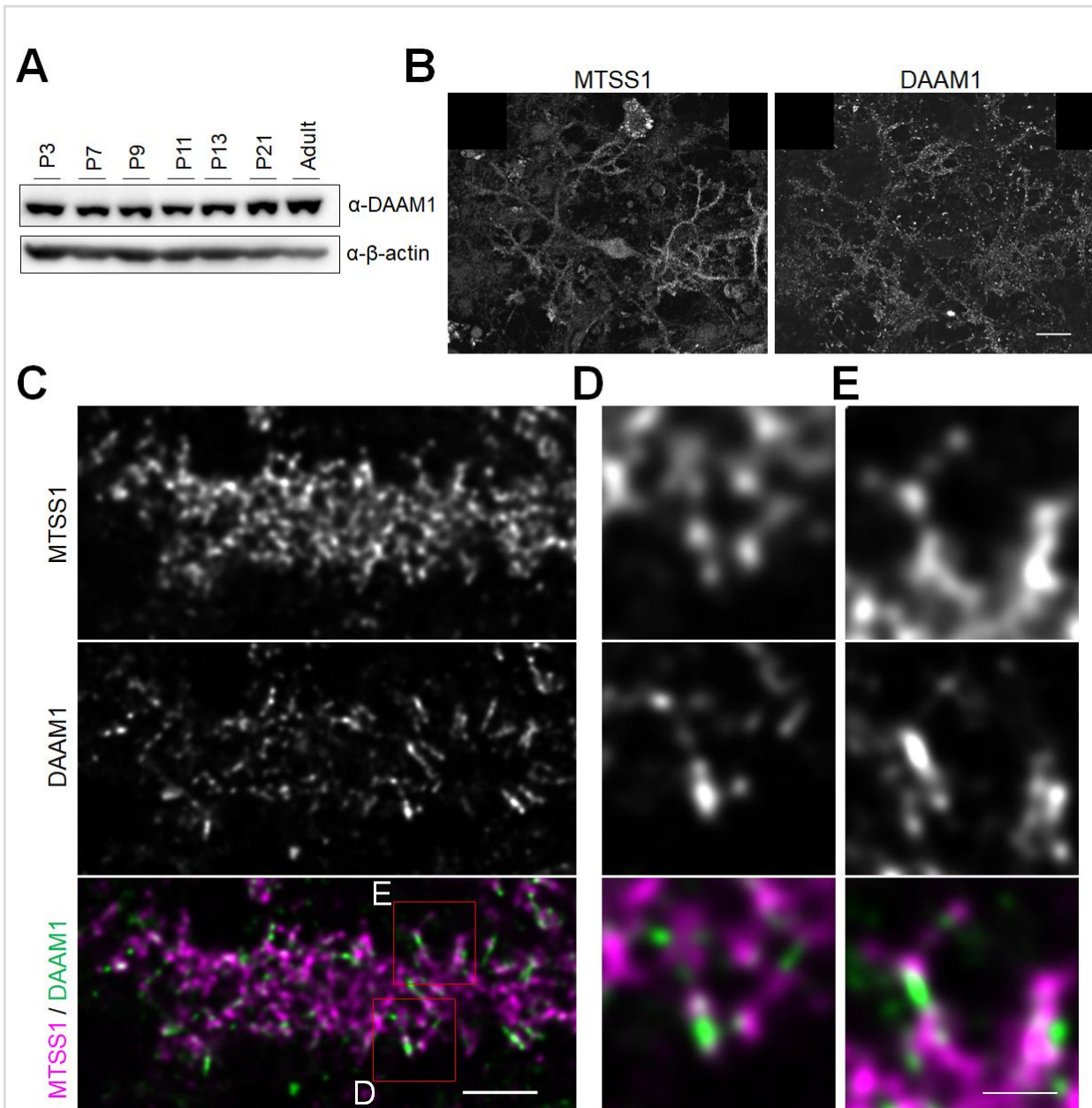


Figure 24. DAAM1 is expressed in the developing cerebellum and is localized in PC dendritic protrusions.

(A) Western blot staining of DAAM1 from cerebellar lysates of WT mice at the indicated ages. **(B-C)** Endogenous staining of MTSS1 and DAAM1 in cultured WT PCs at 12DIV. **(D-E)** Insets shown in (C) demonstrating colocalization of MTSS1 and DAAM1 within a subset of dendritic protrusions Scale bars 20 μm (B), 3 μm (C), and 1 μm (D-E).

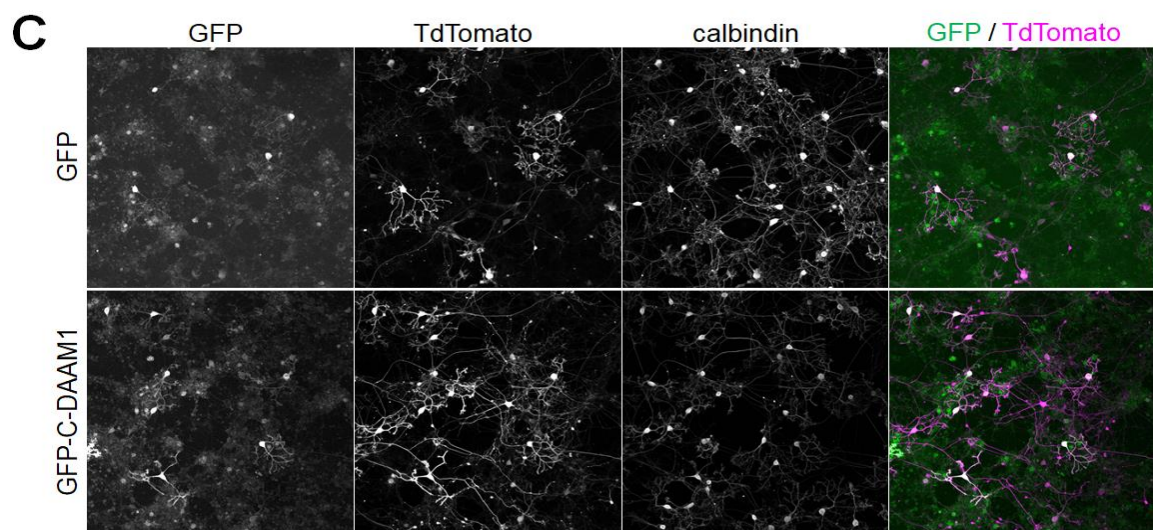
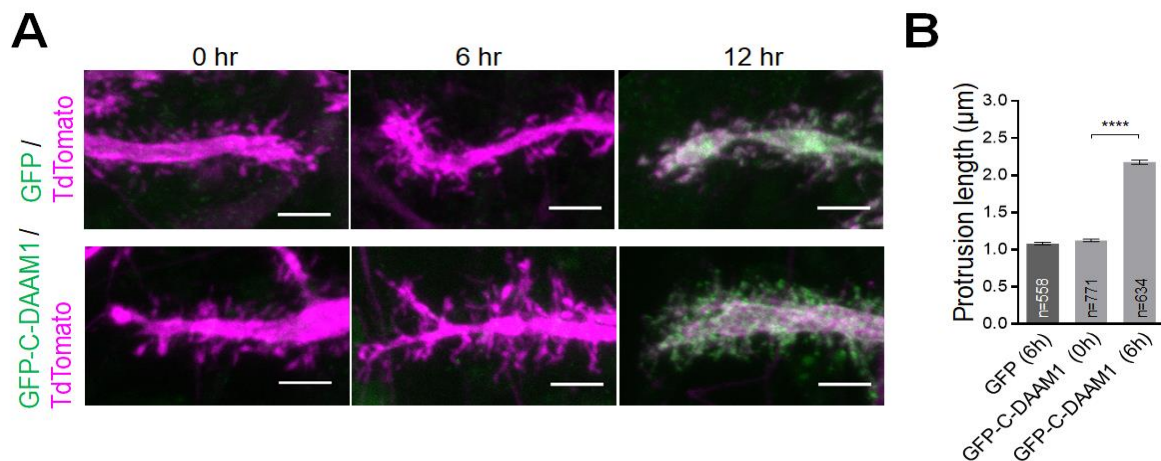


Figure 25. Induction of DAAM1 activity transiently increases dendritic protrusion length.

(A) Dendrite segments from cultured WT PCs transfected with FLE_x-GFP (top) or FLE_x-GFP-C-DAAM1 (bottom) and induced at 12DIV with 500 nM 4-OHT for the indicated times prior to fixation. PCs were transfected at 0DIV with a 1:2:3 ratio mix of CAG::TdTomato, Pcp2(L7):: CreER^{T2}, and CAG::FLE_x-GFP- C-DAAM1. **(B)** Quantification of dendritic protrusions from PCs as described in (A). **(C)** Lower magnification images of cerebellar culture fixed 12 hours after 4-OHT addition, showing TdTomato-positive PCs were also GFP-positive. Data show mean ± SEM. Scale bars 3 μm. **** $p < 0.0001$

constitutive active construct of DAAM1 using the tamoxifen-inducible FLE_x CreER^{T2} system. This allows application of tamoxifen to the culture at the desired time point, leading to translocation of CreER into the nucleus and flipping the coding sequence of constitutive active DAAM1 into the correct orientation for transcription. At 6 hour post tamoxifen addition, the GFP signal was either not visible yet or very weak (**Figure 25A**). However, cells transfected with GFP-C-DAAM1 showed significantly lengthened dendritic protrusions ($2.18 \pm 0.03 \mu\text{m}$), compared with the GFP control ($1.08 \pm 0.02 \mu\text{m}$), as well as compared with Purkinje cells transfected with GFP-C-DAAM1 and treated with vehicle ($1.13 \pm 0.02 \mu\text{m}$) (**Figure 25B**). 12 hours post tamoxifen addition, the GFP signal could be more clearly detected in both conditions, and accumulation of GFP-C-DAAM at the tip of the protrusions could be seen. All Td-Tomato positive Purkinje cells were confirmed to be positive for GFP signal (**Figure 25C**); however, at this time point GFP-C-DAAM expression led to thinning of dendritic protrusions and initiation of quick dendrite retraction, suggesting poor Purkinje cell health. Therefore, it appears that only a small change in DAAM1 activity is sufficient for dendritic protrusion lengthening, and the level of formin activity is very tightly regulated in Purkinje cells.

1.3 REGULATION OF DAAM1 BY MTSS1

1.3.1 MTSS1 DAAM1 interaction

While MTSS1 and DAAM1 were shown to associate with one another in the *Xenopus* system, I next wanted to confirm that the mammalian orthologues showed similar association. I first immunoprecipitated DAAM1 from cerebellar lysate collected from WT mice at P8. MTSS1 could be clearly detected in the immunoprecipitate and not in the control IgG immunoprecipitation (**Figure 26A**).

Next, multiple truncates of GST-MTSS1 fusion proteins were purified and incubated with lysates from HEK293T cells that had been transfected with GFP-C-DAAM1 to identify the binding domains necessary for DAAM1-MTSS1 interaction. While full-length MTSS1 and the C-terminal fragments were able to pull down GFP-C-DAAM1, the I-BAR domain showed no association (**Figure 26B**). These results are consistent with observations from the *Xenopus* orthologs, suggesting conservation of the DAAM1 and MTSS1 interacting residues. Because the C-DAAM truncate includes the FH1-FH2 domain that is highly conserved among many formins, I performed the same pulldown experiment using lysates from HEK293T cells overexpressing the C-terminus of mDia1, and confirmed MTSS1 does not interact with mDia1.

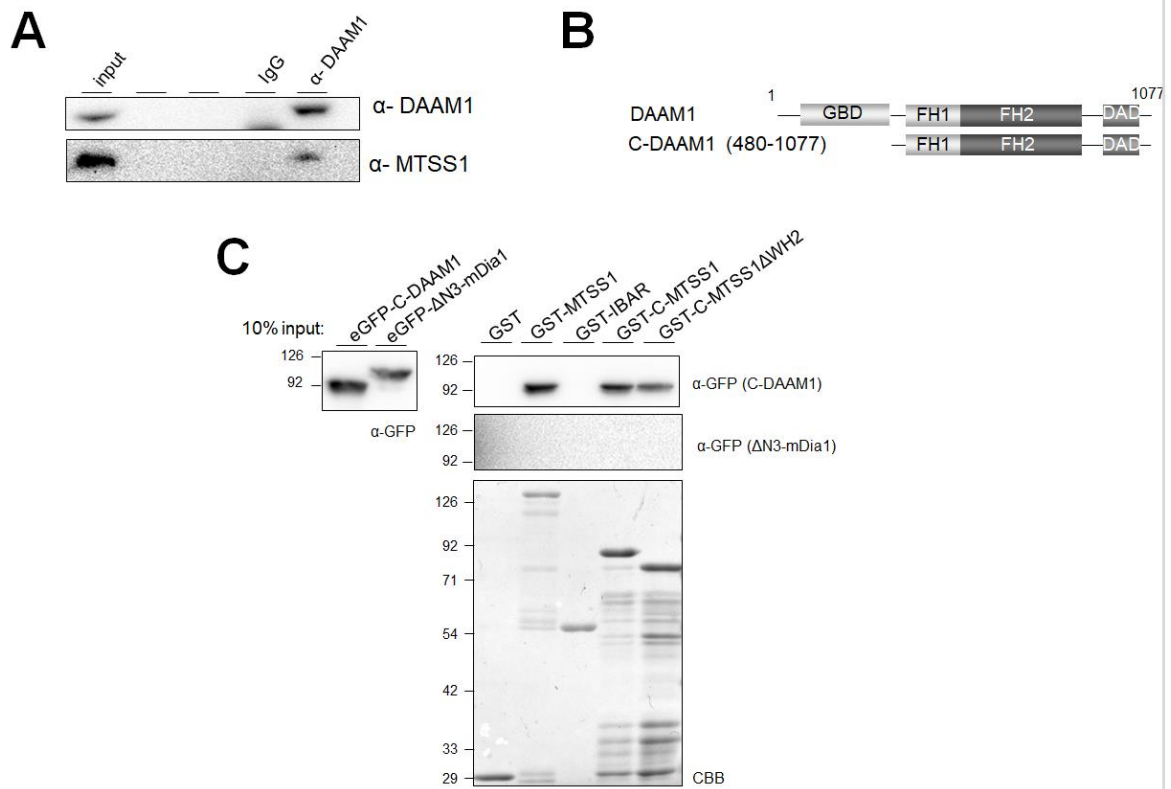


Figure 26. The SRD-PRD region of MTSS1 binds to the C-terminus of DAAM1.

(A) Immunoprecipitation from P8 cerebellar lysate with anti-DAAM1 and IgG as a negative control. **(B)** Schematic of DAAM1 domains and constructs. **(C)** GST pull-down assays using lysates collected from HEK293T cells transfected with GFP-C-DAAM1 and GFP- Δ N3-mDia1 and truncated MTSS1 proteins.

1.3.2 Negative regulation of DAAM1 by MTSS1 in mammalian NIH3T3 cells

Observing changes in endogenous actin levels in Purkinje cells is challenging due to the crowded, multi-layered nature of cerebellar cultures. Thus, to observe how MTSS1 and its specific domains may regulate DAAM1-dependent changes in actin in mammalian cells, I cotransfected constitutive active DAAM1 with MTSS1 truncates in the mouse NIH3T3 cell line. Twenty-four hours after transfection, cells were fixed to observe endogenous F-actin by phalloidin staining. I confirmed previous observations that C-DAAM1 expression significantly increases F-actin assembly (Habas et al., 2001; Higashi et al., 2008) (**Figure 27A-B**). Co-expression of full length MTSS1 and its C-terminus, but not the I-BAR domain, prevented this increase in F-actin formation; however, some cells showed F-actin levels lower than control cells, suggesting that MTSS1 may have multiple mechanisms of regulating F-actin content.

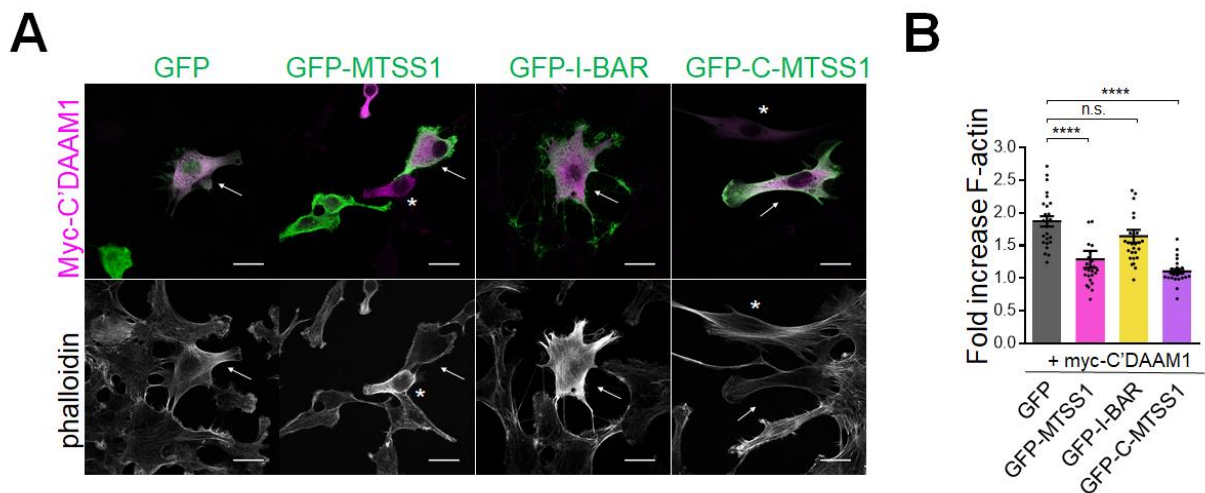


Figure 27. The C-terminus of MTSS1 reduces DAAM1-dependent increase in F-actin content.

(A) NIH3T3 cells transfected with myc-C-DAAM1 and GFP, GFP-MTSS1, GFP-I-BAR, or GFP-C-MTSS1, and stained with anti-myc, anti-GFP, and phalloidin. Arrows indicate co-transfected cells. Asterisks indicate higher relative myc-C-DAAM1 expressing cells. **(B)** Quantification of phalloidin staining intensity in myc- and GFP-double positive cells described in (A) versus non-transfected cells in the same image. $N=25$ for each condition. Data show mean \pm SEM. Scale bars 20 μm . **** $p < 0.0001$

1.3.3 Negative regulation of DAAM1 using SiMS imaging

I next attempted to clarify how MTSS1 was negatively regulating DAAM1 activity. Some formins are known to processively elongate actin, in which a dimerized formin polymerizes F-actin by continuously adding actin monomers to the barbed end (Higashida et al., 2004). Because these formins track the growing barbed end, they can be directly visualized when fused to GFP, using single-molecule speckle microscopy (SiMS) in XTC cells. When plated on glass coverslips coated with polylysine, XTC cells form large, thin lamellipodia that allow observation with minimized obstruction from other planes of focus. Used in combination with transfection of a very low amount of plasmid, individual complexes tagged with a fluorophore can be resolved and directly observed without the need for digital reconstruction such as in PALM or STORM (Higashida et al., 2004, 2008; Ueyama et al., 2016). This method is a more reliable assessment of a formin's F-actin elongation activity in vivo than using biochemical approaches.

I first transfected only GFP-C-DAAM1 to determine whether DAAM1 showed processive elongation. I could observe single speckles, ostensibly dimerized GFP-C-DAAM1, traveling at a consistent velocity on the same vector, confirming that DAAM1 has F-actin processive elongation activity (**Figure 28A-D**). Next, coexpression of C-DAAM with mCherry-MTSS1 resulted in slowed speckle movement. Closer observation showed that some speckles showed occasional pausing during this processive elongation.

To see if this inhibition of DAAM1 activity was specific, I performed the same experiments with constitutive active mDia1, as well as the constitutive active form of the less closely related yeast formin Bni1. Both mDia1 and Bni1 showed processive

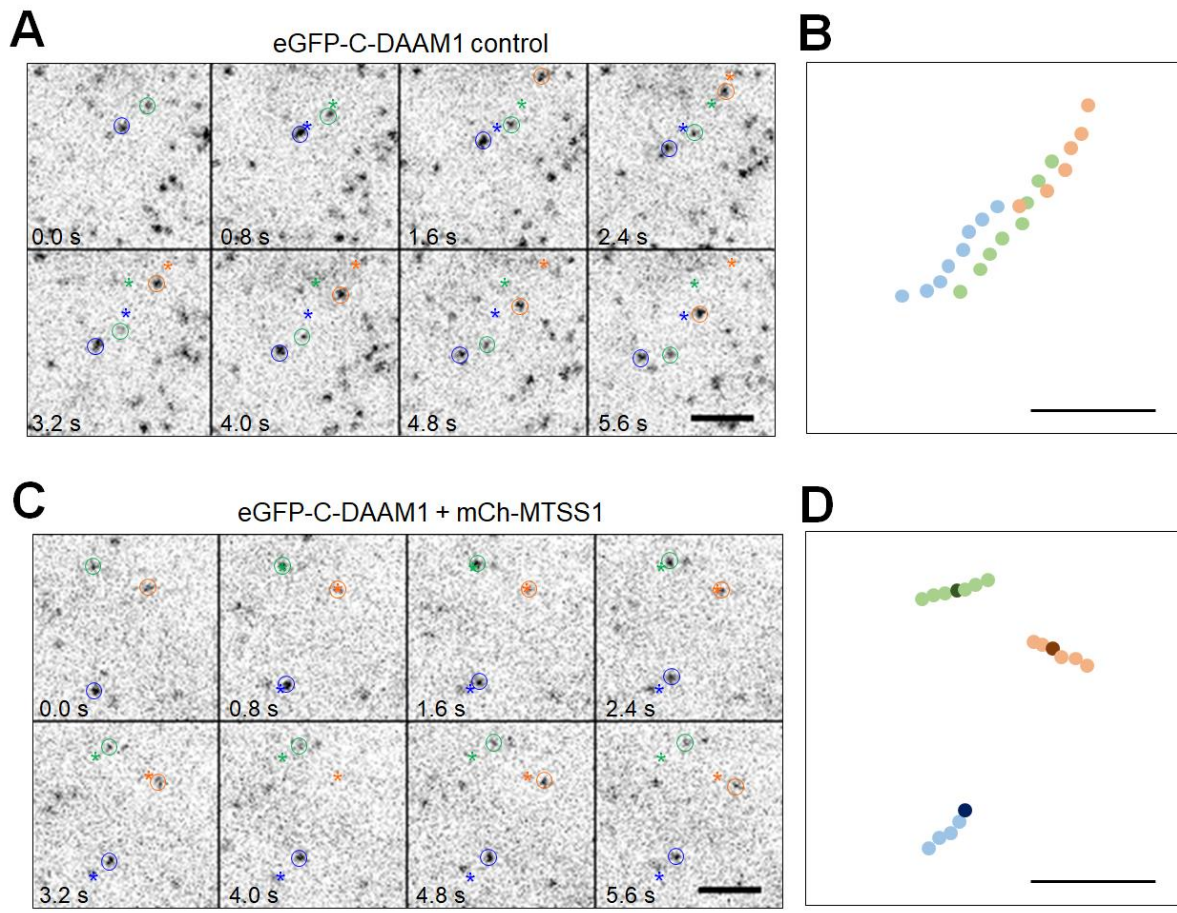


Figure 28. Single-Molecule Speckle (SiMS) imaging of GFP-C-DAAM1 shows slowed movement in the presence of MTSS1.

(A) SiMS imaging showing GFP signal in live XTC cells transfected with GFP-C-DAAM1. **(B)** Speckle position per frame from (A). **(C)** SiMS imaging showing GFP-C-DAAM1 movement in the presence of mCherry-MTSS1. **(D)** Speckle position per frame from images (C) Darker color indicates speckle pause. Scale bars 5 μm .

elongation, and when cotransfected with mCherry-MTSS1, showed slowing of speckle speed, suggesting a slower rate of formin-dependent F-actin elongation. When plotting distance travelled vs time, this becomes more apparent (**Figure 29A-C**). However, the pausing behavior observed with DAAM1 could not be observed for either mDia1 or Bni1 in the presence of MTSS1. This suggested that the interaction between MTSS1 and DAAM1 may underlie the pausing behavior, and the global slowing of all formins may be more of an unspecific effect due to the presence of the WH2 domain at the end of the MTSS1 molecule, which can bind and sequester free G-actin when expressed at very high levels.

To confirm this, I cotransfected the constitutive active formins with C-MTSS1 Δ WH2, and observed that while C-MTSS1 was able to both slow and induce pausing in DAAM1, C-MTSS1 Δ WH2 did not induce global slowing of speckles (MTSS1, $r^2=0.85$, $p<0.0001$; C-MTSS1, $r^2=0.81$, $p<0.0001$; C-MTSS1 Δ WH2, $r=0.32$, $p=0.26$) (**Figure 30A-C**). Similarly, when plotting speckle speed against MTSS1 truncate expression, neither mDia1 or Bni1 showed slopes that were significantly negative in the presence of C-MTSS1 Δ WH2. These data confirmed that overexpression of the WH2 domain seems to sequester free G-actin. Of interest, it appeared that, although not significant, expression of C-MTSS1 Δ WH2 showed a tendency to decrease DAAM1 speed. This may be due to the inclusion of tiny pauses that were unable to be resolved at the time scale of imaging.

Next, I quantified the proportion of measured speckles in each cell that showed pauses longer than 1s, requiring that they recovered movement on the same vector within the observation timeframe. Because this does not include speckles that were either already paused when imaging was started, or stopped and did not recover

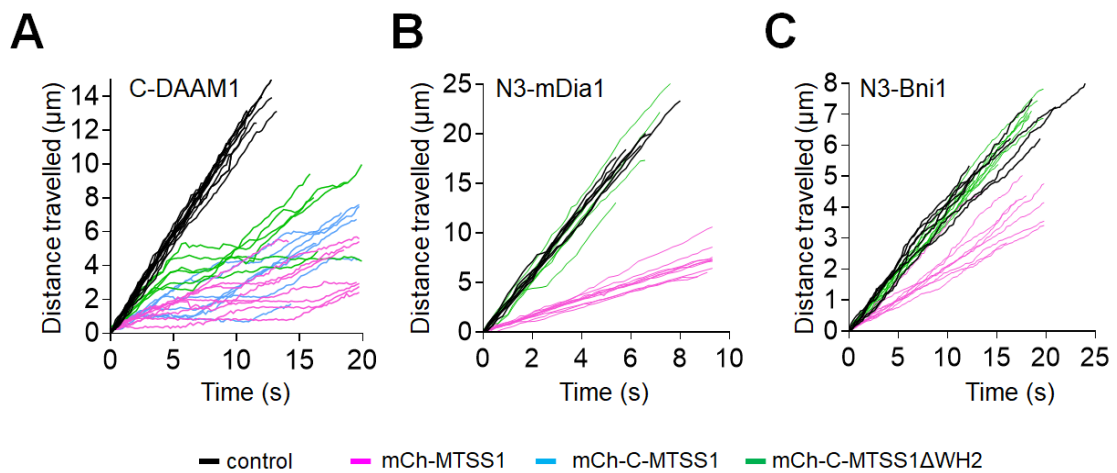


Figure 29. MTSS1 non-specifically slows processive elongation of formins, but induces pauses specifically for DAAM1.

(A-C) Distance vs time plots of individual GFP-tagged constitutive active (A) DAAM1, (B) mDia1, and (C) Bni1 in the presence of MTSS1 or its truncates visualized by SIMS.

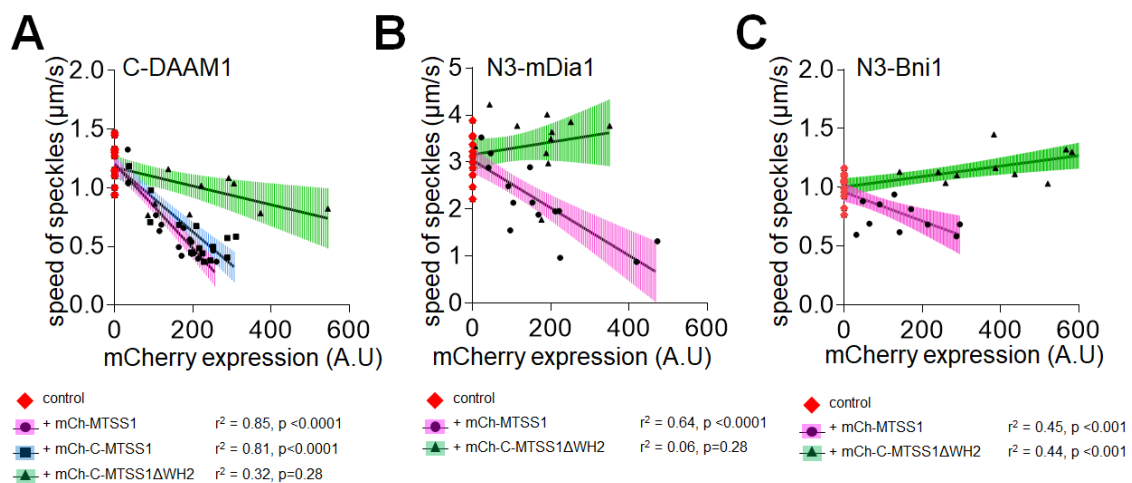


Figure 30. MTSS1 non-specifically decreases formin elongation speed due to presence of the WH2 domain.

(A-C) Speed of speckles were calculated from the slope of distance vs time plots at regions where speckles were not paused. GFP-tagged constitutive active (A) DAAM1, (B) mDia1, and (C) Bni1 all showed slowed speed in the presence of MTSS1 in an expression-level dependent manner. This decrease in speed was abrogated with truncation of the WH2 domain.

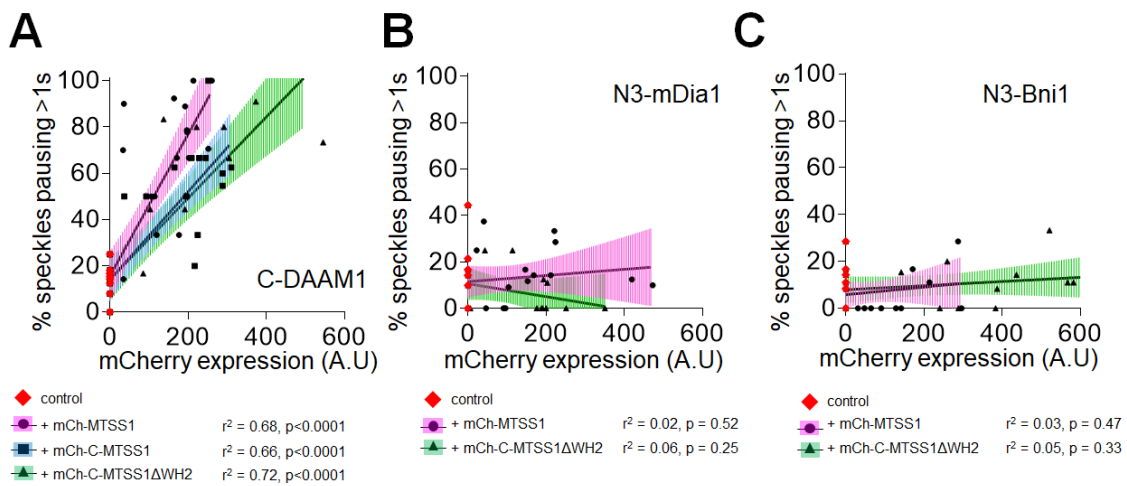


Figure 31. The SRD-PRD region of MTSS1 specifically induces DAAM1 pausing.

(A-C) Speckle pausing was measured from distance vs time plots. **(A)** MTSS1 and its truncates were all able to induce similar extent of DAAM1 pausing in an expression-dependent manner. **(B)** mDia1 and **(C)** Bni1 did not show any pausing.

movement within imaging, this measurement underestimates the proportion of pausing speckles.

Control cells had an average of $9.7\% \pm 8.8\%$ (mean \pm SD) GFP-C-DAAM1 speckles showing a pause of >1 s (**Figure 31**). However, in the presence of MTSS1, there was a significant positive correlation between DAAM1 pausing and MTSS1 expression level ($r^2=0.68, p<0.0001$) as well as in the presence of C-MTSS1 ($r^2=0.66, p<0.0001$). This pausing behavior was still observed in with the loss of the WH2 domain ($r^2=0.72, p<0.0001$). Neither mDia1 nor Bni1 showed any increase in pausing, even with high levels of MTSS1 expression.

1.3.4 Biochemical analysis of MTSS1 inhibition of DAAM1.

While use of SiMS imaging and XTC cells allowed a more natural environment to study the activities of DAAM1 and MTSS1, it was still unknown whether MTSS1-dependent induction of DAAM1 polymerization pausing was due to direct binding or required additional factors found in the cell environment. In an attempt to assess this, I performed TIRF imaging using purified constitutive active C-DAAM1 as well as C-MTSS1 Δ WH2, to directly visualize elongating F-actin filaments.

Initial attempts to visualize DAAM1-dependent F-actin elongation proved to be very challenging, due to the similar apparent elongation speeds of DAAM1-dependent and spontaneous F-actin elongation, and the difficulty in distinguishing between the two. This is consistent with a recent report demonstrating the inability of the drosophila orthologue DAAM to increase elongation speed of F-actin (Vig et al., 2017). Therefore, I next immobilized GST-C-DAAM1 by incubating the purified protein with polystyrene beads functionalized with anti-GST IgG to try to differentiate between DAAM1-dependent and spontaneous elongation of F-actin (**Figure 32A**).

C-DAAM1-functionalized beads were adhered to glass in a flow chamber, followed by a subsequent series of washes, nucleation, and elongation buffers. Actin was initially nucleated without the presence of Profilin for 1 minute to minimize the possibility of Profilin-dependent inhibition of this step. This was then followed by an elongation buffer which included labelled actin, Profilin, and in some cases, purified GST-C-DAAM1. Using 10% labelled G-actin, which forms F-actin with light and dark patches, DAAM1-dependent elongation of F-actin could be identified by movement of F-actin away from the bead, due to immobilized DAAM1-dependent barbed-end addition of actin monomers (**Figure 32B**). Interestingly, I could observe the sides and pointed end of F-actin often attaching to the bead. While it has been reported that

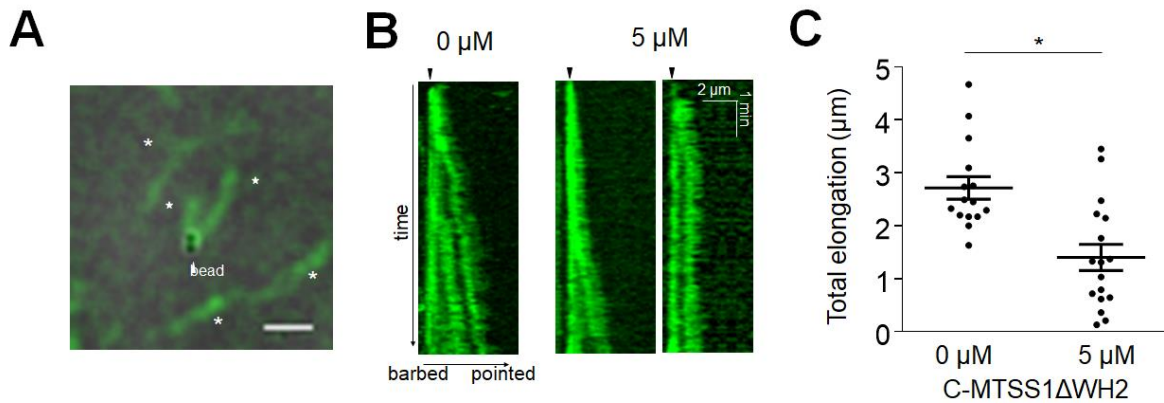


Figure 32.

(A) Example of TIRFM F-actin fluorescence image merged with phase-contrast image of GST-C-DAAM1-beads. Stars indicate C-DAAM1-dependent processively elongating F-actin in the presence of 0.5 μM G-actin and 2 μM profilin. G-actin is preferentially incorporated at the barbed end (bead-side), and the pointed end is pushed away from the bead. Asterisks indicate spontaneously formed F-actin. Scale bar 3 μm. **(B)** Kymographs of processively elongating F-actin in the absence (left) and presence (right) of 5 μM C-MTSS1ΔWH2. Arrowhead indicates position of GST-C-DAAM1 bead. **(C)** Quantification of the length of elongation during 250 s of observation, including F-actin that stopped growing. Student's t-test. Data show mean ±SEM. * $p < 0.05$

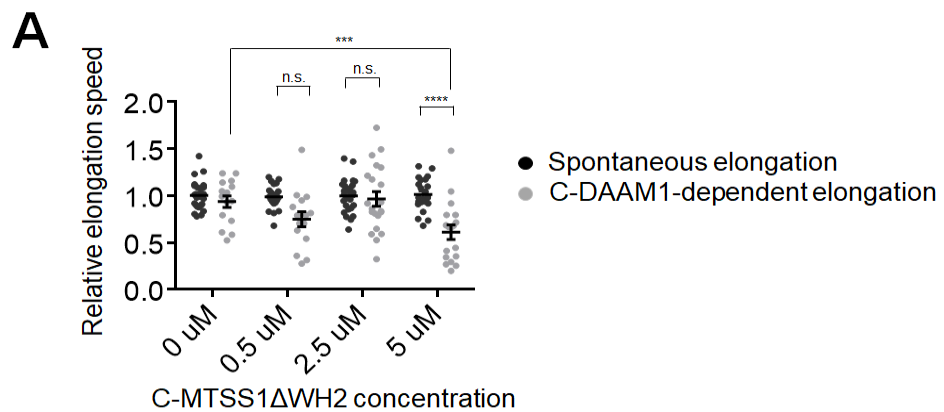


Figure 33. Relative speeds of C-DAAM1 dependent F-actin elongation.

(A) The speed of each F-actin showing C-DAAM1-dependent elongation was normalized to the average elongation speed of spontaneously formed F-actin in each field of view. Data show mean ±SEM. N=15-26 filaments per condition, pooled from three replicate experiments. *** $p < 0.001$, **** $p < 0.0001$, two-way ANOVA.

DAAM1 can function as an F-actin bundler (Jaiswal et al., 2013), there have been no reports of DAAM1 binding to the pointed end of F-actin. Unfortunately, I did not perform control experiments with GST-immobilized beads to determine whether this binding was DAAM1-specific or not.

In the presence of C-MTSS1 Δ WH2, several observations were made. First was what appeared to be a subset of filaments that stopped their elongation (**Figure 32B**), but were quickly obscured by other spontaneously growing F-actin. When including these filaments in measurements of elongation speed, it could be seen that total elongation of the F-actin was reduced in the presence of C-MTSS1 Δ WH2 (**Figure 32C**). However, these filaments were observed in the same field of other active C-DAAM1-dependent elongation, making it unclear what the difference between these two populations of filaments were. Measurement of relative elongation speed, that is, the speed of C-DAAM1-dependent filament elongation normalized to the elongation rate of spontaneously formed filaments in each field of view, C-DAAM1-dependent filaments showed a slight decrease in speed in the presence of C-MTSS1 Δ WH2 (**Figure 33A**).

CHAPTER 3. DISCUSSION

3.1 Discussion

The phenotypic differences observed among the different MTSS1 knockout models highlighted the need for further clarification of the cell-specific function of MTSS1 in different neurons (Saarikangas et al., 2015; Sistig et al., 2017). In particular, it is difficult to interpret the morphological defects observed in the cerebellum in global knockout models due to MTSS1 expression in granule cells, which provide synaptic input onto Purkinje cells (Holst et al., 2008; Hayn-Leichsenring et al., 2011). MTSS1 deficiency in granule cells might affect circuit formation or function, thus resulting in a more severe effect on Purkinje cells in global knockout mice. Although in the Kansas City model, selective re-expression of MTSS1 in the granule cells demonstrated persistent defects in Purkinje cell dendritic morphology, re-expression of MTSS1 in the Purkinje cells showed that the loss of granule cell MTSS1 still resulted in Purkinje cell dendritic morphology defects. While proper innervation is not necessary for Purkinje cell spine initiation (Hirano et al., 1977), we cannot rule out the possibility that proper innervation is required for correct attainment of morphological structure. Therefore, in this study we used a Purkinje cell-specific knockout mouse to better clarify the cell autonomous role of MTSS1.

It has been proposed that dendritic filopodia around the growing tips of Purkinje cell dendrites (terminal filopodia) function as environmental sensors and regulate dendritic growth and branching (Berry and Bradley, 1976). Furthermore, it has been shown that dendritic filopodia act as mediators of contact-dependent retraction, which ensures the non-overlapping arrangement of Purkinje cell dendrites (Fujishima et al., 2012). Their extremely high density in developing Purkinje cells suggests the possibility that they may function to extend the diameter of dendritic reach without

compromising dendritic volume (Ziv and Smith, 1996). Our initial hypothesis was that, due to the ability of MTSS1 to make membrane protrusions, knockout would result in a loss of dendritic protrusions, and following that, loss of dendrites. While my observations showed a decrease in both total dendritic length and branching points, the changes were much milder than what would be expected if dendritic initiation was somehow hampered. Furthermore, the biased difference in dendrite complexity, comprising the loss of dendrites proximal to the soma and somewhat increased density further from the soma, suggested that there was no change in the ability of a dendrite to form, rather that there was a defect in the space-filling arborization rules that govern dendritic growth. This was confirmed by live imaging that suggested oversensitivity of the intrinsic dendritic self-avoidance behavior in Purkinje cells after MTSS1 loss.

What was most unexpected was my observation of a significant increase in dendritic protrusion length and no change in protrusion density. This was opposite of our initial hypothesis, as well as inconsistent with the 2015 Saarikangas et al. report published during my work on this project. This clear lack of necessity of the MTSS1 I-BAR domain demonstrated that MTSS1's regulation of the actin cytoskeleton via its other domains played a more important role in dendritic protrusion development. I believe this may have been overlooked in the 2015 study due to the use of the Finnish knockout model, which may possibly express a C-terminal truncate of MTSS1 in hippocampal neurons. This inconsistency regarding the need of the I-BAR domain was also noted in the 2015 paper; the authors reported that despite MTSS1 I-BAR loss, a complete inability to initiate protrusions was not observed as their model suggested, possibly due to the redundant behavior of other I-BAR or F-BAR proteins.

While several cell-surface molecules have been identified in dendritic self-avoidance of space-filling neurons, it remains unclear how the signaling threshold for retraction is established and regulated. My results suggest that contact-dependent retraction is dependent on both the surface molecule expression and the physical morphology and dynamics of dendritic protrusions. Given the discrepancy between the high density of dendritic protrusions and the delay observed in dendritic retraction, it is unlikely that a single contact results in dendrite retraction. Rather, it is more likely that a number of contacts must occur before rising above the threshold required for generating a retraction signal. However, it is still unknown what regulatory mechanisms underlie the frequent extension and retraction we can observe in wildtype Purkinje cell dendritic protrusions.

Later observation of Purkinje cell dendritic protrusions showed that loss of MTSS1 did not appear to affect differentiation of filopodia into spines but rather caused elongation of all protrusions. This all-encompassing change in protrusion morphology is not surprising, as dendritic filopodia and spines share common molecular characteristics and lie on a reversible morphological spectrum: (1) unlike canonical filopodia, dendritic filopodia show unbundled, bidirectional orientation of individual F-actin filaments similar to what is found in thin spines and the spine neck (Korobova and Svitkina, 2010); (2) dendritic protrusions morphologies are not static, and have been observed to show reversible morphological changes (Halpain et al., 1998; Nägerl et al., 2004; Schätzle et al., 2011); and (3) both structures contain the same actin-binding proteins that generally produce differing physical structures. Thus, MTSS1 may function as one regulator of the balance of these actin-binding proteins in dendritic protrusion morphogenesis.

Due to their small volume, dendritic protrusions require tight regulation and balance of actin nucleation to orchestrate the fast, reversible morphological changes that have been observed during live imaging. This is supported by observations that the ARP2/3 and formin-mediated pathways of actin nucleation can compete for G-actin within cells (Burke et al., 2014; Rotty et al., 2015; Suarez et al., 2015), which has also recently been shown to occur within the spine head (Glebov and Burrone, 2016); thus, disruption of one pathway can indirectly affect another. In Purkinje cells, overexpression of MTSS1 in a WT background resulted in bulbous protrusions, which was lost by ARP2/3 inhibition, confirming that the MTSS1-ARP2/3 axis of regulation is also present in Purkinje cells. MTSS1 has been identified to indirectly upregulate the ARP2/3 pathway via two methods: (1) accumulation of PI(4,5)P₂ in the plasma membrane via its I-BAR domain, which in turn recruits ARP2/3-activating factors during initiation of dendritic protrusions (Maddugoda et al., 2011; Saarikangas et al., 2015), and (2) by direct interaction via its PRD with cortactin and facilitation of cortactin's upregulation of ARP2/3 activity (Lin et al., 2005). The morphology of Purkinje cell dendritic protrusions appears solely dependent on the latter mechanism, as the C-terminus of MTSS1 lacking the I-BAR domain was sufficient for function of the full-length MTSS1 in this context.

The increased protrusion length in MTSS1-deficient cells I observed suggested either the loss of MTSS1-mediated ARP2/3 activation, which induces compensatory formin activation, and/or the loss of MTSS1-directed formin suppression. This led us to wonder to what extent MTSS1 may regulate other actin nucleators other than the previously reported ARP2/3. My results indicate a novel function of MTSS1 as a direct inhibitor of DAAM1, thus providing support for the latter scenario and suggesting MTSS1 plays a dual role as ARP2/3 activator and formin inhibitor in dendritic

protrusions. Taken together, it is likely that MTSS1 has dual functions during dendritic protrusion formation: the first initiation step, in which the MTSS1 I-BAR domain contributes to membrane bending and ARP2/3 recruitment, and the growth step, based on a balance of DAAM1-inhibition and possibly ARP2/3-activation by the C-terminal domain.

My results demonstrated that endogenous DAAM1 is highly localized to the tips of dendritic protrusions in Purkinje cells, and that acute over-activation of DAAM1 leads to transient increase in dendritic protrusion length. This is in line with previous results showing that expression of a constitutive-active form of mDia2 results in an increase in filopodia length (Hotulainen et al., 2009). Experimental and computer modeling have shown that dendritic protrusion dynamics and final morphology are most dependent on the rate of actin polymerization (Marchenko et al., 2017; Miermans et al., 2017), suggesting the contribution of a concerted effort of local formin activation and release of inhibition.

I confirmed that mammalian MTSS1 specifically binds to DAAM1 and homeostatically inhibits DAAM1 actin polymerizing activity in Purkinje cell dendritic protrusions. Like many other formins, DAAM1 contains a G-actin-binding WH2-like domain in the C-terminus that overlaps with the diaphanous autoinhibitory domain (DAD)(Gould et al., 2011; Vig et al., 2017). Formin activity is tightly regulated by the autoinhibitory interactions of DAD with the N-terminal diaphanous inhibitory domain (DID), which can be released by members of the Rho family of GTPases (Higashi et al., 2008), Wnt-dependent binding to Disheveled (Habas et al., 2001; Liu et al., 2008), and a yet uncharacterized conformation change of the FH2 domain to allow exposure of its actin-binding surfaces (Lu et al., 2007). While I did not assess if MTSS1 inhibits

DAAM1 activation, I demonstrated that MTSS1 clearly binds to the constitutive active form of DAAM1 and inhibits actin polymerization via two mechanisms. First, overexpression of MTSS1 can non-specifically slow actin polymerization by DAAM1 and other formins via WH2-dependent competition for free G-actin. This may be specifically enhanced for DAAM1 at physiological MTSS1 concentration due to the direct binding of MTSS1 and increased proximity of its WH2 domain. Second, MTSS1 can specifically induce pauses of DAAM1 during polymerization independently of the MTSS1 WH2 domain.

Due to the strong polymerizing activity of formins once activated, there likely exists multiple levels of their regulation within the dendritic protrusion. My data suggests that MTSS1 can inhibit DAAM1 activity. However, assessment of whether MTSS1 can directly inhibit DAAM1-dependent F-actin elongation without the need of other cofactors remains ambiguous, and requires further analysis. Therefore, it is unknown whether C-MTSS1 Δ WH2 induces transient disassociation of the DAAM1 dimer from the F-actin, blocks G-actin addition, or prevents the sliding of the DAAM1 dimer to remain at the barbed end. Observation in mammalian cells also suggests other pathways of regulation may be involved. The decrease in protrusion length observed after treatment of WT cells with the pan-formin inhibitor SMI-FH2 suggest a basal activity of other formins and/or only a partial inhibition of DAAM1 by endogenous MTSS1. In addition to DAAM1, mDia2 and Delphilin have also been shown to be localized to neuronal protrusions, and mDia2 has been shown to regulate dendritic protrusion morphology (Dutta and Maiti, 2015; Hotulainen et al., 2009; Miyagi et al., 2002; Takeuchi et al., 2008).

In conclusion, I have shown that MTSS1 modulation of opposing actin nucleation pathways is important for both macro- and microscale morphogenesis of neuronal dendrites (**Figure 34**). Much remains to be clarified of the regulatory interplay and control of the fine actin-based temporal dynamics, which is made especially challenging due to the functional redundancy and mutual competition/compensation of actin binding proteins.

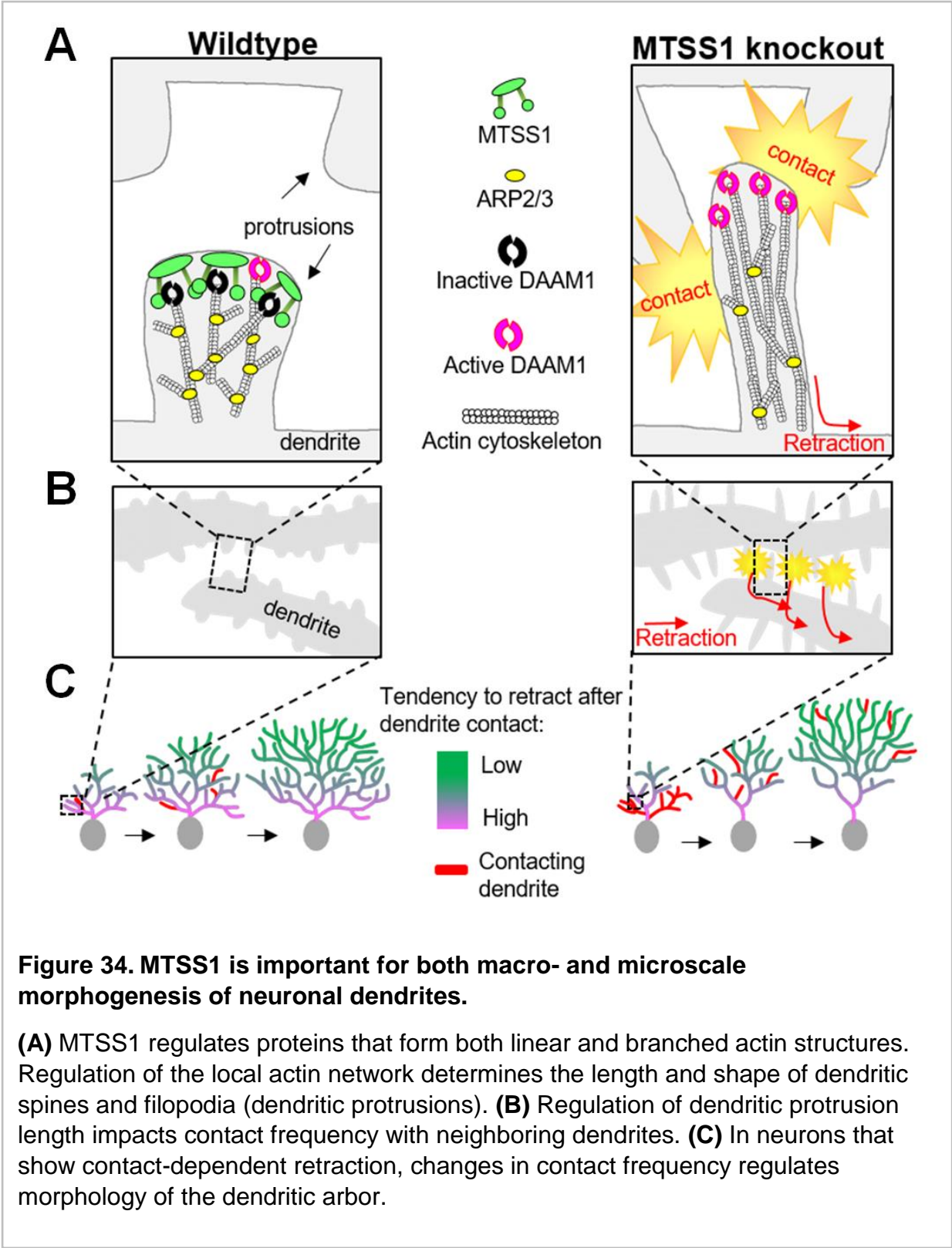


Figure 34. MTSS1 is important for both macro- and microscale morphogenesis of neuronal dendrites.

(A) MTSS1 regulates proteins that form both linear and branched actin structures. Regulation of the local actin network determines the length and shape of dendritic spines and filopodia (dendritic protrusions). **(B)** Regulation of dendritic protrusion length impacts contact frequency with neighboring dendrites. **(C)** In neurons that show contact-dependent retraction, changes in contact frequency regulates morphology of the dendritic arbor.

3.2 Limitations of this study

The GluR δ 2 promoter has been previously used as a Purkinje cell-specific promoter which begins expression around embryonic day 15 (Takayama et al., 1996). However, recent studies have indicated that this promoter drives expression in GABAergic basket and stellate interneurons of the cerebellum, albeit at a later stage, around postnatal day 14 (Hashimoto et al., 2011; Yamasaki et al., 2011). Despite this, there have been no reports of MTSS1 expression in cerebellar interneurons, so we have continued calling these mice Purkinje cell-specific knockout.

Our knockout model utilizes floxing of the fourth exon to mediate Cre-dependent recombination and generation of a stop codon for subsequent knockout. This strategy has the benefit of avoiding the alternative promoter found in exon three which may, in some cells, lead to transcription of a truncated MTSS1 lacking the first part of the I-BAR domain. In our model, possible expression of exons 1-3 may occur, resulting in expression of a 69-residue sequence that retains the domain necessary for homodimerization. However, the membrane-binding region of the I-BAR domain has been reported to occur between residues 129-150 (Mattila et al., 2007). Thus, it is unlikely that this truncate is functional.

CHAPTER 4. MATERIALS AND METHODS

4.1 ANIMALS

Details of *Mtss1^{flox/flox}* generation can be found in (2018) Kawabata Galbraith et al. Littermates from *Mtss1^{flox/flox}* and *Mtss1^{flox/flox-/-}*; *GluRδ2-Cre^{+/-Cre}* crossings were genotyped for presence or lack of *GluRδ2-Cre* either on P0 for use in cerebellar cultures, or on P7 for use in immunohistochemistry experiments. Both male and female pups were pooled and used for experiments with no distinctions made between the two.

Mice were treated according to the Animal Experiment Committee guidelines of Kyoto University. Mice were provided with standard food and water *ad libitum*, and kept in a 12 hr dark/light cycle at 23±3°C/50% humidity. Mice were kept in group housing of up to three animals per cage. *MTSS1* conditional knockout mice were housed in standard SPF conditions. Wildtype ICR mice (Japan-SLC, Cat# Slc:ICR) were obtained 1-3 days prior to giving birth and kept in a conventional animal facility, and used in experiments requiring only mice with wildtype backgrounds.

4.2 PRIMARY CELL CULTURE

To generate primary cerebellar dissociated cultures, I dissected cerebella from littermates of *Mtss1^{flox/flox}* and *Mtss1^{flox/flox-/-}*; *GluRδ2-Cre^{+/-Cre}* crossings the day of birth. After removing the meninges, cerebella were pooled and washed briefly in HBSS (Gibco), and dissociated using the Neuron Dissociation Kit (Wako Pure Chemical Industries, Ltd). Cells were resuspended in DMEM/F12 (Gibco) supplemented by 10% FBS (Gibco) at a concentration of 2 cerebella/coverslip to keep the extremely high density required for Purkinje cell survival. Cells were plated on 12 mm glass coverslips that had been extensively washed with 95% ethanol and coated with 400 µg/mL poly-D-lysine (Sigma-Aldrich) overnight, followed by incubation for 2-3 hrs at 37°C/5%CO₂. Following incubation, I exchanged the medium to one containing DMEM/F12 supplemented with 0.1 mg/ml bovine serum albumin (Sigma-Aldrich), 2.1 mg/ml glucose (Sigma-Aldrich), 2x GlutaMAX™ (Gibco), 8 µM progesterone (Sigma-Aldrich), 20 µg/mL insulin (Sigma-Aldrich), 200 µg/mL transferrin (Sigma-Aldrich), 100 µM putresine (Sigma-Aldrich), 30 nM selenium dioxide (Sigma-Aldrich), 5 µM Ara-C (Sigma-Aldrich), 100 units/mL penicillin (Gibco), and 100 µg/mL streptomycin (Gibco).

The cultures were maintained at 37°C/5%CO₂, with a 50% media exchange every 5-7 days.

4.3 CELL LINE CULTURES

HEK293T (Riken BRC Cell Bank, RCB2202) and NIH3T3 (Riken BRC Cell Bank, RCB1862) cells were cultured in DMEM (Gibco) supplemented with 10% Fetal Bovine Serum (FBS), 100 units/mL penicillin, and 100 ug/mL streptomycin. HEK293T cells were passaged at a 1:5 split every 2-3 days, and NIH3T3 cells were consistently passaged every 3 days and plated at a density of 1.5x10⁴ cells/cm². The cultures were maintained in plastic cell culture-treated dishes, or were plated for experiments on glass coverslips (Matusnami Glass IND., LTD, C012001) coated with 100 ug/mL poly-D-lysine, and maintained at 37°C/5% CO₂ and

XTC cells were cultured in 70% Leibovitz's L15 medium (Gibco) supplemented with 10% FCS (Gibco) and were maintained at 25°C. Cells were passaged every 2-3 days at a 1:5 split, and maintained in plastic cell culture-treated dishes. For experiments, cells were plated on glass coverslips coated with 100 ug/mL poly-L-lysine, in 70% Leibovitz's L15 medium with no serum or phenol red.

4.4 PLASMIDS AND CONSTRUCTION

The plasmids pAAV-CAG-eGFP, pAAV-CAG-mCherry, pAAV-CAG-TdTomato, and pCMV-ΔN3-mDia1 have been previously described (Fujishima et al., 2012; Higashida et al., 2004). The plasmids pCAGGS-Flex and pCL20c-L7::ERT2-Cre-ERT2 were kindly provided by Michisuke Yuzaki of Keio University, Japan. pGEX-4T-3 (GE Healthcare), pCMV-tag5a (Agilent) were purchased.

The full coding sequence of MTSS1 (Forward: ACACGGATCCATGGAGGCTGTGATCGAGAAGGAAT, Reverse: ACACGCGGCCGCCTAAGAGAAGCGCGGTGCTGAGC) and the C-DAAM1 fragment (Forward: ACACGGATCCAAGGAAGAAATGATGCAGACCTTAA, Reverse: ACGCGGCCGCCTATTAATAAATTAAGTTTTGTGATT) were PCR-amplified from P1 mouse cerebellum cDNA and cloned into the BamHI and NotI sites of pCAGGS-GFP-MCS for CAG promoter-driven N'-tagged eGFP expression constructs. Other eGFP-tagged MTSS1 truncates were PCR amplified from pCAGGS-GFP-MTSS1 and cloned

into the BamHI and NotI sites of pCAGGS-GFP-MCS using the following primers: I-BAR (Forward: ACACGGATCCATGGAGGCTGTGATCGAGAAGGAAT; Reverse: ACGCGGCCGCCTAAGAACCTTTCAAGTCCAAAATC), C-MTSS1 (Forward: ACACGGATCCAAGGACTGGGCAAAGCCAGGA; Reverse: ACACGCGGCCGCCTAAGAGAAGCGCGGTGCTGAGC), C-MTSS1 Δ WH2 (Forward: ACACGGATCCAAGGACTGGGCAAAGCCAGGA; Reverse: ACGCGGCCGCCTACTTCTTCAGCTTCACGCCCTC).

For CAG promoter-driven inducible expression constructs, eGFP-C-DAAM1 was excised from pCAGGS-GFP-C-DAAM1 and cloned into the EcoRI and NotI sites of pCAGGS-Flex. To make pCAGGS-Flex-GFP, a eGFP fragment was PCR amplified (Forward: TTGACGAATTCATGGTGAGCAAGGGCGAGGAGCTG; Reverse: ATATGCGGCCGCCTACTTGTACAGCTCGTCCATGC) and cloned into the EcoRI and NotI sites of pCAGGS-flex.

For N'-tagged GST-fusion constructs, inserts were PCR amplified from pCAGGS-GFP-MTSS1 with the following primers and inserted into the BamHI and Sall sites of pGEX-4T-3. MTSS1 (Forward: ACACGGATCCATGGAGGCTGTGATCGAGAAGGAAT; Reverse: AGAGTCGACAGAGAAGCGCGGTGCTGAGCGATCGT), I-BAR (Forward: ACACGGATCCATGGAGGCTGTGATCGAGAAGGAAT; Reverse: GTGTGTCGACAGAACCTTTCAAGTCCAAAATCACC), C-MTSS1 (Forward: ACACGGATCCAAGGACTGGGCAAAGCCAGGA; Reverse: AGAGTCGACAGAGAAGCGCGGTGCTGAGCGATCGT), C-MTSS1 Δ WH2 (Forward: ACACGGATCCAAGGACTGGGCAAAGCCAGGA; Reverse: GTGTGTCGACTTCTCTGGGGCTCAGGTCTGCGGGG).

For CMV-promoter driven N' tagged myc-C-DAAM1, C-DAAM1 was PCR amplified from pCAGGS-GFP-C-DAAM1 with the following primers and inserted into the NotI and HindIII sites of pCMV-tag5a. C-DAAM1 (Forward: ACATGCGGCCGCAAGGAAGAAATGATGCAGACCTT; Reverse: CATAAGCTTTTAAAATTAAGTTTTGTGATTGGTC).

For CAG-driven N'tagged mCherry expression constructs, mCherry constructs: MTSS1 (Forward: GACGTCGACATGGAGGCTGTGATCGAGAA; Reverse: TATAAGCTTCTAAGAGAAGCGCGGTGCTGAGCGAT), C-MTSS1 (Forward: GACGTCGACAAGGACTGGGCAAAGCCAGG; Reverse: TATAAGCTTCTAAGAGAAGCGCGGTGCTGAGCGAT), C-MTSS1 Δ WH2 (Forward:

GACGTCGACAAGGACTGGGCAAAGCCAGG;

Reverse:

TATAAGCTTCTATTCTCTGGGGCTCAGGTCTGCGG).

All constructs were sequence verified.

4.5 AAV PRODUCTION

HEK293T cells were transfected using calcium phosphate with the three-plasmid Agilent Helper-Free AAV system, containing a modified expression vector pAAV-CAG::eGFP (Fujishima et al., 2012), pAAV-RC, and pAAV-Helper. After two days of growth, cells were washed in an AAV-wash buffer containing 20 mM Tris HCl (pH 8.0), 250 mM NaCl, and 10 mM MgCl₂, and lysed via three rounds of freeze-thaw cycles. The lysate was centrifuged and filtered through a 0.45 μm filter. Lysates were incubated with AVB Sepharose High Performance (GE Healthcare) for 15 minutes at RT, washed three times with AAV-wash buffer, and eluted using a buffer containing 250 mM NaCl and 10 mM MgCl₂ (pH 3.0), directly into a concentrated Tris pH 8.0 for immediately neutralization. AAV particles were concentrated using an Amicon Ultra Centrifugal filter Ultracel 50K (EMD Millipore).

4.6 AAV INTRACEREBELLAR INJECTION

For intracerebellar injection of AAV-CAG-EGFP into WT and cKO mice, P1 or P2 pups were anesthetized by hypothermia and positioned on a homemade stereotaxic stage made for neonatal mice. After making a small incision through the occipital skin and muscle, a 27-gauge needle (Terumo) was used to create a small hole in the bone over the cerebellar vermis. A 33-gauge needle (Terumo) attached to a microsyringe containing the AAV suspension was inserted 0.5 mm through the incision in the cerebellar vermis. Over 30 sec, 1-2 μL of AAV suspension was slowly injected. The wound was then sutured, and pups were revived at 37°C and returned to the litter after 2 hrs.

4.7 GENOTYPING

Tail clippings were digested in 50 mM NaOH for 10 minutes at 95°C. The *MTSS1^{flox}* allele (LoxP-frt check) was identified by PCR using primers 5'-GGAATGAGATCCGCTTTCCC-3' and 5'-GTTATCTGGGTGCGCCTGTGTAC-3' using KOD FX polymerase kit (Toyobo).

4.8 PURKINJE CELL ELECTROPORATION

Dissociated cerebellar cells were washed three times in Optimem (Gibco) and resuspended in a final volume of 100 μ L Optimem/cuvette (Nepagene) at a concentration of 2-3 cerebella/cuvette, with 10 μ g plasmid DNA. Cells were electroporated using the Nepa21 Electroporator (NepaGene) using the following settings: Poring Pulse: 150 V, 0.8 ms pulse length, 50 ms pulse interval, 2 pulses, 10% decay rate, + polarity; Transfer Pulse: 20 V, 50 ms pulse length, 50 ms pulse interval, 5 pulses, 40% decay rate, +/- polarity. After electroporation, cells were immediately washed with DMEM/F12 supplemented by 10% FBS and plated.

4.9 PHARMACOLOGICAL EXPERIMENTS

For pharmacological experiments, SMI-FH2 (Sigma-Aldrich) was dissolved in DMSO, diluted in media, and added to cultures for 10 minutes at a final concentration of 10 μ M SMI-FH2 and 0.01% DMSO. CK-666 (EMD Millipore) was dissolved in DMSO, diluted in media, and added to cultures for 24 hrs at a final concentration of 20 μ M CK-666 and 0.01% DMSO. Equivalent volumes of media and DMSO were added to control cultures.

4.10 IMMUNOCYTOCHEMISTRY/ IMMUNOHISTOCHEMISTRY

Antibodies were diluted in PBS containing 5% skim milk (w/v) and 0.3% TritonX-100. For immunocytochemistry, cultures were fixed for 5 minutes at RT in freshly prepared paraformaldehyde (4%) in 10 mM MES, 138 mM KCl, 3mM MgCl₂, 2 mM EGTA, and 0.32 M sucrose (pH 6.1) solution. Coverslips were then washed, and cultures were simultaneously permeabilized and blocked with 5% skim milk (w/v) in PBS and 0.3% TritonX-100 for 1 hr at RT. Cells were labelled with primary antibodies as follows: anti-calbindin (mouse, 1:1000, Swant), anti-GFP (chicken, 1:1000, Thermo Fisher Scientific), anti-MTSS1 (rabbit, 1:500, Novus Biologicals), anti-DAAM1 (goat, 1:1000, Santa Cruz), anti-RFP (rabbit, 1:1000, MBL Life Science) in 5% skim milk/PBS-Triton-X100 (0.3%) at 4°C overnight. Cells were washed extensively in PBS-Triton-X100 (0.3%) and stained with Alexa Fluor-conjugated secondary antibodies (1:10000, Molecular Probes) at RT for 1 hr. Coverslips were washed again with PBS-

Triton-X100 (0.3%) and mounted on glass slides using ProLong Gold Antifade (Thermo Fisher Scientific).

For *in vivo* analysis of Purkinje cell morphology and immunohistochemistry, mice were deeply anesthetized by isoflurane, and were transcardially perfused with phosphate buffer (PB) followed by 4% paraformaldehyde (PFA) in PB. Brains were removed, and postfixed overnight in 4% PFA at 4°C. Brains were then washed of PFA with three changes of 1X phosphate buffered saline (PBS), and embedded in 3% low-temperature melting agarose. Sagittal sections were made (100 μ m thick) using a vibratome (DTK-3000, Dosaka EM, Kyoto, Japan). Slices were permeabilized and blocked by incubation with 5% skim milk in PBS-Triton X-100 (0.3% v/v) over night at 4°C. Primary antibody labeling was performed in blocking buffer overnight at 4°C as follows: anti-calbindin (mouse, 1:1000, Swant), anti-GFP (chicken, 1:1000, Thermo Fisher Scientific), anti-MTSS1 (rabbit, 1:500, Novus Biologicals). After thorough washing, slices were incubated with secondary antibodies for 1 h and if needed, followed by 10 μ g/mL DAPI for 10 min at RT. After washing, slices were transferred to SuperFrost Micro slides (Matsunami) and mounted with ProLong Gold Antifade Mountant (Thermo Fisher Scientific).

4.11 INDUCED EXPRESSION OF CONSTITUTIVELY ACTIVE C-DAAM1

Dissociated cerebellar cells were electroporated on 0DIV with a 1:2:3 ratio mix of three plasmids, CAG::TdTomato, pCL20c-L7::ER^{T2}-Cre-ER^{T2}, and CAG::FLEX-eGFP or CAG::FLEX-eGFP-C-DAAM1, and exposed to 500 nM 4-OHT (Sigma Aldrich) either on 11DIV11 or 12DIV for variable induction times.

4.12 IMMUNOPRECIPITATION AND WESTERN BLOT ANALYSIS

For western blotting and immunoprecipitation of endogenous protein, cerebella were dissected and homogenized using a Dounce homogenizer in lysis buffer (PBS plus 0.3% Triton X-100 supplemented with EDTA-free protease inhibitor cocktail (Nacalai Tesque). Lysates were incubated on ice for 30 minutes, cleared by centrifugation (20K x g 15 minutes), and either denatured for 5 min at 95°C in Laemmli buffer or used for immunoprecipitation. For immunoprecipitation, lysates were precleared for 1 hour at 4°C with Protein A/G agarose beads (Santa Cruz Biotechnologies), and then centrifuged for 500 x g for 1 minute. The supernatant was

incubated over night at 4°C with 5 mg of anti-DAAM1 (Novus Biologicals) or control mouse IgG antibody (Jackson ImmunoResearch Labs), followed by incubation with Protein A/G agarose beads (Santa Cruz Biotechnology) for 1 hour at 4°C. Beads were washed four times in lysis buffer and eluted in Laemmli buffer for 5 min at 95°C. Lysates and samples were separated by SDS-PAGE in 10% acrylamide gels and transferred onto PVDF membrane (Millipore). Membranes were blocked for 60 min at room temperature in PBS-Tween with 5% skimmed powdered. Membranes were incubated with primary antibodies in blocking buffer overnight at 4°C at the following concentrations: anti-GFP (mouse, 1: 2000; Sant Cruz Biotechnology), anti-DAAM1 (mouse, 1:1000, Novus Biologicals), anti MTSS1 (mouse, 1:1000, Santa Cruz Biotechnology), anti-mDia1 (mouse, 1:1000, BD Biosciences). Membranes were washed and incubated for 60 min in blocking buffer containing HRP-conjugated anti-goat, rabbit or mouse secondary antibodies (1:10000; EMD Millipore). Signal was detected with ECL Prime (G.E. Healthcare) and imaged on a ChemiDoc XRS+ System (Biorad).

4.13 PROTEIN PURIFICATION

C-DAAM1, MTSS1, and its truncates were expressed as N'tagged GST fusion proteins in BL21-CodonPlus (DE3)-RIPL-competent cells (Agilent). Cells were grown in LB medium to OD₆₀₀ 0.6. Expression was induced by 50 µM IPTG (Nacalai tesque) for GST-MTSS1 and 250 µM IPTG for GST-C-DAAM1, GST-I-BAR, GST-C-MTSS1, and GST-C-MTSS1ΔWH2 constructs. Cells were grown at 18°C overnight for GST-MTSS1 and GST-C-DAAM1, and 37°C for 1-2 h for GST-I-BAR, GST-C-MTSS1, and GST-C-MTSS1ΔWH2 constructs. For MTSS1 and its truncates, cells were harvested and resuspended in lysis buffer (50 mM Tris HCl (pH 8.0), 150 mM NaCl, 1 mM EDTA, 10% glycerol, 1% Triton X-100, 1mM DTT, and 1 mM PMSF), with all subsequent steps performed at 4°C or on ice. Cells were lysed by sonication and centrifuged at 20k x g for 20 min. GST fusion proteins were purified by incubation with Glutathione Sepharose 4B beads (GE Healthcare) for 2 hrs. The beads were then washed four times with wash buffer (50 mM Tris HCl (pH 8.0), 300 mM NaCl, 1 mM EDTA, 10% glycerol, 1% Triton X-100, 1mM DTT, and 1 mM PMSF) and eluted in glutathione buffer (50 mM Tris HCl (pH 8.0), 30 mM reduced glutathione, 150 mM NaCl). The eluted sample was concentrated using Amicon Ultra 4 Centrifugal filter Ultracel 50K

(EMD Millipore) followed by buffer exchange to 50 mM Tris HCl (pH 8.0), 150 mM NaCl, 1 mM EDTA, 10% glycerol, and 1 mM PMSF using a PD-Spin Trap G-25 column (GE Healthcare). For use in TIRFM experiments, the GST tag was cleaved from GST-C-MTSS1 Δ WH2 with thrombin (Nacalai tesque) for 1 hour at RT, and thrombin was removed by incubation with p-aminobenzamidine agarose (Sigma Aldrich). For GST-C-DAAM1, purification was performed as previously described (Vig et al., 2017), stored at 4°C, and used within two weeks.

Rabbit skeletal muscle actin was purified as previously described (Spudich and Watt, 1971), and G-actin was further purified by Superdex 200 pg HiLoad 16/60 gel filtration column (GE Healthcare). Purified G-actin was labeled with DyLight 488 NHS-Ester (Thermo Scientific) as previously described (Mizuno and Watanabe, 2014). Purification of human profilin I was previously described (Higashida et al., 2008).

4.14 GST PULL-DOWN

For pulldown assay, HEK293T cells were transfected with eGFP constructs using Lipofectamine LTX (Thermo Fisher). The following day, cells were washed and lysed in PBS with 0.1% Triton X-100 and EDTA-free protease inhibitor cocktail (Nacalai Tesque), passed through a 27-gauge needle 7 times, incubated on ice for 30 minutes, and centrifuged at 20k x g for 20 minutes. eGFP fluorescence per mg total protein was calculated, and lysate from untransfected cells was used to adjust for equivalent eGFP fluorescence and protein concentration between different eGFP lysates. Pulldown samples were prepared by incubating 1 mg/mL total protein concentration with equivalent eGFP fluorescence and 1 μ M GST protein for 4 hrs at 4°C with end-over-end rotation. Glutathione Sepharose 4B beads (GE Healthcare) were then added and further incubated for 1 hour. Samples were centrifuged at 500x g, and beads were washed four times in PBS supplemented with an additional 150 mM NaCl, 0.1% Triton X-100, and EDTA-free protease inhibitor cocktail (Nacalai Tesque). Beads were eluted in Laemmli buffer for 5 min at 95°C and separated by SDS-PAGE as described above.

4.15 IMAGE ACQUISITION

For fixed samples, multi-channel fluorescent images were acquired on a Fluoview FV1000 (Olympus) laser scanning confocal microscope equipped with

UPLSAPO 40x dry and 100x oil-immersion objectives (NA 0.95 and 1.40, respectively; Olympus). For *ex vivo* dendrite morphology imaging, serial confocal z stack images were acquired from midsagittal Purkinje cells in lobes IV-V with the 40x objective at a z-step of 1 μm . For *in vitro* dendrite morphology, serial confocal z stack images were acquired with the 100x objective at a z-step of 1 μm . For dendritic protrusion imaging, serial confocal z stack images were acquired at distal regions of the dendritic arbor with the 100x objective and 3x digital zoom with a voxel size of 0.04 x 0.04 x 0.39 μm .

For long-term live imaging of developing dendrites, serial confocal z-stacks (4 μm stack, 5 slices x 1 μm z-step) were taken with an incubator microscope (LCV100; Olympus) equipped with a 20x objective (NA 0.7; Olympus) and CO₂ supplementation. Images were taken at 3 h intervals up to 4 days.

For high-resolution live imaging of dendritic protrusions, serial confocal z-stacks were taken with an incubator microscope (IX81; Olympus) equipped with a UPLSAPO 100x objective (NA 1.40, Olympus) and CO₂ supplementation. Images were taken with 3x digital zoom at an interval of 15 sec.

For lower-resolution multi-position live imaging of dendritic protrusions (used for the SMI-FH2 experiments), serial confocal z-stacks were acquired with a spinning disk confocal microscope (CV1000; Yokogawa) using a 100x oil-immersion objective (numerical aperture 1.4; Olympus) and CO₂ supplementation. Images were obtained every 30 sec for 1 hour and stacked to acquire z-max projections.

4.16 XTC CELL ELECTROPORATION AND PREPARATION FOR SIMS IMAGING

Dissociated XTC cells $1.86 \times 10^5/\text{cells}$ were suspended in 10 μL of Buffer R of the Neon® Transfection kit (Invitrogen) with the following amounts of plasmid DNA. For the eGFP-C-DAAM1 control condition, 2.5 ng of plasmid DNA was included per 10 μL of cell suspension. For conditions co-expressing eGFP-C-DAAM1 and mCherry-MTSS1 or its mCherry-conjugated truncates, 2.5-5 ng or eGFP-C-DAAM1 and 2 μg of mCherry construct were included per 10 μL of cell suspension. Cells were electroporated using the 10 μL Neon® pipette tip using the following program: Voltage: 1005V, Width: 35 ms, Pulses: 2. For experiments, cells were trypsinization and resuspended in 70% Leibovitz's L15 medium with no serum or phenol red, and plated on glass coverslips coated with 100 $\mu\text{g}/\text{mL}$ poly-L-lysine. Cells showing similar, low levels of eGFP-C-DAAM1 were selected for imaging 30 minutes post plating.

4.17 TIRF IMAGING OF C-DAAM1-DEPENDENT ELONGATION OF F-ACTIN

Two mg of 0.5 μm carboxylated microspheres (Polysciences Inc.) were functionalized with 100 μg goat anti-GST IgG (GE Healthcare) and 200 μg goat IgG (Jackson ImmunoResearch Labs) in a 3 mg/mL carbodiimide solution (Nacalai tesque) for 2 hours at RT. After quenching the reaction with glycine and extensive washing, anti-GST microspheres were incubated with purified GST-C-DAAM1 for 1 hour at 4°C. GST-C-DAAM1 beads were washed 5 times and resuspended in 50 mM KCl, 10 mM imidazole-HCl, 1 mM MgCl_2 , 1 mM EGTA, 1 mM DTT, pH=7.0).

DyLight 488-labelled actin was diluted with unlabeled actin to achieve 100 μL of 10% labelled actin in G-buffer (2 mM Tris-HCl, 0.2 mM CaCl_2 , 0.2 mM ATP, and 1 mM DTT) and centrifuged at 346K x g, 4°C, for 30 minutes. The upper 50 μL of actin was aspirated for use in assays, within 4 hours of centrifuging.

Homemade glass flow cells were constructed as previously described (Mizuno and Watanabe, 2014), using glass coverslips that had been carbon-coated (VE-2030, Vacuum Device Inc.) and hydrophilized by “Soft” glow-discharge (PIB-10 Vacuum Device, Inc) just prior to flow cell construction. GST-C-DAAM1 beads were incubated in the flow cell for 1 min, followed by two washes of 10% BSA, incubation of 10% BSA for 5 minutes, and six washes of TIRF buffer (50 mM KCl, 10 mM imidazole-HCl, 1 mM MgCl_2 , 1 mM EGTA, 50 μM CaCl_2 , 0.5% methylcellulose, 0.5 mM ATP, 0.5% β -mercaptoethanol, pH=7.0).

To begin nucleation, actin-bound Ca^{2+} to Mg^{2+} exchange was performed by adding 1 mM MgCl_2 and 1 mM EGTA to 10% DyLight488-labelled actin in G-buffer two minutes prior to preparation and perfusion of nucleation buffer (1 μM 10% DyLight488-labelled actin, 50 mM KCl, 10 mM imidazole-HCl, 1 mM MgCl_2 , 50 μM CaCl_2 , 1 mM EGTA, 0.5% methylcellulose, 0.5 mM ATP, 0.5% β -mercaptoethanol, 0.1 mg glucose oxidase, 20 $\mu\text{g}/\text{mL}$ catalase, 4.5 mg/mL glucose) through the flow cell. After 1 min of nucleation, four volumes of elongation buffer (0.5 μM 10% DyLight488-labelled actin, 2 μM profilin I, 50 mM KCl, 10 mM imidazole-HCl, 1 mM MgCl_2 , 50 μM CaCl_2 , 1 mM EGTA, 0.5% methylcellulose, 0.5 mM ATP, 0.5% β -mercaptoethanol, 0.1 mg glucose oxidase, 20 $\mu\text{g}/\text{mL}$ catalase, 4.5 mg/mL glucose) with or without 5 μM C-MTSS1 Δ WH2 was perfused through the flow cell. The total volume of proteins and their storing

buffers were constant among samples and did not exceed 50% of the total sample buffer. All experiments were performed at 20°C.

Fluorescence images of DyLight 488-labelled actin were obtained using an IX81 microscope (Olympus) equipped with Olympus PlanApo Na 1.45100x TIRFM objective lens and BCD1 Blue DDD laser (488 nm, 20 mW, Melles Griot). Images were recorded by a CCD camera (CoolSNAP HQ, Roper Scientific) at 5 s intervals using MetaMorph software (Molecular Devices).

4.18 IMAGE ANALYSIS

For dendrite morphometry, neurons were traced in reconstructed 3-dimensional stacks using Imaris software. Sholl analysis was performed using traced dendrites with Fiji software. To illustrate the cKO phenotype, we defined a primary dendrite as any branch emerging from the soma, terminating in a bifurcation of two equivalent-thickness branches. For protrusion analysis, straight unbranching dendritic segments of 10 µm were selected at least 3 µm away from branch points and tips of dendrites. For time lapse analysis, Z-max projections were made using Metamorph software and dendrites were reconstructed with the same methodology as the fixed samples. Protrusions were manually traced in 3-dimensional stacks using Fiji software. For fluorescent intensity analysis, the maximal intensity projected images were generated, and the mean fluorescent intensity of ROI was measured following the subtraction for off-cell background with ImageJ software (NIH).

For C-DAAM1 speckling analysis, speckles showing processive elongation movement (constant speed, same vector) were tracked using the Speckle Tracker J plugin for Fiji (Smith et al., 2011). Speckles were tracked using the “constant velocity NCC” model, and two-dimensional Gaussian fitting to identify the peak intensity of the speckle was used to improve position to subpixel accuracy. Plots of distance travelled vs time were constructed for each speckle. Due to varying lifetimes of speckles or movement of speckles out of frame, distance travelled was calculated as total distance travelled during observation divided by lifetime of speckle. Speed of speckles were calculated from the slope of the plot at regions where speckles were not obviously paused. We acknowledge that the presence of very small “non-obvious” pauses could also contribute to the reduction of speckle speed. This issue may be addressed with imaging at higher time resolution. Speckles were next classified as “paused” or

“moving” at every timepoint. Speckles were determined to be “paused” at a timepoints when the total distance travelled over the preceding four frames was less than 30% of the expected distance to be travelled according to the speckle speed calculated above.

For TIRF imaging of elongating F-actin, C-DAAM1-dependent elongating F-actin were first identified by finding F-actin with one end immobilized on a bead, showing the relative dark/light regions of the F-actin being pushed away from the bead, indicating the processive incorporation of G-actin by the C-DAAM1-associated barbed end. Filaments were analyzed manually and with the KymoResliceWide plugin of Fiji.

ACKNOWLEDGEMENTS

This doctoral dissertation was completed with the support of several people over the last five and a half years. First and foremost I wish to express my sincere gratitude to my advisor Professor Mineko Kengaku for her continuous support of my Ph.D. study and research. Her patience, motivation, encouragement, and insightful comments helped me grow both academically and personally, and she will continue to be a role model even after I leave this lab. My sincere thanks also goes to Professor Naoki Watanabe for offering his support and providing the opportunity to work in his lab. My work would not have been completed without his extensive knowledge, enthusiasm, encouragement, and feedback. I also owe a great deal of gratitude to Dr. Kazuto Fujishima and Dr. Hiroaki Mizuno for their extensive training, scientific feedback, and mentoring. I sincerely thank my fellow lab mates in the Kengaku Group for always being so friendly, supportive, and making the lab an easy place to work in. I thank Yukari Matsushita for her help and patience when I was struggling to navigate through the Japanese system. I also thank my friends here at Kyoto University who provided a much needed form of escape from my studies and helped me keep things in perspective. Last but not the least, I would like to thank my family: my mother, father, brother, and grandparents for their love and support throughout this journey.

This thesis is based on material contained in the following scholarly paper.

Kawabata Galbraith, K., Fujishima, K., Mizuno, H., Lee, S.-J., Uemura, T., Sakimura, K., Mishina, M., Watanabe, N., and Kengaku, M.
MTSS1 Regulation of Actin-Nucleating Formin DAAM1 in Dendritic Filopodia Determines Final Dendritic Configuration of Purkinje Cells
Cell Reports 24, 95-106, 2018

REFERENCES

- Alvarez, V.A., and Sabatini, B.L. (2007). Anatomical and Physiological Plasticity of Dendritic Spines. *Annu. Rev. Neurosci.* *30*, 79–97.
- Baggett, A.W., Cournia, Z., Han, M.S., Patargias, G., Glass, A.C., Liu, S.-Y., and Nolen, B.J. (2012). Structural characterization and computer-aided optimization of a small-molecule inhibitor of the Arp2/3 complex, a key regulator of the actin cytoskeleton. *ChemMedChem* *7*, 1286–1294.
- Berry, M., and Bradley, P. (1976). The growth of the dendritic trees of Purkinje cells in the cerebellum of the rat. *Brain Res.* *112*, 1–35.
- Bershteyn, M., Atwood, S.X., Woo, W.-M., Li, M., and Oro, A.E. (2010). MIM and Cortactin Antagonism Regulates Ciliogenesis and Hedgehog Signaling. *Dev. Cell* *19*, 270–283.
- Bompard, G. (2005). Involvement of Rac in actin cytoskeleton rearrangements induced by MIM-B. *J. Cell Sci.* *118*, 5393–5403.
- Brette, M., Suchowerska, A.K., Chua, S.W., Ittner, L.M., and Fath, T. (2015). Amyotrophic lateral sclerosis-associated mutant profilin 1 increases dendritic arborisation and spine formation in primary hippocampal neurons. *Neurosci. Lett.* *609*, 223–228.
- Burke, T.A., Christensen, J.R., Barone, E., Suarez, C., Sirotkin, V., and Kovar, D.R. (2014). Homeostatic actin cytoskeleton networks are regulated by assembly factor competition for monomers. *Curr. Biol. CB* *24*, 579–585.
- Callahan, C.A. (2004). MIM/BEG4, a Sonic hedgehog-responsive gene that potentiates Gli-dependent transcription. *Genes Dev.* *18*, 2724–2729.
- Carrier, M.F., Pantaloni, D., and Korn, E.D. (1987). The mechanisms of ATP hydrolysis accompanying the polymerization of Mg-actin and Ca-actin. *J. Biol. Chem.* *262*, 3052–3059.
- Carrier, M.-F., Pernier, J., and Avvaru, B.S. (2013). Control of actin filament dynamics at barbed ends by WH2 domains: From capping to permissive and processive assembly. *Cytoskeleton* *70*, 540–549.
- Cendelin, J. (2014). From mice to men: lessons from mutant ataxic mice. *Cerebellum Ataxias* *1*.
- Chazeau, A., Mehidi, A., Nair, D., Gautier, J.J., Leduc, C., Chamma, I., Kage, F., Kechkar, A., Thoumine, O., Rottner, K., et al. (2014). Nanoscale segregation of actin nucleation and elongation factors determines dendritic spine protrusion. *EMBO J.* *33*, 2745–2764.
- Chen, Q., Nag, S., and Pollard, T.D. (2012). Formins filter modified actin subunits during processive elongation. *J. Struct. Biol.* *177*, 32–39.
- Chereau, D., Kerff, F., Graceffa, P., Grabarek, Z., Langsetmo, K., and Dominguez, R. (2005). Actin-bound structures of Wiskott–Aldrich syndrome protein (WASP)-homology domain 2 and the implications for filament assembly. *Proc. Natl. Acad. Sci. U. S. A.* *102*, 16644–16649.
- Cherniak, C. (1994). Component placement optimization in the brain. *J. Neurosci.* *14*, 2418–2427.
- Chesarone, M.A., and Goode, B.L. (2009). Actin Nucleation and Elongation Factors: Mechanisms and Interplay. *Curr. Opin. Cell Biol.* *21*, 28–37.

- Dailey, M.E., and Smith, S.J. (1996). The dynamics of dendritic structure in developing hippocampal slices. *J. Neurosci. Off. J. Soc. Neurosci.* *16*, 2983–2994.
- Dawson, J.C., Bruche, S., Spence, H.J., Braga, V.M.M., and Machesky, L.M. (2012a). Mtss1 Promotes Cell-Cell Junction Assembly and Stability through the Small GTPase Rac1. *PLoS ONE* *7*, e31141.
- Dawson, J.C., Timpson, P., Kalna, G., and Machesky, L.M. (2012b). Mtss1 regulates epidermal growth factor signaling in head and neck squamous carcinoma cells. *Oncogene* *31*, 1781–1793.
- Dent, E.W., Kwiatkowski, A.V., Mebane, L.M., Philippar, U., Barzik, M., Rubinson, D.A., Gupton, S., Van Veen, J.E., Furman, C., Zhang, J., et al. (2007). Filopodia are required for cortical neurite initiation. *Nat. Cell Biol.* *9*, 1347–1359.
- Didry, D., Cantrelle, F.-X., Husson, C., Roblin, P., Moorthy, A.M.E., Perez, J., Clainche, C.L., Hertzog, M., Guittet, E., Carlier, M.-F., et al. (2012). How a single residue in individual β -thymosin/WH2 domains controls their functions in actin assembly. *EMBO J.* *31*, 1000–1013.
- Du, P., Ye, L., Li, H., Yang, Y., and Jiang, W.G. (2012). The tumour suppressive role of metastasis suppressor-1, MTSS1, in human kidney cancer, a possible connection with the SHH pathway. *J. Exp. Ther. Oncol.* *10*, 91–99.
- Dutta, P., and Maiti, S. (2015). Expression of multiple formins in adult tissues and during developmental stages of mouse brain. *Gene Expr. Patterns GEP* *19*, 52–59.
- Emoto, K., Parrish, J.Z., Jan, L.Y., and Jan, Y.-N. (2006). The tumour suppressor Hippo acts with the NDR kinases in dendritic tiling and maintenance. *Nature* *443*, 210–213.
- Fahrenkamp, D., Herrmann, O., Koschmieder, S., Brümmendorf, T.H., and Schemionek, M. (2017). Mtss1(CSC156) mutant mice fail to display efficient Mtss1 protein depletion. *Leukemia* *31*, 1017–1019.
- Fiala, J.C., and Harris, K.M. (2007). *Dendrites* (Oxford University Press).
- Fuerst, P.G., Bruce, F., Tian, M., Wei, W., Elstrott, J., Feller, M.B., Erskine, L., Singer, J.H., and Burgess, R.W. (2009). DSCAM and DSCAML1 function in self-avoidance in multiple cell types in the developing mouse retina. *Neuron* *64*, 484–497.
- Fujishima, K., Horie, R., Mochizuki, A., and Kengaku, M. (2012). Principles of branch dynamics governing shape characteristics of cerebellar Purkinje cell dendrites. *Development* *139*, 3442–3455.
- Fujiwara, I., Vavylonis, D., and Pollard, T.D. (2007). Polymerization kinetics of ADP- and ADP-Pi-actin determined by fluorescence microscopy. *Proc. Natl. Acad. Sci. U. S. A.* *104*, 8827–8832.
- Fukumitsu, K., Fujishima, K., Yoshimura, A., Wu, Y.K., Heuser, J., and Kengaku, M. (2015). Synergistic Action of Dendritic Mitochondria and Creatine Kinase Maintains ATP Homeostasis and Actin Dynamics in Growing Neuronal Dendrites. *J. Neurosci.* *35*, 5707–5723.
- Gao, L., and Bretscher, A. (2008). Analysis of Unregulated Formin Activity Reveals How Yeast Can Balance F-Actin Assembly between Different Microfilament-based Organizations. *Mol. Biol. Cell* *19*, 1474–1484.

- Gibson, D.A., Tymanskyj, S., Yuan, R.C., Leung, H.C., Lefebvre, J.L., Sanes, J.R., Chédotal, A., and Ma, L. (2014). Dendrite Self-Avoidance Requires Cell-Autonomous Slit/Robo Signaling in Cerebellar Purkinje Cells. *Neuron* *81*, 1040–1056.
- Glassmann, A., Molly, S., Surchev, L., Nazwar, T.A., Holst, M., Hartmann, W., Baader, S.L., Oberdick, J., Pietsch, T., and Schilling, K. (2007). Developmental expression and differentiation-related neuron-specific splicing of metastasis suppressor 1 (Mtss1) in normal and transformed cerebellar cells. *BMC Dev. Biol.* *7*, 111.
- Glebov, O.O., and Burrone, J. (2016). Interaction between distinct pools controls activity-dependent actin dynamics in the dendritic spine. *BioRxiv* 077933.
- González-Burgos, I., González-Tapia, D., Zamora, D.A.V., Feria-Velasco, A., and Beas-Zárate, C. (2011). Guided motor training induces dendritic spine plastic changes in adult rat cerebellar purkinje cells. *Neurosci. Lett.* *491*, 216–220.
- Gonzalez-Quevedo, R. (2005). Receptor tyrosine phosphatase-dependent cytoskeletal remodeling by the hedgehog-responsive gene MIM/BEG4. *J. Cell Biol.* *168*, 453–463.
- Gordon, D.J., Boyer, J.L., and Korn, E.D. (1977). Comparative biochemistry of non-muscle actins. *J. Biol. Chem.* *252*, 8300–8309.
- Gould, C.J., Maiti, S., Michelot, A., Graziano, B.R., Blanchoin, L., and Goode, B.L. (2011). The formin DAD domain plays dual roles in autoinhibition and actin nucleation. *Curr. Biol. CB* *21*, 384–390.
- Grueber, W.B., Ye, B., Moore, A.W., Jan, L.Y., and Jan, Y.N. (2003). Dendrites of Distinct Classes of Drosophila Sensory Neurons Show Different Capacities for Homotypic Repulsion. *Curr. Biol.* *13*, 618–626.
- Habas, R., Kato, Y., and He, X. (2001). Wnt/Frizzled Activation of Rho Regulates Vertebrate Gastrulation and Requires a Novel Formin Homology Protein Daam1. *Cell* *107*, 843–854.
- Halpain, S., Hipolito, A., and Saffer, L. (1998). Regulation of F-Actin Stability in Dendritic Spines by Glutamate Receptors and Calcineurin. *J. Neurosci.* *18*, 9835–9844.
- Han, C., Wang, D., Soba, P., Zhu, S., Lin, X., Jan, L.Y., and Jan, Y.-N. (2012). Integrins regulate repulsion-mediated dendritic patterning of drosophila sensory neurons by restricting dendrites in a 2D space. *Neuron* *73*, 64–78.
- Hashimoto, K., Tsujita, M., Miyazaki, T., Kitamura, K., Yamazaki, M., Shin, H.-S., Watanabe, M., Sakimura, K., and Kano, M. (2011). Postsynaptic P/Q-type Ca²⁺ channel in Purkinje cell mediates synaptic competition and elimination in developing cerebellum. *Proc. Natl. Acad. Sci.* *108*, 9987–9992.
- Häusser, M., Spruston, N., and Stuart, G.J. (2000). Diversity and Dynamics of Dendritic Signaling. *Science* *290*, 739–744.
- Hayn-Leichsenring, G., Liebig, C., Miething, A., Schulz, A., Kumar, S., Schwalbe, M., Eiberger, B., and Baader, S.L. (2011). Cellular distribution of metastasis suppressor 1 and the shape of cell bodies are temporarily altered in Engrailed-2 overexpressing cerebellar Purkinje cells. *Neuroscience* *189*, 68–78.
- Heiman, M.G., and Shaham, S. (2010). Twigs into branches: How a filopodium becomes a dendrite. *Curr. Opin. Neurobiol.* *20*, 86–91.

Higashi, T., Ikeda, T., Shirakawa, R., Kondo, H., Kawato, M., Horiguchi, M., Okuda, T., Okawa, K., Fukai, S., Nureki, O., et al. (2008). Biochemical Characterization of the Rho GTPase-regulated Actin Assembly by Diaphanous-related Formins, mDia1 and Daam1, in Platelets. *J. Biol. Chem.* *283*, 8746–8755.

Higashida, C., Miyoshi, T., Fujita, A., Ocegüera-Yanez, F., Monypenny, J., Andou, Y., Narumiya, S., and Watanabe, N. (2004). Actin polymerization-driven molecular movement of mDia1 in living cells. *Science* *303*, 2007–2010.

Higashida, C., Suetsugu, S., Tsuji, T., Monypenny, J., Narumiya, S., and Watanabe, N. (2008). G-actin regulates rapid induction of actin nucleation by mDia1 to restore cellular actin polymers. *J. Cell Sci.* *121*, 3403–3412.

Hirano, A., Dembitzer, H.M., and Yoon, C.H. (1977). Development of Purkinje cell somatic spines in the weaver mouse. *Acta Neuropathol. (Berl.)* *40*, 85–90.

Hoffmann, A.-K., Naj, X., and Linder, S. (2014). Daam1 is a regulator of filopodia formation and phagocytic uptake of *Borrelia burgdorferi* by primary human macrophages. *FASEB J.* *28*, 3075–3089.

Holst, M.I., Maercker, C., Pintea, B., Masseroli, M., Liebig, C., Jankowski, J., Miething, A., Martini, J., Schwaller, B., Oberdick, J., et al. (2008). Engrailed-2 regulates genes related to vesicle formation and transport in cerebellar Purkinje cells. *Mol. Cell. Neurosci.* *38*, 495–504.

Hotulainen, P., and Hoogenraad, C.C. (2010). Actin in dendritic spines: connecting dynamics to function. *J. Cell Biol.* *189*, 619–629.

Hotulainen, P., Llano, O., Smirnov, S., Tanhuanpää, K., Faix, J., Rivera, C., and Lappalainen, P. (2009). Defining mechanisms of actin polymerization and depolymerization during dendritic spine morphogenesis. *J. Cell Biol.* *185*, 323–339.

Ing-Esteves, S., Kostadinov, D., Marocha, J., Sing, A.D., Joseph, K.S., Laboulaye, M., Sanes, J.R., and Lefebvre, J.L. (2018). Combinatorial effects of Alpha- and Gamma-Protocadherins on neuronal survival and dendritic self-avoidance. *J. Neurosci. Off. J. Soc. Neurosci.*

Isaksson, H.S., Sorbe, B., and Nilsson, T.K. (2014). Whole genome expression profiling of blood cells in ovarian cancer patients –Prognostic impact of the CYP1B1, MTSS1, NCALD, and NOP14 genes. *Oncotarget* *5*, 4040–4049.

Ito, M. (1989). Long-Term Depression. *Annu. Rev. Neurosci.* *12*, 85–102.

Jaiswal, R., Breitsprecher, D., Collins, A., Corrêa Jr., I.R., Xu, M.-Q., and Goode, B.L. (2013). The Formin Daam1 and Fascin Directly Collaborate to Promote Filopodia Formation. *Curr. Biol.* *23*, 1373–1379.

Kaufmann, W.E., and Moser, H.W. (2000). Dendritic Anomalies in Disorders Associated with Mental Retardation. *Cereb. Cortex* *10*, 981–991.

Kayser, G., Csanadi, A., Kakanou, S., Prasse, A., Kassem, A., Stickeler, E., Passlick, B., and Hausen, A. zur (2015). Downregulation of MTSS1 expression is an independent prognosticator in squamous cell carcinoma of the lung. *Br. J. Cancer* *112*, 866–873.

Kida, Y., Shiraishi, T., and Ogura, T. (2004). Identification of chick and mouse Daam1 and Daam2 genes and their expression patterns in the central nervous system. *Dev. Brain Res.* *153*, 143–150.

Kim, I.H., Racz, B., Wang, H., Burianek, L., Weinberg, R., Yasuda, R., Wetsel, W.C., and Soderling, S.H. (2013). Disruption of Arp2/3 Results in Asymmetric Structural Plasticity of Dendritic Spines and Progressive Synaptic and Behavioral Abnormalities. *J. Neurosci.* *33*, 6081–6092.

Korobova, F., and Svitkina, T. (2010). Molecular Architecture of Synaptic Actin Cytoskeleton in Hippocampal Neurons Reveals a Mechanism of Dendritic Spine Morphogenesis. *Mol. Biol. Cell* *21*, 165–176.

Lee, K.J., Kim, H., Kim, T.S., Park, S.-H., and Rhyu, I.J. (2004). Morphological analysis of spine shapes of Purkinje cell dendrites in the rat cerebellum using high-voltage electron microscopy. *Neurosci. Lett.* *359*, 21–24.

Lee, Y.-G., Macoska, J.A., Korenchuk, S., and Pienta, K.J. (2002). MIM, a Potential Metastasis Suppressor Gene in Bladder Cancer. *Neoplasia* *4*, 291–294.

Lefebvre, J.L., Kostadinov, D., Chen, W.V., Maniatis, T., and Sanes, J.R. (2012). Protocadherins mediate dendritic self-avoidance in the mammalian nervous system. *Nature* *488*, 517–521.

Lefebvre, J.L., Sanes, J.R., and Kay, J.N. (2015). Development of Dendritic Form and Function. *Annu. Rev. Cell Dev. Biol.* *31*, 741–777.

Li, L., Baxter, S.S., Gu, N., Ji, M., and Zhan, X. (2017). Missing-in-metastasis protein downregulates CXCR4 by promoting ubiquitination and interaction with small Rab GTPases. *J Cell Sci* jcs.198937.

Lin, J., Liu, J., Wang, Y., Zhu, J., Zhou, K., Smith, N., and Zhan, X. (2005). Differential regulation of cortactin and N-WASP-mediated actin polymerization by missing in metastasis (MIM) protein. *Oncogene* *24*, 2059–2066.

Ling, D.-J., Chen, Z.-S., Liao, Q.-D., Feng, J.-X., Zhang, X.-Y., and Yin, T.-Y. (2016). Differential effects of MTSS1 on invasion and proliferation in subtypes of non-small cell lung cancer cells. *Exp. Ther. Med.* *12*, 1225–1231.

Liu, W., Sato, A., Khadka, D., Bharti, R., Diaz, H., Runnels, L.W., and Habas, R. (2008). Mechanism of activation of the Formin protein Daam1. *Proc. Natl. Acad. Sci.* *105*, 210–215.

Liu, W., Komiya, Y., Mezzacappa, C., Khadka, D.K., Runnels, L., and Habas, R. (2011). MIM regulates vertebrate neural tube closure. *Development* *138*, 2035–2047.

Lohmann, C., and Bonhoeffer, T. (2008). A Role for Local Calcium Signaling in Rapid Synaptic Partner Selection by Dendritic Filopodia. *Neuron* *59*, 253–260.

London, M., and Häusser, M. (2005). Dendritic Computation. *Annu. Rev. Neurosci.* *28*, 503–532.

Lu, J., Meng, W., Poy, F., Maiti, S., Goode, B.L., and Eck, M.J. (2007). Structure of the FH2 Domain of Daam1: Implications for Formin Regulation of Actin Assembly. *J. Mol. Biol.* *369*, 1258–1269.

Luo, L. (2002). Actin Cytoskeleton Regulation in Neuronal Morphogenesis and Structural Plasticity. *Annu. Rev. Cell Dev. Biol.* *18*, 601–635.

Ma, S., Guan, X.-Y., Lee, T.K., and Chan, K.W. (2007). Clinicopathological significance of missing in metastasis B expression in hepatocellular carcinoma. *Hum. Pathol.* *38*, 1201–1206.

- Maddugoda, M.P., Stefani, C., Gonzalez-Rodriguez, D., Saarikangas, J., Torrino, S., Janel, S., Munro, P., Doye, A., Prodon, F., Aurrand-Lions, M., et al. (2011). cAMP Signaling by Anthrax Edema Toxin Induces Transendothelial Cell Tunnels, which Are Resealed by MIM via Arp2/3-Driven Actin Polymerization. *Cell Host Microbe* *10*, 464–474.
- Marchenko, O.O., Das, S., Yu, J., Novak, I.L., Rodionov, V.I., Efimova, N., Svitkina, T., Wolgemuth, C.W., and Loew, L.M. (2017). A minimal actomyosin-based model predicts the dynamics of filopodia on neuronal dendrites. *Mol. Biol. Cell* *28*, 1021–1033.
- Matsuoka, R.L., Jiang, Z., Samuels, I.S., Nguyen-Ba-Charvet, K.T., Sun, L.O., Peachey, N.S., Chédotal, A., Yau, K.-W., and Kolodkin, A.L. (2012). Guidance-cue control of horizontal cell morphology, lamination, and synapse formation in the mammalian outer retina. *J. Neurosci. Off. J. Soc. Neurosci.* *32*, 6859–6868.
- Mattila, P.K. (2003). Mouse MIM, a Tissue-specific Regulator of Cytoskeletal Dynamics, Interacts with ATP-Actin Monomers through Its C-terminal WH2 Domain. *J. Biol. Chem.* *278*, 8452–8459.
- Mattila, P.K., Pykäläinen, A., Saarikangas, J., Paavilainen, V.O., Vihinen, H., Jokitalo, E., and Lappalainen, P. (2007). Missing-in-metastasis and IRSp53 deform PI(4,5)P₂-rich membranes by an inverse BAR domain-like mechanism. *J. Cell Biol.* *176*, 953–964.
- McAllister, A.K., Katz, L.C., and Lo, D.C. (1997). Opposing roles for endogenous BDNF and NT-3 in regulating cortical dendritic growth. *Neuron* *18*, 767–778.
- Mel, B.W., Schiller, J., and Poirazi, P. (2017). Synaptic plasticity in dendrites: complications and coping strategies. *Curr. Opin. Neurobiol.* *43*, 177–186.
- Mertz, K.D., Pathria, G., Wagner, C., Saarikangas, J., Sboner, A., Romanov, J., Gschaider, M., Lenz, F., Neumann, F., Schreiner, W., et al. (2014). MTSS1 is a metastasis driver in a subset of human melanomas. *Nat. Commun.* *5*.
- Miermans, C.A., Kusters, R.P.T., Hoogenraad, C.C., and Storm, C. (2017). Biophysical model of the role of actin remodeling on dendritic spine morphology. *PLOS ONE* *12*, e0170113.
- Miller, F.D., and Kaplan, D.R. (2003). Signaling mechanisms underlying dendrite formation. *Curr. Opin. Neurobiol.* *13*, 391–398.
- Miyagi, Y., Yamashita, T., Fukaya, M., Sonoda, T., Okuno, T., Yamada, K., Watanabe, M., Nagashima, Y., Aoki, I., Okuda, K., et al. (2002). Delphilin: a Novel PDZ and Formin Homology Domain-Containing Protein that Synaptically Colocalizes and Interacts with Glutamate Receptor δ 2 Subunit. *J. Neurosci.* *22*, 803–814.
- Mizuno, H., and Watanabe, N. (2014). Chapter Five - Rotational Movement of Formins Evaluated by Using Single-Molecule Fluorescence Polarization. In *Methods in Enzymology*, R.D. Vale, ed. (Academic Press), pp. 73–94.
- Montaville, P., Jégou, A., Pernier, J., Compper, C., Guichard, B., Mogessie, B., Schuh, M., Romet-Lemonne, G., and Carlier, M.-F. (2014). Spire and Formin 2 Synergize and Antagonize in Regulating Actin Assembly in Meiosis by a Ping-Pong Mechanism. *PLOS Biol.* *12*, e1001795.
- Nägerl, U.V., Eberhorn, N., Cambridge, S.B., and Bonhoeffer, T. (2004). Bidirectional Activity-Dependent Morphological Plasticity in Hippocampal Neurons. *Neuron* *44*, 759–767.

- Napper, R.M.A., and Harvey, R.J. (1988). Number of parallel fiber synapses on an individual Purkinje cell in the cerebellum of the rat. *J. Comp. Neurol.* *274*, 168–177.
- Niell, C.M., Meyer, M.P., and Smith, S.J. (2004). In vivo imaging of synapse formation on a growing dendritic arbor. *Nat. Neurosci.* *7*, 254–260.
- Parnass, Z., Tashiro, A., and Yuste, R. (2000). Analysis of spine morphological plasticity in developing hippocampal pyramidal neurons. *Hippocampus* *10*, 561–568.
- Parr, C., and Jiang, W.G. (2009). Metastasis suppressor 1 (MTSS1) demonstrates prognostic value and anti-metastatic properties in breast cancer. *Eur. J. Cancer* *45*, 1673–1683.
- Pollard, T.D. (1986). Rate constants for the reactions of ATP- and ADP-actin with the ends of actin filaments. *J. Cell Biol.* *103*, 2747–2754.
- Pollard, T.D. (2007). Regulation of actin filament assembly by Arp2/3 complex and formins. *Annu. Rev. Biophys. Biomol. Struct.* *36*, 451–477.
- Quinones, G. (2010). Missing in Metastasis mediates directional sensing during guided cell migration.
- Ramon y Cajal, S. (1911). *Histology of the Nervous System of Man and Vertebrates* (Translated from the French). (Oxford, UK: Oxford University Press).
- Raymond, J.L., Lisberger, S.G., and Mauk, M.D. (1996). The cerebellum: A neuronal learning machine? *Sci. Wash.* *272*, 1126.
- Rimkus, T.K., Carpenter, R.L., Qasem, S., Chan, M., and Lo, H.-W. (2016). Targeting the Sonic Hedgehog Signaling Pathway: Review of Smoothed and GLI Inhibitors. *Cancers* *8*.
- Rotty, J.D., Wu, C., Haynes, E.M., Suarez, C., Winkelman, J.D., Johnson, H.E., Haugh, J.M., Kovar, D.R., and Bear, J.E. (2015). Profilin-1 Serves as a Gatekeeper for Actin Assembly by Arp2/3-Dependent and -Independent Pathways. *Dev. Cell* *32*, 54–67.
- Saarikangas, J., Zhao, H., Pykäläinen, A., Laurinmäki, P., Mattila, P.K., Kinnunen, P.K.J., Butcher, S.J., and Lappalainen, P. (2009). Molecular Mechanisms of Membrane Deformation by I-BAR Domain Proteins. *Curr. Biol.* *19*, 95–107.
- Saarikangas, J., Mattila, P.K., Varjosalo, M., Bovellan, M., Hakanen, J., Calzada-Wack, J., Tost, M., Jennen, L., Rathkolb, B., Hans, W., et al. (2011). Missing-in-metastasis MIM/MTSS1 promotes actin assembly at intercellular junctions and is required for integrity of kidney epithelia. *J. Cell Sci.* *124*, 1245–1255.
- Saarikangas, J., Kourdougli, N., Senju, Y., Chazal, G., Segerstråle, M., Minkeviciene, R., Kuurne, J., Mattila, P.K., Garrett, L., Hölter, S.M., et al. (2015). MIM-Induced Membrane Bending Promotes Dendritic Spine Initiation. *Dev. Cell* *33*, 644–659.
- Saengsawang, W., Taylor, K.L., Lumbard, D.C., Mitok, K., Price, A., Pietila, L., Gomez, T.M., and Dent, E.W. (2013). CIP4 coordinates with phospholipids and actin-associated proteins to localize to the protruding edge and produce actin ribs and veils. *J Cell Sci* *126*, 2411–2423.
- Salomon, S.N., Haber, M., Murai, K.K., and Dunn, R.J. (2008). Localization of the Diaphanous-related formin Daam1 to neuronal dendrites. *Neurosci. Lett.* *447*, 62–67.

- Schätzle, P., Ster, J., Verbich, D., McKinney, R.A., Gerber, U., Sonderegger, P., and María Mateos, J. (2011). Rapid and reversible formation of spine head filopodia in response to muscarinic receptor activation in CA1 pyramidal cells. *J. Physiol.* *589*, 4353–4364.
- Sept, D., and McCammon, J.A. (2001). Thermodynamics and Kinetics of Actin Filament Nucleation. *Biophys. J.* *81*, 667–674.
- Sistig, T., Lang, F., Wrobel, S., Baader, S.L., Schilling, K., and Eiberger, B. (2017). Mtss1 promotes maturation and maintenance of cerebellar neurons via splice variant-specific effects. *Brain Struct. Funct.* 1–19.
- Smith, C.J., Watson, J.D., VanHoven, M.K., Colón-Ramos, D.A., and Miller, D.M. (2012). Netrin (UNC-6) mediates dendritic self-avoidance. *Nat. Neurosci.* *15*, 731–737.
- Smith, M.B., Karatekin, E., Gohlke, A., Mizuno, H., Watanabe, N., and Vavylonis, D. (2011). Interactive, Computer-Assisted Tracking of Speckle Trajectories in Fluorescence Microscopy: Application to Actin Polymerization and Membrane Fusion. *Biophys. J.* *101*, 1794–1804.
- Snider, J., Pillai, A., and Stevens, C.F. (2010). A universal property of axonal and dendritic arbors. *Neuron* *66*, 45–56.
- Spence, E.F., Kanak, D.J., Carlson, B.R., and Soderling, S.H. (2016). The Arp2/3 Complex Is Essential for Distinct Stages of Spine Synapse Maturation, Including Synapse Unsilencing. *J. Neurosci.* *36*, 9696–9709.
- Spudich, J.A., and Watt, S. (1971). The regulation of rabbit skeletal muscle contraction. I. Biochemical studies of the interaction of the tropomyosin-troponin complex with actin and the proteolytic fragments of myosin. *J. Biol. Chem.* *246*, 4866–4871.
- Suarez, C., Carroll, R.T., Burke, T.A., Christensen, J.R., Bestul, A.J., Sees, J.A., James, M.L., Sirotkin, V., and Kovar, D.R. (2015). Profilin Regulates F-Actin Network Homeostasis by Favoring Formin over Arp2/3 Complex. *Dev. Cell* *32*, 43–53.
- Takayama, C., Nakagawa, S., Watanabe, M., Mishina, M., and Inoue, Y. (1996). Developmental changes in expression and distribution of the glutamate receptor channel $\delta 2$ subunit according to the Purkinje cell maturation. *Dev. Brain Res.* *92*, 147–155.
- Takeuchi, T., Ohtsuki, G., Yoshida, T., Fukaya, M., Wainai, T., Yamashita, M., Yamazaki, Y., Mori, H., Sakimura, K., Kawamoto, S., et al. (2008). Enhancement of Both Long-Term Depression Induction and Optokinetic Response Adaptation in Mice Lacking Delphilin. *PLOS ONE* *3*, e2297.
- Tsuji, T., Ohta, Y., Kanno, Y., Hirose, K., Ohashi, K., and Mizuno, K. (2010). Involvement of p114-RhoGEF and Lfc in Wnt-3a- and Dishevelled-Induced RhoA Activation and Neurite Retraction in N1E-115 Mouse Neuroblastoma Cells. *Mol. Biol. Cell* *21*, 3590–3600.
- Ueyama, T., Ninoyu, Y., Nishio, S.-Y., Miyoshi, T., Torii, H., Nishimura, K., Sugahara, K., Sakata, H., Thumkeo, D., Sakaguchi, H., et al. (2016). Constitutive activation of DIA1 (DIAPH1) via C-terminal truncation causes human sensorineural hearing loss. *EMBO Mol. Med.* *8*, 1310–1324.
- Vig, A.T., Földi, I., Szikora, S., Migh, E., Gombos, R., Tóth, M.Á., Huber, T., Pintér, R., Talián, G.C., Mihály, J., et al. (2017). The activities of the c-terminal regions of the formin protein dishevelled-associated activator of morphogenesis (daam) in actin dynamics. *J. Biol. Chem.* *292*, 13566–13583.

- Wang, D., Xu, M., Wang, T., Li, T., and Zhu, J. wei (2011). MTSS1 overexpression correlates with poor prognosis in colorectal cancer. *J. Gastrointest. Surg. Off. J. Soc. Surg. Aliment. Tract* *15*, 1205–1212.
- Wang, Y., Zhou, K., Zeng, X., Lin, J., and Zhan, X. (2007). Tyrosine Phosphorylation of Missing in Metastasis Protein Is Implicated in Platelet-derived Growth Factor-mediated Cell Shape Changes. *J. Biol. Chem.* *282*, 7624–7631.
- Wegner, A.M., Nebhan, C.A., Hu, L., Majumdar, D., Meier, K.M., Weaver, A.M., and Webb, D.J. (2008). N-WASP and the Arp2/3 Complex Are Critical Regulators of Actin in the Development of Dendritic Spines and Synapses. *J. Biol. Chem.* *283*, 15912–15920.
- Woodings, J.A., Sharp, S.J., and Machesky, L.M. (2003). MIM-B, a putative metastasis suppressor protein, binds to actin and to protein tyrosine phosphatase delta. *Biochem. J.* *371*, 463.
- Wu, J.-Q., and Pollard, T.D. (2005). Counting Cytokinesis Proteins Globally and Locally in Fission Yeast. *Science* *310*, 310–314.
- Xia, S., Li, X., Johnson, T., Seidel, C., Wallace, D.P., and Li, R. (2010). Polycystin-dependent fluid flow sensing targets histone deacetylase 5 to prevent the development of renal cysts. *Development* *137*, 1075–1084.
- Xie, F., Ye, L., Chen, J., Wu, N., Zhang, Z., Yang, Y., Zhang, L., and Jiang, W.G. (2011). The impact of Metastasis Suppressor-1, MTSS1, on oesophageal squamous cell carcinoma and its clinical significance. *J. Transl. Med.* *9*, 95.
- Yamagishi, A., Masuda, M., Ohki, T., Onishi, H., and Mochizuki, N. (2004). A Novel Actin Bundling/Filopodium-forming Domain Conserved in Insulin Receptor Tyrosine Kinase Substrate p53 and Missing in Metastasis Protein. *J. Biol. Chem.* *279*, 14929–14936.
- Yamasaki, M., Miyazaki, T., Azechi, H., Abe, M., Natsume, R., Hagiwara, T., Aiba, A., Mishina, M., Sakimura, K., and Watanabe, M. (2011). Glutamate receptor $\delta 2$ is essential for input pathway-dependent regulation of synaptic AMPAR contents in cerebellar Purkinje cells. *J. Neurosci. Off. J. Soc. Neurosci.* *31*, 3362–3374.
- Yu, D., Zhan, X.H., Niu, S., Mikhailenko, I., Strickland, D.K., Zhu, J., Cao, M., and Zhan, X. (2011). Murine Missing in Metastasis (MIM) Mediates Cell Polarity and Regulates the Motility Response to Growth Factors. *PLoS ONE* *6*, e20845.
- Yu, D., Zhan, X.H., Zhao, X.F., Williams, M.S., Carey, G.B., Smith, E., Scott, D., Zhu, J., Guo, Y., Cherukuri, S., et al. (2012). Mice deficient in MIM expression are predisposed to lymphomagenesis. *Oncogene* *31*, 3561–3568.
- Yu, J., Lin, S., Wang, M., Liang, L., Zou, Z., Zhou, X., Wang, M., Chen, P., and Wang, Y. (2016). Metastasis suppressor 1 regulates neurite outgrowth in primary neuron cultures. *Neuroscience* *333*, 123–131.
- Yuste, R., and Bonhoeffer, T. (2004). Genesis of dendritic spines: insights from ultrastructural and imaging studies. *Nat. Rev. Neurosci.* *5*, 24–34.
- Zeleniak, A.E., Huang, W., Fishel, M.L., and Hill, R. (2018). PTEN-Dependent Stabilization of MTSS1 Inhibits Metastatic Phenotype in Pancreatic Ductal Adenocarcinoma. *Neoplasia* *20*, 12–24.

Zhan, T., Cao, C., Li, L., Gu, N., Civin, C.I., and Zhan, X. (2016). MIM regulates the trafficking of bone marrow cells via modulating surface expression of CXCR4. *Leukemia* 30, 1327–1334.

Zhao, H., Pykäläinen, A., and Lappalainen, P. (2011). I-BAR domain proteins: linking actin and plasma membrane dynamics. *Curr. Opin. Cell Biol.* 23, 14–21.

Zhou, L., Li, J., Shao, Q.-Q., Guo, J.-C., Liang, Z.-Y., Zhou, W.-X., Zhang, T.-P., You, L., and Zhao, Y.-P. (2016). Expression and Significances of MTSS1 in Pancreatic Cancer. *Pathol. Oncol. Res.* 22, 7–14.

Ziv, N.E., and Smith, S.J. (1996). Evidence for a Role of Dendritic Filopodia in Synaptogenesis and Spine Formation. *Neuron* 17, 91–102.

IMAGE LICENSING INFORMATION

Figure 1B: Reprinted from *Neuron*, 77:6, 1017–1038. Parekh, R., and Ascoli, G.A. Neuronal Morphology Goes Digital: A Research Hub for Cellular and System Neuroscience. Copyright 2013, with permission from Elsevier, license # 4367011146555.

Figures 2A-C: Santiago Cajal y Ramon (1852-1934). Public domain – Creative Commons.

Figures 3A-B: Henry Gray (1918) *Anatomy of the Human Body*. Public domain – Creative Commons.

Figure 3C: Daniel John Cunningham (1913) *Cunningham's Textbook of anatomy*. Public domain – Creative Commons.

Figure 4A and B: Reprinted from *Cellular and Molecular Life Sciences*, 74, 4511–4537. Ledda, F., and Paratcha, G. Mechanisms regulating dendritic arbor patterning. Copyright 2017, with permission from Springer Nature, license # 4385801071728.

Figure 5A: Modified from *Frontiers in Cellular Neurosciences*. Ramaswamy, S., and Markram, H. Anatomy and physiology of the thick-tufted layer 5 pyramidal neuron. Copyright 2015 Creative Commons Attribution 4.0 International Public License.

Figure 5B: Reprinted from *Journal of Physiology*, 567, 829–850. McKay, B.E., and Turner, R.W. Physiological and morphological development of the rat cerebellar Purkinje cell. Copyright 2005) with permission from Wiley and Sons, license # 4385791371487.

Figure 8A-C. Reprinted from *Nature Reviews Cancer*, 11, 177–187. Nürnberg, A., Kitzing, T., and Grosse, R. (2011). Nucleating actin for invasion. Copyright 2011 with permission from Springer Nature, license # 4385950966271.

Figures 9A-B. Reprinted from *Open Biology*, 3, 130079. Ireton, K. Molecular mechanisms of cell–cell spread of intracellular bacterial pathogens. Copyright 2013, Creative Commons Attribution 4.0 International Public License.

Figure 10A. Reprinted from *Journal of Cell Biology*, 189, 619–629. Hotulainen, P., and Hoogenraad, C.C. Actin in dendritic spines: connecting dynamics to function. Copyright 2010, with permission from Rockefeller Press, license # 4386180227060.

Figure 10B. Reprinted from *Current Opinion in Neurobiology* 39, 86–92. Lei, W., Omotade, O.F., Myers, K.R., and Zheng, J.Q. (2016). Actin cytoskeleton in dendritic spine development and plasticity. Copyright 2016, with permission from Elsevier, license # 4386931038378.